國 立 交 通 大 學

應用化學系博士班

博 士 論 文

新穎含鉿之金屬間化合物的合成與分析

Synthesis and Characterization of New Hafnium-containing Intermetallics

研 究 生：黃文亨

指導教授：李積琛 博士

中 華 民 國 一 百 年 九 月

#

新穎含鉿之金屬間化合物的合成與分析

Synthesis and Characterization of New Hafnium-containing Intermetallics

研 究 生：黃文亨　　Student：Wen-Heng Huang

指導教授：李積琛　　Advisor：Chi-Shen Lee

國 立 交 通 大 學

應 用 化 學 系 博 士 班

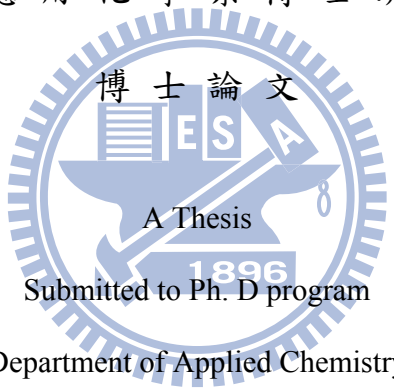

博 士 論 文

A Thesis

Submitted to Ph. D program

Department of Applied Chemistry

College of Science

National Chiao Tung University

in partial Fulfillment of the Requirements

for the Degree of

Doctor of Philosophy

in

Applied Chemistry

September 2011

Hsinchu, Taiwan, Republic of China

中華民國一百年九月

#

Contents

#

新穎含鉿之金屬間化合物的合成與分析

學生: 黃文亨　　指導教授: 李積琛　博士

國立交通大學應用化學系博士班

摘要

在本論文中，我們利用電弧反應合成含鉿之金屬間化合物，藉由單晶繞射解析其結構，並透過理論計算研究這些化合物的電子結構。首先，在 Hf–Cu–Al 的三元系統中，我們得到三個 Laves phase 結構化合物 $HfAl_{2-x}Cu_x$ (x = 0.49, 0.88, 1.04)。實驗顯示，隨著鋁逐漸被銅取代，化合物的結構會依序呈現 $MgCu_2$，$MgNi_2$，$MgZn_2$ 三種不同類型的變化。電性測量顯示在室溫下，其電阻率分別為 4.35 (x = 0.5)、5.85 (x = 0.7)，6.50 (x = 0.9)。透過理論計算，我們可以得到化合物在穩定態時，銅原子與鋁原子在結構中的分布傾向，同時此結果亦可印證我們在實驗中實際觀察到的現象。接著，同樣是在 Hf–Cu–Al 的三元系統中，我們得到一化合物 $Hf_6Cu_{16}Al_{7.58}$。此化合物的結構可視為一組成單體以立方最密推積的方式所構成，而此組成單體則是由四個多面體層所組合。儘管由結構上來看，Al2 原子處於一個在鍵結環境上較不適宜的位置，但是電子結構的計算顯示 Al2 與鄰近的 Hf 原子仍有很強烈的鍵結。然後，在 Hf–Al–Sb 的三元系統中，我們得到三個化合物 $Hf_5Al_{3-x}Sb_x$ (x = 0.70, 1.44, 2.14)。此系統在 $0 \le x \le 1.0$ 以及 $2.0 \le x \le 2.5$ 的範圍內，分別呈現 Mn_5Si_3 與 W_5Si_3 兩種結構類型的相寬。這兩種結構各為兩種不同的多面體沿著 c 軸所構成。理論計算的結果說明該化合物的電子結構主要是來自於 Hf–Sb 鍵結的貢獻，而系統的穩定度則同時受到異鍵結 Hf–Al 與 Hf–Sb 的影響。最後，在 Hf–Ni–Ga 的三元系統中，我們得到兩個金屬間化合物 $Hf_{13.0}Ni_{40.8}Ga_{30.9}$ 與 $Zr_{13.0}Ni_{40.6}Ga_{31.0}$，其結構是由鍵結數不等的多面體所組成(鉿：12–15，鎳與鎵：6–12)。進一步的結構分析顯示，此化合物可視為 $CaCu_5$ 的結構延伸，即透過取代與移除原子位置所得的層狀架構。

#

Synthesis and Characterization of New Hafnium-containing Intermetallics

Student: Wen-Heng Huang Advisor: Dr. Chi-Shen Lee

Department of Applied Chemistry
National Chiao Tung University

Abstract

The main topic for this dissertation focuses on the synthesis, structures, and physical properties of ternary hafnium aluminides that contains four parts as listed below: 1) A series of new ternary intermetallic phases $HfAl_{2-x}Cu_x$ (x = 0.49, 0.88, 1.04) and characterized them as Laves phase structures. X-ray diffraction revealed homogeneity within the ranges $0.2 \leq x \leq 0.5$ and $0.7 \leq x \leq 0.9$ for the $MgCu_2$ and $MgNi_2$ structure types, respectively. When Cu atoms gradually replaced the Al atoms, the structure type altered in the sequence $MgCu_2$ → $MgNi_2$ → $MgZn_2$, and distortion of Kagomé nets occurred with varying bond lengths. Measurements of physical properties revealed these phases were metallic, with resistances of 4.35(x = 0.5), 5.85 (x = 0.7), and 6.50 (x = 0.9) mΩ·cm, respectively, at temperatures 300 K. The coloring schemes revealed that, upon increasing the Cu atom content, the stability of these phases correlated with the arrangements of the Al and Cu atoms. Calculated electronic structures indicated that the bonding character was consistent with experimentally observed phase width. 2) Hafnium copper aluminide $Hf_6Cu_{16}Al_{7.58}$ was synthesized from the pure elements in an arc- melting reaction; its structure was solved from X-ray diffraction data of a single crystal. The structure contains building unit as four successive polyhedral shells adopting cubic close packing. Calculations of the band structure indicate an intense interaction in Hf-Al contacts despite the unfavorable coordination environment, and a strong contribution from Cu–Al interactions. 3) Three new hafnium aluminium antimonides $Hf_5Al_{3-x}Sb_x$ (x = 0.70, 1.44, 2.14)

#

were synthesized from the pure elements in an arc-melting reaction; their structures were solved from X-ray diffraction data of single crystals. Two ranges of homogeneity were observed through Al/Sb mixing, which appeared within ranges $0 \leq x \leq 1.0$ for Mn_5Si_3 structure type and $2.0 \leq x \leq 2.5$ for W_5Si_3 type. Both structures are regarded as condensations of two polyhedra stacking along the *c* axis. Calculations of their electronic structures revealed substantial contributions from Hf-Sb interactions; the heteroatomic bonding (Hf-Al and Hf-Sb contacts) affected the stability of these two phases. Measurements of resistivity on polycrystalline samples showed dependence on temperature, indicating a metallic behavior consistent with the results from calculations. 4) Ternary compounds $Hf_{13.0}Ni_{40.8}Ga_{30.9}$ and $Zr_{13.0}Ni_{40.6}Ga_{31.0}$ that were synthesized from the pure elements in an arc-melting reaction, and characterized their structures through X-ray diffraction of single crystals. Each compound adopted a hexagonal structure of $Y_{13}Pd_{40}Sn_{31}$ type and crystallized in the space group *P6/mmm* (no. 191). The cell parameters of $Hf_{13.0}Ni_{40.8}Ga_{30.9}$ were a = 17.895(3) Å; c = 8.2434(16) Å; V = 2286.0(6) Å^3; and R_1/wR_2 = 0.0299/0.0598. The cell parameters of $Zr_{13.0}Ni_{40.6}Ga_{31.0}$ were a = 17.964(3) Å; c = 8.2757(17) Å; V = 2312.7(7) Å^3; and R_1/wR_2 = 0.0348/0.0686. These structures comprise polyhedra with diverse coordination numbers (Hf 12–15, Ni and Ga 6–12) and the analysis of structures revealed the layer frameworks based on the $CaCu_5$-type structures. Calculated electronic structures revealed a strong contribution from Ni-Ga interaction and the characteristics of a polar intermetallics phase.

#

Acknowledgments

記得不久前，總是覺得時間過得相當緩慢，一直在期待口試完畢的這一天到來。口試當天，在與口試委員別過的那一刻，內心卻意外平靜，彷彿就只是結束了一次實驗室的 meeting。到今天，要重新回憶過去日子，竟又覺得過去近十年的日子彷彿瞬間就過去了。這真的是一種很矛盾的情緒。

我還記得，第一次見到李積琛老師的時候。那時候實驗室還只有一間小休息室，我忐忑地走進去問坐在椅子上的老師，是否可以收我進實驗室。感謝老師，感謝您為我開啟一扇學術的小窗戶。感謝您培養我做科學的態度，感謝您接受我在實驗上的顛簸，感謝您在我迷惘困惑時給予我許多的指導與鼓勵。

感謝所有曾經在實驗室中相處過的夥伴。我會永遠珍惜這一份回憶與成長，不論是好是壞，都會成為我今後人生重要的一部分。感謝明芳、奎伯，感謝這份曾經的革命情感與兄弟情誼。感謝明誠，感謝你對我在做人處事上的啟發。感謝明諺、聖豐、家侃，感謝你們支持實驗室的運作。感謝學弟妹們，感謝所有與你們在實驗室內發生過的事。

感謝我的父親母親，感謝您們雖然不懂我的課業，卻還是默默地關心與支持我。感謝您們從小就給我最好的環境，感謝您們給我第一個家，更感謝您們給我第二個家。希望這一次課業的成就能讓您們不用再擔心我，更希望您們能為我感到驕傲。

感謝我的小天使們，感謝你們的出生與成長。感謝您們那天真無邪的臉龐，能讓我得到最舒緩的喘息。感謝您們加上我身上的擔子，爸爸會永遠將你們捧在懷裡。

最後要感謝我摯愛的欣芳。感謝妳在這幾年的付出，感謝妳為我帶來這麼美好的家庭成員。感謝妳接納我這一個不常說感謝的人。感謝我們已經完成，以及未來要完成的人生旅程。

#

List of Tables

#

Chapter 3

Chapter 4

Chapter 5

#

List of Figures

Chapter 6

#

Chapter 1

Introduction

1.1 Background

Intermetallic refers to solid-state phases composed of two or more metals. For metallurgy, this area is about the alloying behavior of the elements, i.e. metal phases that are capable of incorporating different amount of elements into its lattice without structural change [1], which may form several homogeneous compounds in a certain range of composition. In the early centuries, metallurgists performed works with hundreds of different proportions of metal elements in order to obtain optimized metallic properties for daily applications (Fig. 1.1), as exemplifies in Table 1.1 [2]. It is believed that the Chinese ancient book "Rites of Zhou" recorded the first example of metallurgy. It says that the alloy combined with cooper and tin in ratio 1:6 can be used for food utensil, and its hardness will increases with the tin composition, making the alloy capable to be cast as ax or sword. Some researchers suspected that structural transformation might occur between metals due to the observations of varying densities [3], however, crystallographic studies were impeded at that time by the restrictions of crystal separating technique and structure resolving tool.

#

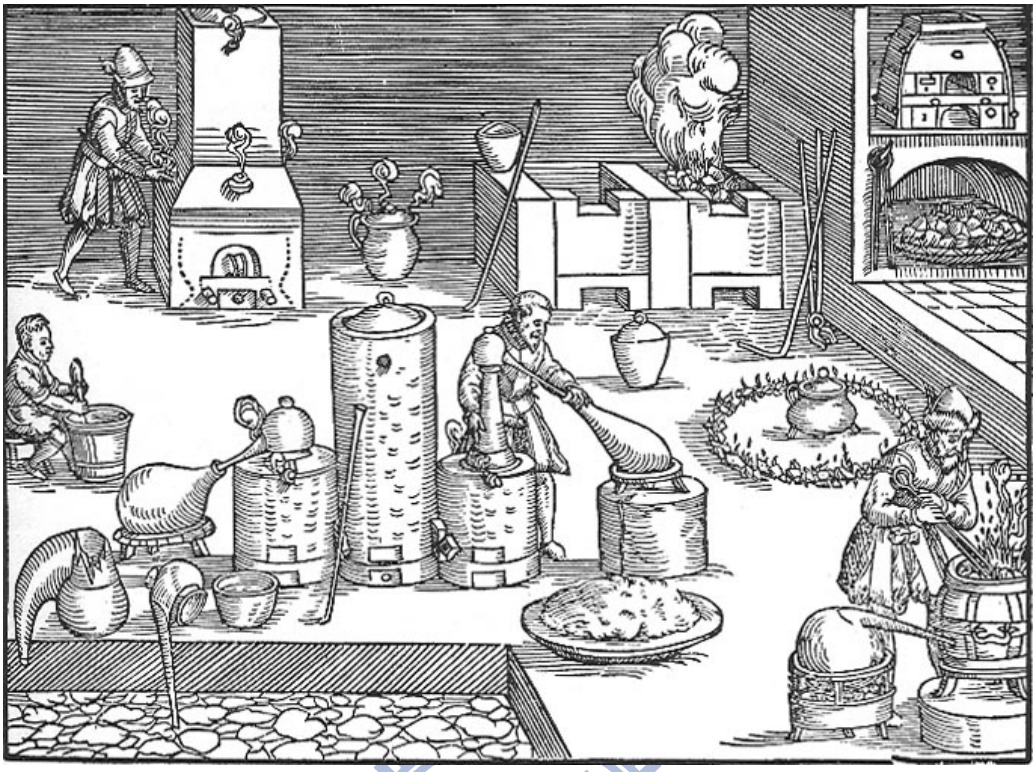

Fig 1.1 Illustration of a metallurgy process drawn by Lazarus Ericker in 1574.

Table 1.1 Past applications of intermetallics [4]

Since approx.	Material or process	Phase	Application
2500 B.C.	cementation	Cu_3Al	coating of bronze tools, etc.
100 B.C.	yellow brass	CuZn	coins, ornamental parts
0	high tin bronze	$Cu_{31}Sn_8$	mirror
600	amalgam	$Ag_2Hg_3 + Sn_6Hg$	dental restorative
1500		Cu_4Hg_3	
1505	amalgam	Sn_8Hg	mirror
1540	type metal	SbSn	printing
1910	acutal	SbSn	fruit knife
1926	Permendur	FeCo	soft magnetic alloy
1931	Alnico	NiAl-Fe-Co	Mermanent magnet material

1.2 Literature Review

The behavior of metallurgy gradually became a subject of scientific research at the beginning of last century with breakthrough works in many territories. German metallurgist Tammann contributed the technique of thermal analysis by introducing the method of quantitative measurement of the times of thermal arrest for alloy samples, that helped to determine the composition of any intermediate phase [5]. Laue *et al*. found that X-rays should be diffracted by crystal [6], which provided fundamental theory of crystallography. Andrews published the first X-ray studies of the Fe-Ni and Fe-Co systems [7], that the crystal structure change from that of one component to that of the other as the composition was varied across the system. With more structural variations proved via powder methods [8], the term "intermetallics" has been referred as compounds of metals whose crystal structures are different from those of the constituent metals [9]. Pauling performed first crystal-structure determination on an complex intermetallic Mg_2Sn, which was essentially indecipherable by powder pattern techniques [10]. Shull reported the first neutron diffraction pattern for intermetallic phases [11], extending researches to those compounds with lack of sufficient difference in the scattering powers of the component elements. Until this day, the developed X-ray diffracting method still leads crystallographic studies to explore new phase, new structure and new type of atomic bonding in the field of intermetallic.

The works implemented by X-ray diffracting technique are tremendous, and the enormous data are collected and classified by Goldschmidt on metallic radii [12], Okamoto on phase diagrams [13]

#

and Pearson on crystal structure and lattice parameters [14] as significant references in crystallographic study. For a long time, chemists have attempted to establish a general principle to interpret those variations of structures listed in the literatures, such as Wade's rules for deltahedral cluster entities [15] and the (8-N) rule of valence compounds [16] which link electron counts to particular geometrical arrangements. Hume-Rothery also made contributions, that he pointed out a great number of compounds, also called Hume-Rothery phases, are alloys with the structures of different types of brass (Cu-Zn alloys) which are effected by valence electron concentration (VEC, number of valence electrons per atom). A survey is given in Table 1.2 [17] and structures are illustrated in Fig 1.2. With increasing composition of metal zinc, structure type of phase varies with the sequence fcc → bcc → γ-brass → hcp [18]. Recently, examples of similar structures that exhibit structural stability is solely determined by the electron count or VEC are the system T_mE_n with T = transition metal and E = heavier p-block element [19], and the quasi-binary transition metal distannide systems $T_xT'_{1-x}Sn_2$ (T and T' from the first transition series) with structural sequence $CuMg_2$ → $NiMg_2$ → $CuAl_2$ → $CoGe_2$ which was supported with computational calculations [20].

Table 1.2 Brass phases [17]

	composition	VEC	Structure type	examples
α	$Cu_{1-x}Zn_x$, x = 0 to 0.38	1 to 1.38	Cu	
β	CuZn	1.50 = 3/2	W	AgZn, Cu_3Al, Cu_5Sn
γ	Cu_5Zn_8	1.62 = 21/13	Cu_5Sn_8	Ag_5Sn_8, Cu_9Al_4, $Na_{31}Pb_9$
ε	$CuZn_3$	1.75 = 7/4	Mg	$AgZn_3$, Cu_3Sn, Ag_5Al_3
η	$Cu_{1-x}Zn_x$, x = 0.98 to 1	1.98 to 2	Mg	

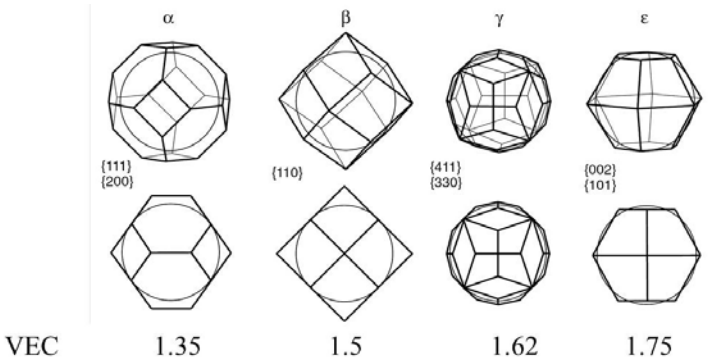

Fig 1.2 Structures of Hume-Rothery phases

With increasing value of VEC, there are some aluminide substructures with varying VEC between two and four electrons per atom. This so-called R-phase belongs to a collection of crystalline approximants whose structures and compositions are presumed to be close to those of corresponding quasicrystals. Recently, it has been well studied in the Mg–Zn–Al system about the site occupancy and VEC-controlled bonding states via theoretical calculation [21].

The relation between structure and VEC still maintains as the number is larger than four, and compounds meet this value mostly are Zintl phases. This is class of compounds consisting of an cationic component (alkali metal, alkaline earth metal, lanthanoid) and an anionic component of p-element (post-transition) metal and metalloid constructing polyatomic clusters or network anions of these elements [22]. The excitement in exploratory synthesis of Zintl phase is that a remarkable variety of homoatomic and other bonding types is found in anionic states of the post-transition metals[23], and that a great number of these diverse species can be understood in terms of stoichiometry, geometry, and electron count by Zintl-Klemm concepts [24, 25].

#

Besides valence electron concentration, atomic size is another effective factor affecting the structure of intermetallic compounds. Laves is the first one proposed the principle of compound formation that based on the relative sizes of the component atoms. For general compound AB_2 of the larger Laves phase family, the closest packing of hard spheres is obtained for an ideal radius ratio r_A / r_B is ca. 1.225 [26]. However, just like other intermetallic compounds, the structure of Laves compound is not only determined by the size ratio, but also controlled by electronegativities and valence electron numbers of the A and B atoms, as shown in Fig 1.3 [27].

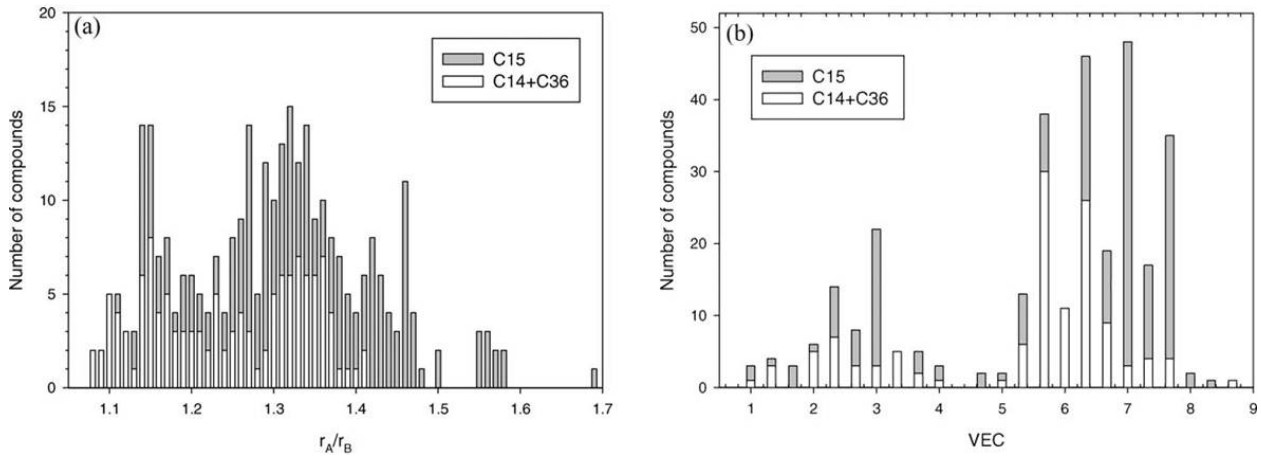

Fig 1.3 Frequency of Laves phase structure type vs. (a) atomic radius ratio r_A / r_B and (b) valence electron concentration [28].

1.3 Recent Researches

In the last decade, many intermetallics have been reported and classified as anionic DFSO-stabilized compounds (DFSO = differential fractional site occupancies) [29]. In this category, there are three criteria: (i) the metal atom sites are occupied by mixtures of two different metal

#

atoms; (ii) these occupancies vary from site to site; and (iii) the crystal structure does not occur in any of the two corresponding binary systems. In the last decade, many have been reported in this category; furthermore, these researches are studied with theoretical calculation to understand the site preference [30] or electronic structure [31] of the compound. Tkachuk *et al*. reported system $ZrSn_{2-x}Sb_x$ whose structure type varied in the sequence $TiSi_2$ → $CrSi_2$ → $PbCl_2$ as Sb atoms gradually replaced the Sn atoms (Fig 1.4). The calculation revealed that the $TiSi_2$-type and $CrSi_2$-type are more stable in energy, but interlayer Sb–Sb bonding is important in stabilizing the structure of $PbCl_2$-type [32]. The system $KBi_{2-x}Pb_x$ investigated by Ponou indicated a structural distortion with space group degradation from $Fd\bar{3}m$ to $F\bar{4}3m$, and theoretically proved that the behavior corresponded to a proper charge-balanced Zintl phase [33] (Fig 1.5). In system $Gd_5Si_{4-x}Bi_x$, the interslab dimers were disconnected which resulted new slabs and stacking sequence and may therefore change the structure-depending physical property [34] (Fig 1.6).

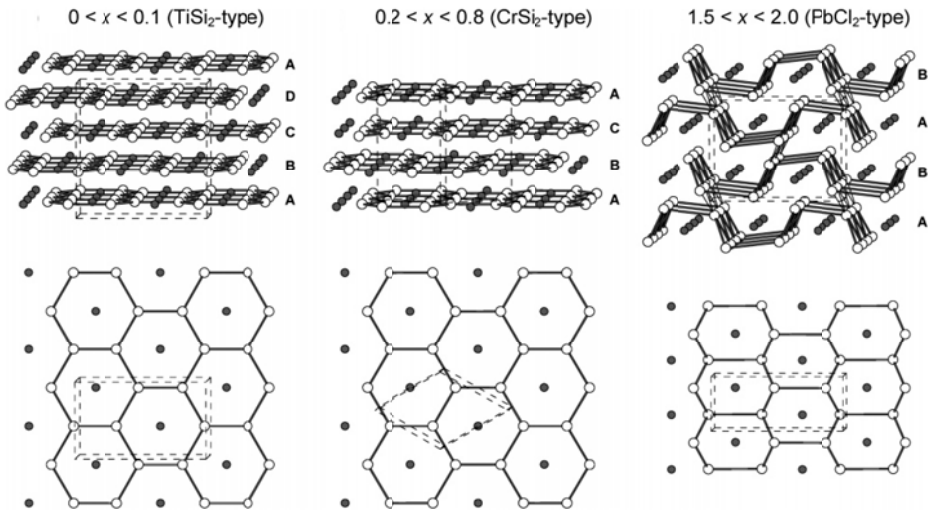

Fig. 1.4 Structures of $ZrSn_{2-x}Sb_x$ in terms of different stacking sequences [32].

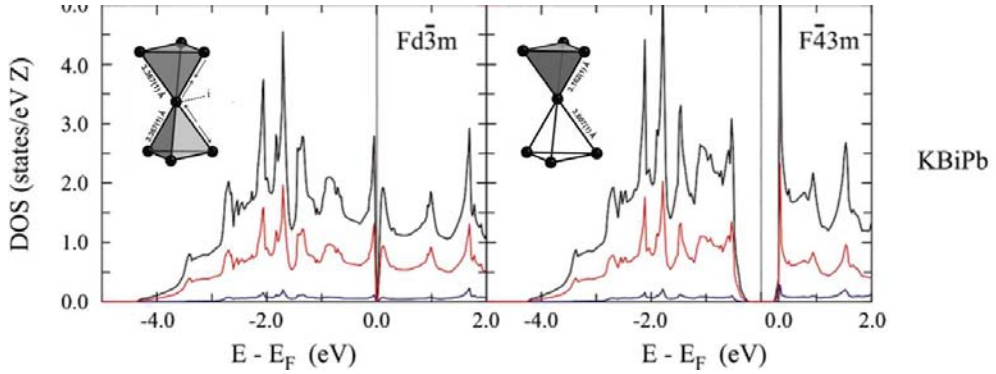

Fig. 1.5 The variation of structures and electronic structures of system $KBi_{2-x}Pb_x$ [33].

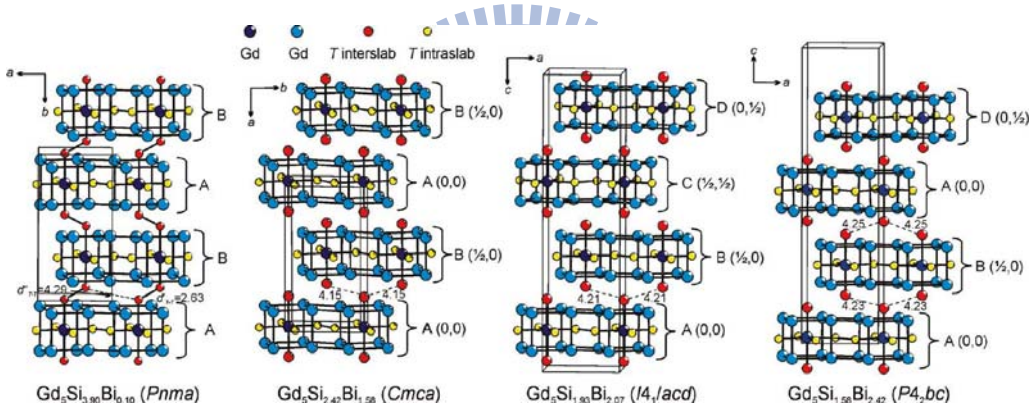

Fig. 1.6 Structures of slab stacking in the $Gd_5Si_{4-x}Bi_x$ phases [34].

Besides the DFSO materials, lots efforts to explore phases comprising cationic elements (alkali metal, alkaline earth metal, lanthanoid and early-transition metal), late-transition metal, and main group elements (groups 13 to 15) have been dedicated by many assiduous scientists. The most prolific chemist is John D. Corbett. He and his group published dozens of literatures in the last decade providing significant insight of solid state phases, especially polar intermetallics [35, 36]. In

theory practice, he demonstrated that, in AB_4 phase, the atomic size governed the formation of structure, from the ordered anionic network to distorted structures, as shown in Fig. 1.7 owing to the varying spaces via replacement of cationic element ($SrIn_4$, [37]) or anionic element ($BaHg_2Tl_2$, [38]; Ba_2AuTl_7, [39]). In crystal synthesis, they reported several crystalline approximants such as $Sc_3Cu_yZn_{18-y}$ ($0 \leqq y \leqq \sim 2.2$) [40], $CaAu_3Ga$ [41]; furthermore, in the case of $Mg_2Cu_6Ga_5$ [42, 43] and $Na_2Au_6In_5$ [44], they predicted existences of bcc approximant and quasicrystal phases from the corresponding pseudogap in LMTO calculations (Fig. 1.8) rather than theoretical guess with Hume–Rothery concepts, and experimentally obtained crystalline approximants in Sc–Mg–Zn [45] and Ca–Au–In systems [46].

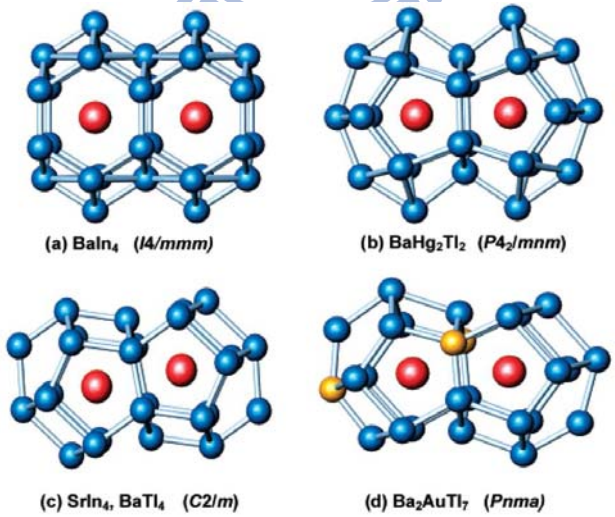

Fig. 1.7 The variations of $BaIn_4$ structures, that are induced by element replacements [47].

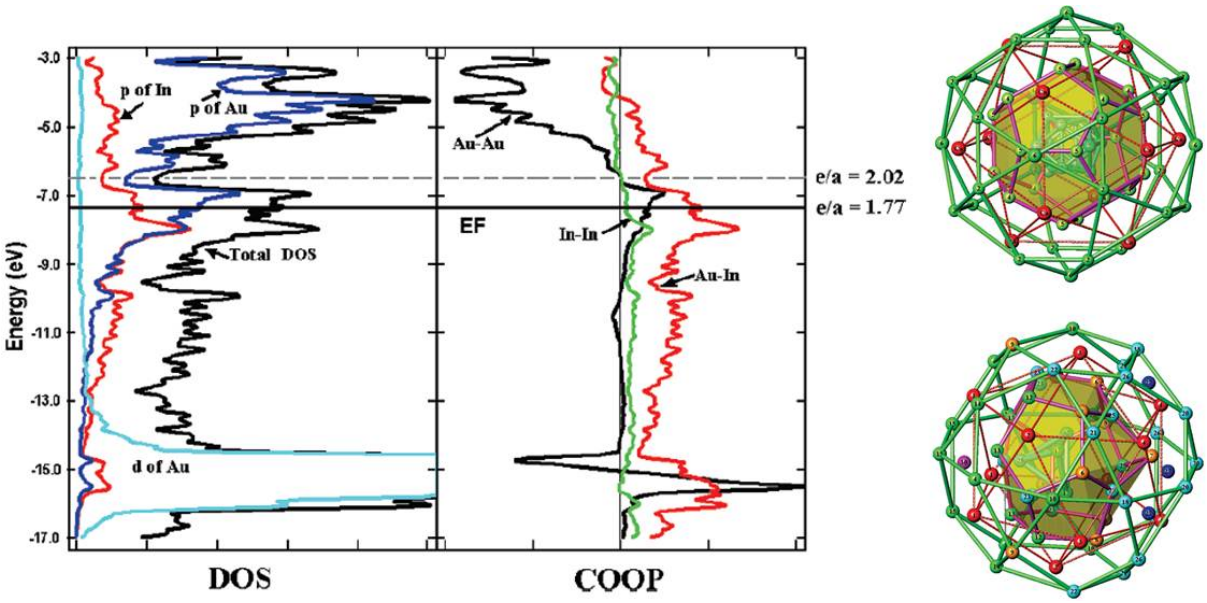

Fig. 1.8 Densities-of-states and crystal orbital overlap population data for $Na_2Au_6In_5$, and poly-clusters of 1/1 and 2/1 approximants [46].

Mercouri G. Kanatzidis is another diligent chemist with major contributions in thermoelectric material. Examples like $AgPb_mSbTe_{2+m}$, $AgPb_mSn_nSbTe_{2+m+n}$, $NaPb_mSbTe_{2+m}$, all provides self-formed inhomogeneities on the nanostructures to conduct low lattice thermal conductivity (Fig. 1.9)[48]. Recently, Kanatzidis reported compounds with regulable physical properties controlled by site vacancy, component element and phase composition. For $Y_4Mn_{1-x}Ga_{12-y}Ge_y$, its ferromagnetism develops as Ge concentration gradually decreases as well as Mn vacancies, creating ordered Mn atoms and vacancies in slabs of octahedral (Fig. 1.10) and 6-fold supercell, that makes this system the first example where ferromagnetism can be tunable by the magnetic species [49]. For NaFeAs, its superconductivity occurs when the material is Na deficient, and the T_c is controlled by the composition ratio of NaFeAs and its oxidized phase $NaFe_2As_2$ [50].

#

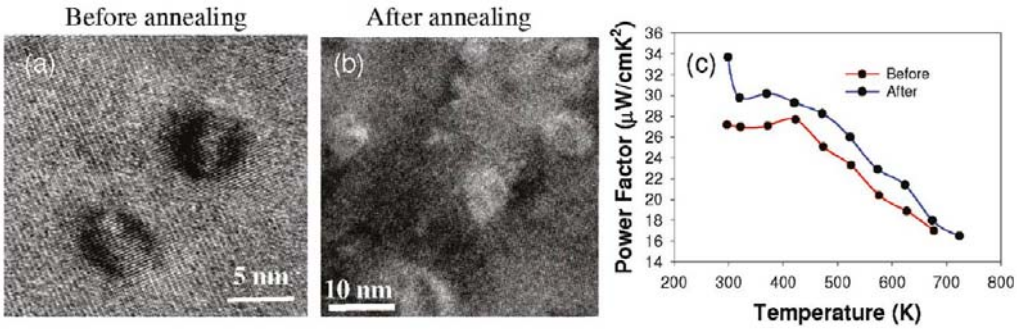

Fig. 1.9 High resolution transmission electron microscopy of a $AgPb_mSbTe_{2+m}$ sample and power factor of the sample [48].

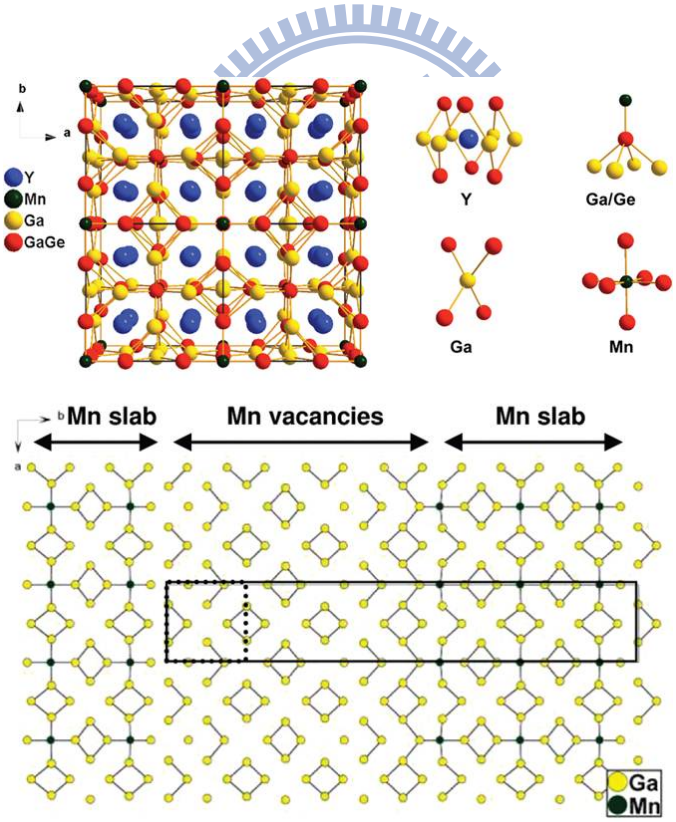

Fig. 1.10 Crystal structure of $Y_4Mn_{0.95}Ga_{11.0}Ge_{1.0}$ (top) and the 6-fold supercell viewing along the *c*-axis [49].

Gordon J. Miller established a delicate theory, the “coloring problem”, addresses the issues of structural preference of different elements within a given structure [30]. Example revealed in the intermetallics ZrMoP and ZrNbP with three possible structure types: Co_2Si, Fe_2P, and Cu_2Sb. The calculation results, as shown in Fig. 1.11, indicated that the most stable phase shall be the one with the lowest total energy. Another example exhibited in γ-brass structure of the Cu–Zn system [51]. The distribution of two adjacent elements used to be resolved by neutron diffraction method; on the other hand, the authors performed theoretical study to obtain information the about atomic arrangement. Table 1.3. lists the energies of different models. The lowest energy arrangement is in agreement with crystallography result, and consistent with the plot of relative Mulliken populations (Fig, 1.12), that the positive values indicate sites for more electropositive elements. Similar concepts were applied in Zn–Pd system [52], R_5Pn_3-type phases (Pn = Sb, Bi) [53], and AeE_2 (Ae = Ca, Sr, Ba; E = Al, Ga, In) [54].

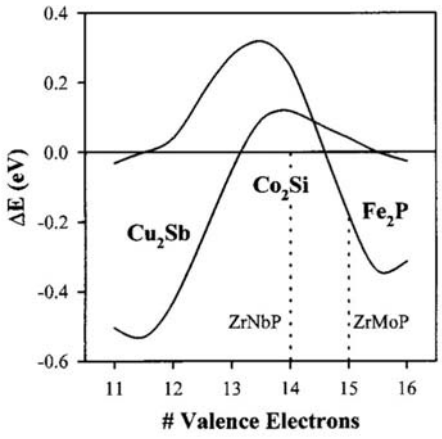

Fig. 1.11 Energy difference curves vs. valence electron count for the Co_2Si-, Fe_2P-, and Cu_2Sb-structure types as possible models [30].

Table 1.3. various atomic arrangements for Cu_5Zn_8 and their relative total energies per atoms [51]

	space group	M1 (M1′)	M2 (M2′)	M3 (M3′)	M4 (M4′)	formula	energy/atom (eV)
A	$I\bar{4}3m$	Cu	Zn	Cu	Zn	$(Cu_{10}Zn_{16})_2$	0
B	$I\bar{4}3m$	Zn	Cu	Cu	Zn	$(Cu_{10}Zn_{16})_2$	0.028
C	$P\bar{4}3m$	Cu	Zn	Cu	Zn	$(Cu_{10}Zn_{16})$	0.010
		Zn	Cu	Cu	Zn	$(Cu_{10}Zn_{16})$	
D	$P\bar{4}3m$	Cu	Cu	Zn	Zn	(Cu_8Zn_{18})	0.025
		Zn	Zn	Zn	Cu	$(Cu_{12}Zn_{14})$	
E	$P\bar{4}3m$	Cu	Cu	Cu	Zn	(Cu_6Zn_{20})	0.025
		Zn	Zn	Cu	Zn	$(Cu_{14}Zn_{12})$	
F	$P\bar{4}3m$	Cu	Zn	Zn	Zn	(Cu_4Zn_{22})	0.001
		Cu	Zn	Zn	Cu	$(Cu_{16}Zn_{10})$	
G	$P\bar{4}3m$	Zn	Cu	Zn	Zn	(Cu_4Zn_{22})	0.012
		Zn	Cu	Zn	Cu	$(Cu_{16}Zn_{10})$	
H	$P\bar{4}3m$	Zn	Zn	Zn	Zn	(Cu_0Zn_{26})	0.022
		Cu	Cu	Zn	Cu	$(Cu_{20}Zn_6)$	

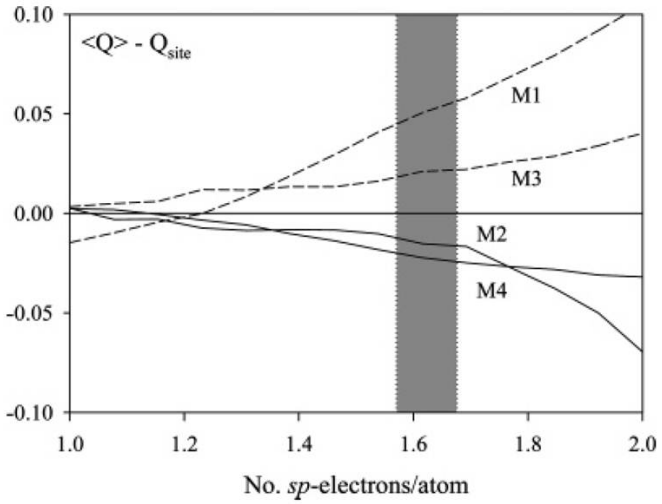

Fig. 1.12 Relative Mulliken populations for the four crystallographic sites [51].

There are other scientists devoted their efforts to the solid state chemistry of intermetallic compounds. The major work of Svilen Bobev recently focused on A–(Cd, Zn)–Pn phases, where A = Ca, Sr, Ba, Eu, Yb and Pn = As, Sb, Bi, such as Ca_2CdSb_2 and Yb_2CdSb_2 [55], $A_{21}Cd_4Bi_{18}$ (A = Sr, Ba, Eu) [56], and Ba_2ZnPn_2 [57]. Most of these pnictides are featured by edge-shared (Cd, Zn)Pn_4 tetrahedra and such one-dimensional structural units represent a new motif in the crystal

#

chemistry of the Zintl phases (Fig. 1.13). Arthur Mar consistently synthesized a series of antimonides and arsenides, including *RE*GaSb$_2$ (RE = La–Nd) [58], Ba$_5$Ti$_{12}$Sb$_{19+x}$ [59], RE$_{12}$Fe$_{57.5}$As$_{41}$ (RE = La, Ce) [60], that also exhibited a great diversity of structure forms. Other works like AeM$_x$In$_{4-x}$ (Ae = Sr, Ba; M = Mg, Zn) [61], RE$_6$Ge$_{5-x}$Sb$_{11+x}$ (RE = La–Nd, Sm, Gd–Dy) [62], M$_2$Ba$_2$Sn$_6$ (M = Yb, Ca) [63], Ti$_{1-\delta}$Mo$_{1+\delta}$As$_4$ and Ti$_{1-\delta}$Mo$_{1+\delta}$Sb$_4$ [64], K$_3$Au$_5$Tr (Tr = In, Tl) [65], and La$_2$NiAl$_7$ [66], which contains a variety of research interests, such as equilibrium phases, delocalized bonding, polar character, wide diversity in structure and bonding type, unusual valence rules and electronic structure, that motivates us to the exploratory synthesis of new intermetallic compounds. Accordingly, we performed systematically investigations in ternary Hf–M–M' systems (M, M' = Mn, Ni, Cu, Al, Ga, In, Si, Ge, Sb) (see appendix). In this thesis, we report the results of our studies.

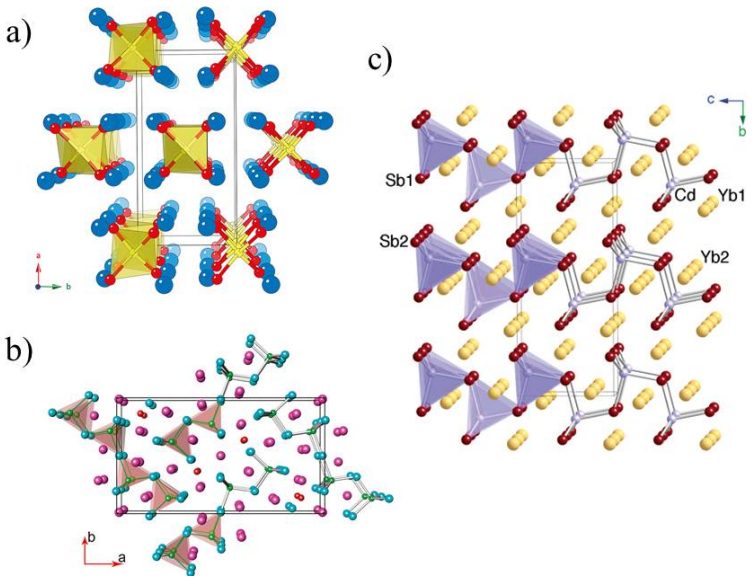

Fig. 1.13 Structures of (a) Ba$_2$ZnSb$_2$, (b) Yb$_9$Mn$_{4+x}$Sb$_9$, and (c) Yb$_2$CdSb$_2$ [55, 57, 67].

1.4 Research Scope

1.4.1 Hf–Cu–Al system

1.4.1.1 Laves phase

Laves phases exhibit intrinsic properties [68] that suggest their potential applications in superconducting materials, magnetic materials and metal hydride batteries [4, 69, 70]. Thousands of topologically close-packed compounds are classified within this family, with hexagonal $MgZn_2$ (C14), cubic $MgCu_2$ (C15), and hexagonal $MgNi_2$ (C36) structure types [14, 71]. The phase stability and structures of Laves structures are strongly affected by two factors: (i) atomic size (for binary Laves systems AB_2, the ideal radius ratio of the two atoms is ca. 1.225 and values of 1.05–1.68 occur in many surveys) [72], and (ii) concentration of valence electrons. For $Mg(Cu/Al)_2$ [73] and $Ca(Al/Li)_2$ [74] systems, the structures vary between C15, C36 and C14 types, accompanied by changes in the number of valence electrons [75]. For s-p bonded Laves compounds $CaAl_{2-x}Mg_x$, the structural transformation has been further studied by first-principles calculations considering especially moments of the electronic density of states on structure stability [76].

$HfAl_2$ [77] was reported as a Laves phase with the $MgZn_2$ structural type. The Al atom is replaceable by other metallic elements to form ternary compounds of the $MgCu_2$ {e.g. $HfAl_{1.65}$(Au, Cu, Ni)$_{0.35}$ [78, 79], $HfAl_{1.7}Co_{0.3}$ [80], $HfAg_{0.425}Al_{1.575}$ [81], $HfAl_{1.5}Zn_{0.5}$ [82], $HfAl_{0.1}Ni_{1.9}$ [83]} and $MgNi_2$ ($HfPd_{0.33}Al_{1.67}$, $HfPt_{0.36}Al_{1.64}$ [78]) types. No previous reports describe successive variations of the Laves structures in Hf–Cu–Al system. In this study, we systematically investigated the

changes in the Laves structures of the ternary system $HfAl_{2-x}Cu_x$ to determine the ranges of homogeneity and to characterize its new phases. We obtained several new phases that feature a measurable phase width and structural transformations triggered through substitution of Al atoms by Cu atoms. Here we report the synthesis, structural characterization, electrical resistivities, and electronic structures of three Laves phases within the system Hf–Cu–Al.

1.4.1.2 $Sc_{11}Ir_4$ phase

Hundreds of compounds comprising elements throughout the periodic table adopt [14] the structural type Th_6Mn_{23} [84]. Two possible compositions – $A_6B_{16}C_7$ or $A_6(B, C)_2$ – are observed in a ternary system, where A is an early transition metal or lanthanide, and B and C are elements from groups 7 to 15. Research on $M_6Fe_{16}Si_7$ (M = Ta, Nb) [85], $Mn_6Ni_{16}Si_7$ [86], $U_6Fe_{16}Si_7$ [87], $La_6Mg_{22}Al$ [88], $Y_6Fe_{23-x}Cr_x$ [89] include crystallographic measurements implemented with X-ray and neutron diffraction. The Th_6Mn_{23} prototype contains an interstitial position that can be either empty or filled with an atom of appropriate size. According to the literature, the filled compound of type Th_6Mn_{23}, known also as structural type $Sc_{11}Ir_4$ [90], occurs mostly in silicides or aluminides, including $U_6Fe_{16}Si_7C$ [91] and $Ln_3Pd_8Sb_4$ (Ln = Y, Gd, Tb, Dy, Ho, Er, Tm) [92].

Few ternary phases have been reported in the Hf–Cu–Al system [78, 92, 93] . During our investigation on structural variations of Laves phases $HfAl_{2-x}Cu_x$ [94], we obtained a compound characterized as $Hf_6Cu_{16}Al_{7.58}$, similar to $ZrCu_{16}Al_7$ [95]. Unlike the reported aluminides such as

#

$Ti_{26.88}Fe_{28}Al_{65.12}$ [96], $Ti_{45.7}Co_{30.4}Al_{43.9}$ [97], and $Ti_{37.9}Ru_{28}Al_{54.1}$ [98] , which feature a large proportion of Al and a mixed occupancy of various metals in the 4*b* site, $Hf_6Cu_{16}Al_{7.58}$ as synthesized contains little aluminium and the 4*b* site is filled partially with Al. Here we report the synthesis, structural characterization, electrical resistivity and electronic structure of a compound of type $Sc_{11}Ir_4$ in the Hf–Cu–Al system.

1.4.2 Hf–Al–Sb system

Ternary intermetallics of $T_5A_xB_{3-x}$ (T = early transition metal; A, B = group 13-15 elements) have been extensively investigated [14] because of their rich structural chemistry and tunable electronic properties. Much has been reported about the hexagonal Mn_5Si_3 structure with interesting physical properties including solid strength and hardness of silicide, aluminide, beryllide and chromide compounds [99], the stability of Nb_5Si_3 at high temperature [100], and the ability of Y_5Si_3 and ternary $Y_5(Si,Ge)_3$ to store hydrogen [101]. Structures in this family are correlated with similar polyhedra, that the Mn_5Si_3 type was composed of edge-shared trigonal prisms arranged along the [001] direction, whereas the prisms formed sheets of trigonal columns about (101) in the Y_5Bi_3-type structure [102]. Many ternary phases, such as in (Ti, Zr, Hf)-M-Sb systems, adopt W_5Si_3 structural form with substituted transition-metal atoms (M), including Ti_5CuSb_2 [103], $Zr_5Cu_{0.45}Sb_{2.55}$ [104], $Zr_5M_{0.5}Sb_{2.5}$ (M = Fe, Co, Ni, Ru, Rh) [105], $T_5M_{1-x}Sb_{2+x}$ (T = Ti, Zr, Hf; M = Fe, Co, Ni, Cu, Ru, Rh, Pd, Cd) [106], $Hf_5M_{1-x}Sb_{2+x}$ (M = V, Cr, Mn, Fe, Co, Ni, Cu) [107]. The transition metals show

#

a preference to occupy the 4*a* site according to the Brewer-Engel rules [108], and inhibition of local arrangement of Sb-Sb separation [109].

Besides these phases, compounds of W_5Si_3 type comprising early transition-metal and main-group elements are less available, only $M_5(Sn, Ga)_3$ (M = Nb, Ta) [110, 111], Ti_5XSb_2 (X = Al, Ga, In) [112], $Ti_5Si_{1.3}Sb_{1.7}$ [113] have been explored. To understand the structural diversity and their physical properties, we undertook exploratory experiments in the ternary Hf-Al-Sb system about which is less known than other phases.

We obtained several new phases that feature a measurable phase width and variation of structural types in the sequence Mn_5Si_3 → W_5Si_3 → Y_5Bi_3 as Al atoms were gradually replaced by Sb atoms in $Hf_5Al_{3-x}Sb_x$ reactions. Herein, we report their syntheses, crystal structures, band structures and physical properties.

1.4.3 Hf–Ni–Ga system

Intermetallic compounds of the ternary systems A–Ni–Ga (where A is a rare earth, alkali, alkaline earth, or early transition element) exhibit many different structures [14]. Among these phases, most belong to RE–Ni–Ga systems (RE = rare-earth metal), such as $RE_3Ni_6Ga_2$ [114], $RENiGa_3$ [115], $RE_4Ni_2Ga_{17}$ (RE = Ce, Nd) [116], $Eu_3Ni_4Ga_4$ [117], $RE_{15}Ni_{96-x}Ga_x$ [118], and $Yb_4Ni_{10+x}Ga_{21-x}$ [119]. In addition to their flexible compositions, these systems have been studied extensively for their phase transitions [120], the valence behavior of the electropositive atom [121], band-structures [122]

and intrinsic magnetic properties [123-125]. In contrast, only a few compounds have been reported that comprise elements of groups 1–3. For example, $CaNi_2Ga_3$ of $BaZn_5$ type, deformed from a $CaCu_5$ structure [126]; $Na_{10}NiGa_{10}$ featuring a three-dimensional net composed of $[Ga_{10}Ni]^{10-}$ gallium clusters [127]; $Sc_5(Ni, Ga)_{1.925}$ built through condensation of cuboctahedral and tricapped trigonal prisms [128]; and $Y(Ni, Ga)_2$, which transforms its structure between $CeCu_2$ and $CaIn_2$ types for various compositions [129].

For TM–Ni–Ga systems (TM = Ti, Zr, Hf), several compounds have been synthesized and their structures determined, including TMNiGa [130, 131], $TMNi_2Ga$ [132], $Ti_4Ni_2Ga_3$ [133], $Hf(Ni, Ga)_3$ [134] and $HfNiGa_2$ [135]. The unique structures revealed in compounds $TM_6Ni_8Ga_{15}$ [136] and $HfNi_{2.15}Ga_{3.85}$ [137] led us to explore new phases featuring large contents of nickel and gallium atoms. We have undertaken a systematic synthesis of new compounds in the ternary M–Ni–Ga system (M = Zr, Hf). Here, we report the synthesis, structures and calculated electronic structures of the intermetallic compounds $Hf_{13.0}Ni_{40.8}Ga_{30.9}$ and $Zr_{13.0}Ni_{40.6}Ga_{31.0}$. Each phase adopts hexagonal structure of $Y_{13}Pd_{40}Sn_{31}$-type with a complicated framework and atomic sites [138], and we discuss these structures in relation to those determined previously for $CaCu_5$-corresponding phases.

#

Chapter 2

Experiments

2.1 Synthesis

2.1.1 Hf–Cu–Al system

2.1.1.1 Laves phase

To seek new phases in the ternary system Hf–Cu–Al, Hf ingot (99.9%, Alfa Aesar), Al powder (99.99%, Alfa Aesar) and Cu powder (99.999%, Alfa Aesar) were combined in stoichiometric ratios (total mass: ca. 0.35 g) in a glove box under an atmosphere of N_2. Alloys of the type $HfAl_{2-x}Cu_x$ (nominal compositions: x = 0, 0.1, 0.2, …, 2.0) were effected on arc-melting samples on a water-cooled copper hearth under an Ar atmosphere. The samples were melted three times to ensure homogeneity; loss of mass was controlled to less than 3%. After these reactions, each compound was sealed in an evacuated silica tube and annealed at 1073 K for five days.

1.4.1.2 $Sc_{11}Ir_4$ phase

Hf ingot (99.9%, Alfa Aesar), Al powder (99.99%, Alfa Aesar) and Cu powder (99.999%, Alfa Aesar) were used to seek in the ternary system Hf–Cu–Al. The elements were combined in

#

stoichiometric ratios (total mass: ca. 0.35 g) in a glove box under an atmosphere of N_2 and cold pressed into pellets. The reactants were loaded in an alumina crucible and sealed within an evacuated fused-silica tube. The tube was heated from 300K to 1273K over 12 h; the latter temperature was maintained for 6 h before cooling to room temperature. The samples revealed a silver surface after being crushed into pieces; they were insensitive to air or moisture. Further crystal analyses, using powder X-ray diffraction, were performed after the target phases were obtained in pure form.

2.1.2 Hf–Al–Sb system

The starting materials for seeking new phases in the ternary system Hf-Al-Sb including hafnium ingot (99.9 %, Alfa Aesar), aluminum powder (99.99 %, Alfa Aesar) and antinomy powder (99.999 %, Alfa Aesar). The samples of total mass ~0.35 g in stoichiometric ratio with an excess of 0.05 g to 0.15g antimony were cold pressed into pellets within glove box of nitrogen atmosphere. Samples of $Hf_5Al_{3-x}Sb_x$ (nominal compositions x = 0, 0.5, 1.0, …, 3.0) were effected on arc-melting samples on a water-cooled copper hearth in an argon atmosphere. The samples were melted three times to ensure homogeneity and loss of mass was controlled to be less than 3 % of stoichiometric weight. After reaction, each sample was sealed in an evacuated silica tube and annealed at 1073 K for five days.

#

2.1.3 Hf–Ni–Ga system

To obtain new Hf-Ni-Ga phases, samples of a Hf ingot (99.9%, Alfa Aesar), Zr ingot (99.9%, Alfa Aesar), Ni powder (99.99%, Alfa Aesar), and Ga (99.999 %, Alfa Aesar) were combined (total mass ca. 0.35 g) with the elements in stoichiometric ratios in a glove box under an atmosphere of N_2. The reactions were effected through arc-melting of the samples on a water-cooled copper hearth under an Ar atmosphere. The samples were melted three times to ensure homogeneity; loss of mass was controlled to less than 3%. After these reactions, each sample was sealed in an evacuated silica tube and annealed at 1073 K for five days. The samples revealed a silver surface after being crushed into pieces; they were insensitive to air or moisture. Further crystal analyses, using powder X-ray diffraction, were performed after the target phases were obtained in pure form. The same processes were duplicated for the synthesis of the Zr compound.

2.2 Characterization

Powder X-ray diffraction data were collected on a Bragg–Brentano–type powder diffractometer (Bruker D8 Advance; operated at 40 kV and 40 mA; Cu Kα; λ = 1.5418 Å). For phase identification, all patterns were measured in a 2θ range from 5 to 60° with a step size of 0.05° and a counting period of 1 s/step. The patterns of the $MgNi_2$-type compounds were similar to those for $MgZn_2$-type compounds, but could be differentiated their (015) peak at angle of 2θ of 33°. Energy dispersive

spectra (SEM/EDX, Hitachi S-4700I high-resolution scanning electron microscope) were recorded using small pieces of samples to confirm that the levels of component elements were close to their weighted-in compositions.

2.3 X-ray Crystallography

Crystals suitable for X-ray diffraction experiments were selected under an optical microscope and then mounted on glass fibers. Crystal X-ray diffraction data were collected with the use of graphite-monochromatized Mo Kα radiation (λ = 0.71073 Å) at 298(2) K (Bruker APEX CCD diffractometer). The distance from the crystal to the detector was 5.038 cm. SMART software was used for data acquisition. Data were collected in an ω scan with steps of 0.3° and an exposure period of 20 s/frame; values of 2θ varied between 1.21 and 28.26°. The data were integrated (Siemens SAINT program) and corrected for Lorentz and polarization effects [139]. Absorption corrections made with SADABS [140] were based on fitting a function to the empirical transmission surface as sampled by multiple equivalent measurements of numerous reflections. The structural model was obtained using direct methods and refined with full-matrix least-square refinement based on F^2 using the SHELXTL package [21].

#

2.3.1 Hf–Cu–Al system

2.3.1.1 Laves phase

According to the powder XRD measurements, three crystals obtained from the nominal $HfAl_{2-x}Cu_x$ reactions for values of x of 0.5 (**I**), 0.9 (**II**) and 1.0 (**III**), respectively, were refined using $MgCu_2$, $MgNi_2$ and $MgZn_2$ structurs as starting models. For **I**, the structure was refined in space group $Fd\bar{3}m$ and yielded final R-factors (R_1, wR_2, GOF) were 0.0222, 0.0564, and 1.171, respectively, with the formula $HfAl_{1.51(2)}Cu_{0.49(2)}$. For **II** and **III**, the space groups were determined to be $P6_3/mmc$ and generated the formulas $HfAl_{1.12(3)}Cu_{0.88(3)}$ and $HfAl_{0.96(2)}Cu_{1.04(2)}$, respectively, with parameters R_1, wR_2, and GOF of 0.0367/0.1046/1.473 and 0.0321/0.0651/1.096, respectively. Crystallographic data for $HfAl_{1.51}Cu_{0.49}$, $HfAl_{1.12}Cu_{0.88}$, and $HfAl_{0.96}Cu_{1.04}$ are provided in Table 2.1. The refined positional parameters and important bond lengths are listed in Tables 2.2 and 2.3, respectively.

Table 2.1 Crystal Data and Conditions of Data Collection for $HfAl_{1.51(2)}Cu_{0.49(2)}$, $HfAl_{1.12(3)}Cu_{0.88(3)}$ and $HfAl_{0.96(2)}Cu_{1.04(2)}$

Refined composition	$HfAl_{1.51(2)}Cu_{0.49(2)}$	$HfAl_{1.12(3)}Cu_{0.88(3)}$	$HfAl_{0.96(2)}Cu_{1.04(2)}$
Formula weight (g/mol)	250.00	264.63	270.48
Instrument; Temperature	Bruker APEX CCD; 298(2)		
Wavelength	0.71073 Å		
Crystal system	cubic	hexagonal	hexagonal
Space group, *Z*	$Fd\bar{3}\,m$ (227), 8	$P6_3/mmc$ (194), 8	$P6_3/mmc$ (194), 4
a (Å)	7.3430(8)	5.1641(7)	5.1567(7)
c (Å)		16.763(3)	8.3211(17)
V ($Å^3$)	395.93(7)	387.15(11)	191.63(5)
$d_{calcd.}$ (g/cm^3)	8.412	8.980	9.324
Absorption coefficient (mm^{-1})	58.058	62.444	65.146
Refinement method	Full-matrix least-squares on F^2		
Goodness-of-fit on F^2	0.994	1.473	1.096
R_1, wR_2 (all data)[a]	0.0219, 0.0680	0.0367, 0.1046	0.0321, 0.0651
R_1, wR_2 ($I > 2\sigma(I)$)	0.0219, 0.0680	0.0307, 0.1014	0.0273, 0.0626

[a] $R_1 = \Sigma||F_o| - |F_c||/\Sigma|F_o|$, $wR_2 = [\Sigma w(F_o^2 - F_c^2)^2 / \Sigma w(F_o^2)^2]^{1/2}$

Table 2.2 Atomic Coordinates, Site Occupancies and Isotropic Displacement Parameters (U_{eq}, 10^{-3} $Å^2$) for $HfAl_{1.51}Cu_{0.49}$, $HfAl_{1.12}Cu_{0.88}$ and $HfAl_{0.96}Cu_{1.04}$

	Atom	Site	x	y	z	U_{eq}[a]	Site occ.	
$HfAl_{1.51}Cu_{0.49}$	Hf(1)	8*a*	0.125	0.125	0.125	6(1)		
	M(1)	16*d*	0.5	0.5	0.5	9(2)	Al	0.76
							Cu	0.24(2)
$HfAl_{1.12}Cu_{0.88}$	Hf(1)	4*e*	0	0	0.4047(1)	8(1)		
	Hf(2)	4*f*	0.3333	0.6667	0.6562(1)	8(1)		
	M(1)	4*f*	0.3333	0.6667	0.3724(3)	12(2)	Al	0.610
							Cu	0.39(7)
	M(2)	6*h*	0.1622(5)	0.3244(10)	0.25	11(1)	Al	0.51
							Cu	0.49(6)
	M(3)	6*g*	0	0.5	0.5	13(2)	Al	0.54
							Cu	0.46(7)
$HfAl_{0.96}Cu_{1.04}$	Hf(1)	4*f*	0.3333	0.6667	0.0641(1)	9(1)		
	M(1)	2*a*	0	0	0	11(2)	Al	0.53
							Cu	0.47(2)
	M(2)	6*h*	0.1707(2)	0.3415(6)	0.25	7(1)	Al	0.46
							Cu	0.54(1)

[a] U_{eq} is defined as one third of the trace of the orthogonalized U_{ij} tensor.

Table 2.3 Interatomic Distances (Å) for $HfAl_{1.51}Cu_{0.49}$, $HfAl_{1.12}Cu_{0.88}$ and $HfAl_{0.96}Cu_{1.04}$

$HfAl_{1.51}Cu_{0.49}$		Distance (Å)	$HfAl_{1.12}Cu_{0.88}$		Distance (Å)
Hf(1)	-Hf(2)×4	3.180(1)	Hf(1)	-Hf(1)	3.105(1)
	-M(1)×12	3.044(3)		-Hf(2)x3	3.166(2)
M(1)	-M(1)x6	2.596(3)		-M(1)x3	3.038(1)
				-M(2)x3	2.951(2)
				-M(3)x6	3.013(1)
$HfAl_{0.96}Cu_{1.04}$		Distance (Å)	Hf(2)	-Hf(2)	3.144(2)
Hf(1)	-Hf(1)x3	3.163(2)		-M(1)x3	3.020(2)
	-Hf(1)	3.093(1)		-M(2)x6	3.028(1)
	-M(1)x3	3.025(1)		-M(3)x3	3.013(2)
	-M(2)x6	3.001(1)	M(1)	-M(2)x3	2.560(1)
	-M(2)x3	2.990(1)		-M(3)x3	2.607(1)
M(1)	-M(2)x2	2.579(2)	M(2)	-M(2)x2	2.512(1)
M(2)	-M(2)x2	2.516(4)		-M(2)x2	2.651(2)
	-M(2)x2	2.641(4)	M(3)	-M(3)x4	2.582(2)

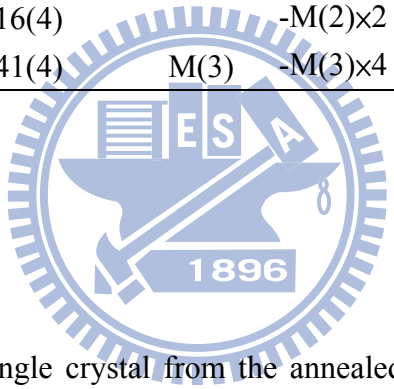

2.3.1.2 $Sc_{11}Ir_4$ phase

We selected irregularly shaped single crystal from the annealed samples to collect crystal X-ray diffraction data to perform structure refinements. Using direct methods, we built a structural model with 6 crystallographic sites, which was consistent to $Sc_{11}Ir_4$ structure type. The positions with heavier electron density were assigned to Hf atoms and others, except 4*b* site, were assigned to Cu and Al atoms according to the site occupancy. With no unexpected element was detected in EDX experiment, the refinement finally assumed the deficient electron density in 4*b* position as Al atom with occupancy of 0.57(15), generating the formula $Hf_6Cu_{16}Al_{7.58(3)}$ with parameters R_1, wR_2, and *GOF* of 0.0329/0.0844/1.400. The crystallographic data are provided in Table 2.4. The refined

positional parameters and important bond lengths are listed in Tables 2.5 and 2.6, respectively.

Table 2.4 Crystal Data and Conditions of Data Collection for $Hf_6Cu_{16}Al_{7.58}$

Refined composition	$Hf_6Cu_{16}Al_{7.58}$
Formula weight (g/mol)	2292.20
Instrument; Temperature	Smart CCD; 298(2)
Wavelength	0.71073 Å
Crystal system	cubic
Structure type	$Sc_{11}Ir_9$
Space group, Z	$Fm\bar{3}m$ (225), 8
a (Å)	11.8895(14)
V (Å^3)	1680.7(3)
$d_{calcd.}$ (g/cm^3)	9.058
Absorption coefficient (mm^{-1})	56.980
Refinement method	Full-matrix least-squares on F^2
Goodness-of-fit on F^2	1.400
R_1, wR_2 (all data)[a]	0.0329, 0.0844
R_1, wR_2 ($I > 2\sigma(I)$)	0.0329, 0.0844

[a] $R_1 = \Sigma||F_o| - |F_c||/\Sigma|F_o|$, $wR_2 = [\Sigma w(F_o^2 - F_c^2)^2 / \Sigma w(F_o^2)^2]^{1/2}$

Table 2.5 Atomic Coordinates, Site Occupancies and Isotropic Displacement Parameters (U_{eq}, 10^{-3} Å^2) for $Hf_6Cu_{16}Al_{7.58}$

	Atom	Site	x	y	z	U_{eq}[a]	Site occ.	
$Hf_6Cu_{16}Al_{7.58}$	Hf(1)	24*e*	0.3003	0	0	4(1)		
	Cu(1)	32*f*	0.1190	0.1190	0.1190	4(1)		
	Cu(2)	32*f*	0.3298	0.3298	0.3298	6(1)		
	Al(1)	4*a*	0	0	0	1(4)		
	Al(2)	4*b*	0.5	0.5	0.5	30(20)	Al	0.57(15)
	Al(3)	24*d*	0	0.25	0.25	2(2)		

[a] U_{eq} is defined as one third of the trace of the orthogonalized U_{ij} tensor.

Table 2.6 Interatomic Distances (Å) for $Hf_6Cu_{16}Al_{7.58}$

Hf(1)	-Cu(1)*4	2.9409(11)	Cu(1)	-Al(1)*8	2.451(3)
	-Cu(2)*4	2.883(2)	Cu(1)	-Al(3)*4	2.6179(13)
Hf(1)	-Al(2)*6	2.3746(13)	Cu(2)	-Al(3)*4	2.4280(3)
Cu(1)	-Cu(1)*3	2.830(4)			
Cu(1)	-Cu(2)*3	2.650(3)			
Cu(2)	-Cu(2)*3	2.683(5)			

2.3.2 Hf–Al–Sb system

The structure refinements were performed using the structure models of Mn_5Si_3 and W_5Si_3 as starting models. The positions with heavier electron density were assigned to Hf atoms and others were assumed to be mixtures of Al and Sb atoms. The final *R* factors *R1*, *wR2*, and *GOF* were 0.0310/0.0710/1.163, 0.0369/0.0920/1.143, and 0.0223/0.0555/1.329, respectively, with the formulas $Hf_5Al_{2.30(2)}Sb_{0.70(2)}$, $Hf_5Al_{1.56(2)}Sb_{1.44(2)}$, and $Hf_5Al_{0.86(3)}Sb_{2.04(3)}$, respectively. The crystallographic data are provided in Table 2.7 and Table 2.8. The refined positional parameters and important bond lengths are listed in Tables 2.9 and 2.10, respectively.

Table 2.7 Crystal Data and Conditions of Data Collection for $Hf_5Al_{2.30}Sb_{0.70}$

Refined composition	$Hf_5Al_{2.30}Sb_{0.70}$
Formula weight (g/mol)	1039.734
Instrument; Temperature	Smart CCD; 298(2)
Wavelength	0.71073 Å
Crystal system	hexagonal
Structure type	Mn_5Si_3
Space group, *Z*	*P6₃/mcm* (193), 8
a (Å)	8.1442(12)
c (Å)	5.6566(11)
V (Å^3)	324.92(9)
$d_{calcd.}$ (g/cm^3)	10.627
Absorption coefficient (mm^{-1})	40.896
Refinement method	Full-matrix least-squares on F^2
Goodness-of-fit on F^2	1.163
R_1, wR_2 (all data)[a]	0.0310, 0.0710
R_1, wR_2 ($I > 2\sigma(I)$)	0.0290, 0.0692

[a] $R_1 = \Sigma||F_o| - |F_c||/\Sigma|F_o|$, $wR_2 = [\Sigma w(F_o^2 - F_c^2)^2 / \Sigma w(F_o^2)^2]^{1/2}$

Table 2.8 Crystal Data and Conditions of Data Collection for $Hf_5Al_{1.56}Sb_{1.44}$ and $Hf_5Al_{0.86}Sb_{2.14}$

Refined composition	$Hf_5Al_{1.56}Sb_{1.44}$	$Hf_5Al_{0.86}Sb_{2.14}$
Formula weight (g/mol)	1109.870	1176.213
Instrument; Temperature	Smart CCD; 298(2)	
Wavelength	0.71073 Å	
Crystal system	tetragonal	tetragonal
Structure type	W_5Si_3	W_5Si_3
Space group, *Z*	*I*4/*mcm* (140), 8	*I*4/*mcm* (140), 8
a (Å)	10.8955(15)	10.9296(15)
c (Å)	5.5101(11)	5.5355(11)
V (Å^3)	654.11(18)	661.25(18)
$d_{calcd.}$ (g/cm^3)	10.846	11.814
Absorption coefficient (mm^{-1})	41.607	42.608
Refinement method	Full-matrix least-squares on F^2	
Goodness-of-fit on F^2	1.143	1.329
R_1, wR_2 (all data)[a]	0.0396, 0.0920	0.0223, 0.0555
R_1, wR_2 ($I > 2\sigma(I)$)	0.0391, 0.0915	0.0227, 0.0554

[a] $R_1 = \Sigma||F_o| - |F_c||/\Sigma|F_o|$, $wR_2 = [\Sigma w(F_o^2 - F_c^2)^2 / \Sigma w(F_o^2)^2]^{1/2}$

Table 2.9 Atomic Coordinates, Site Occupancies and Isotropic Displacement Parameters (U_{eq}, 10^{-3} Å^2) for $Hf_5Al_{2.30}Sb_{0.70}$, $Hf_5Al_{1.56}Sb_{1.44}$ and $Hf_5Al_{0.86}Sb_{2.14}$

	Atom	Site	x	y	z	U_{eq}[a]	Site occ.	
$Hf_5Al_{2.30}Sb_{0.70}$	Hf(1)	4*d*	0.3333	0.6667	0	9(1)		
	Hf(2)	6*g*	0.7591(1)	0	0.25	7(1)		
	M	6*g*	0.3936(4)	0	0.25	7(1)	Al	0.766
							Sb	0.234(9)
$Hf_5Al_{1.56}Sb_{1.44}$	Hf(1)	4*b*	0	0.5	0.25	7(1)		
	Hf(2)	16*k*	0.0766(1)	0.2182(1)	0.5	6(1)		
	M(1)	4*a*	0	0	0.25	9(3)	Al	0.92
							Sb	0.08(1)
	M(2)	8*h*	0.1643(1)	0.3358(1)	0	5(1)	Al	0.32
							Sb	0.68(1)
$Hf_5Al_{0.86}Sb_{2.14}$	Hf(1)	4*b*	0	0.5	0.25	4(1)		
	Hf(2)	16*k*	0.0757(1)	0.2181(1)	0	4(1)		
	M(1)	4*a*	0	0	0.25	3(1)	Al	0.76
							Sb	0.24(1)
	M(2)	8*h*	0.1645(1)	0.3356(1)	0.5	4(1)	Al	0.05
							Sb	0.951(7)

[a] U_{eq} is defined as one third of the trace of the orthogonalized U_{ij} tensor.

Table 2.10 Interatomic Distances (Å) for $Hf_5Al_{2.30}Sb_{0.70}$, $Hf_5Al_{1.56}Sb_{1.44}$ and $Hf_5Al_{0.86}Sb_{2.14}$

$Hf_5Al_{2.30}Sb_{0.70}$		Distance (Å)
Hf(1)	-Hf(1)*2	2.8283(5)
	-M(1)*6	2.877(1)
Hf(2)	-M(1)*2	2.799(2)

$Hf_5Al_{1.56}Sb_{1.44}$		Distance (Å)
Hf(1)	-Hf(1)*2	2.7550(5)
Hf(1)	-M(1)*4	2.881(1)
Hf(2)	-M(1)*2	2.883(1)
	-M(2)	2.920(1)
	-M(2)	2.8716(7)
M(1)	-M(1)*2	2.7551(5)

$Hf_5Al_{0.86}Sb_{2.14}$		Distance (Å)
Hf(1)	-Hf(1)*2	2.7678(5)
Hf(1)	-M(1)*4	2.894(1)
Hf(2)	-M(1)*2	2.8774(5)
	-M(2)	2.9223(7)
	-M(2)	2.899(1)
M(1)	-M(1)*2	2.7678(5)

2.3.3 Hf–Ni–Ga system

The structural refinements are detailed in Chapter 6. Crystallographic data for $Hf_{13.0}Ni_{40.8}Ga_{30.9}$ and $Zr_{13.0}Ni_{40.6}Ga_{31.0}$ are provided in Table 2.11. The refined positional parameters and important bond lengths are listed in Table 2.12 – 2.15.

Table 2.11 Crystal Data and Conditions of Data Collection for $Hf_{13.0}Ni_{40.8}Ga_{30.9}$ and $Zr_{13.0}Ni_{40.6}Ga_{31.0}$

refined composition	$Hf_{13}Ni_{40.8}Ga_{31}$	$Zr_{13.0}Ni_{40.6}Ga_{31.0}$
formula weight (g/mol)	6852.89	5733.15
instrument; temperature	Smart CCD; 293(2)	
wavelength	0.71073 Å	
crystal system	hexagonal	
space group, *Z*	*P6/mmm* (191), 2	*P6/mmm* (191), 2
a /Å	17.895(3)	17.964(3)
c /Å	8.2434(16)	8.2757(17)
V /Å^3	2286.0(6)	2312.7(7)
$d_{calcd.}$ / g cm^{-3}	9.955	8.232
refinement method	full-matrix least-squares on F1/2	
goodness of fit on F2	1.141	1.088
R_1, wR_2 (all data)[a]	0.0299, 0.0598	0.0348, 0.0686
R_1, wR_2 (I > 2σ(I))	0.0262, 0.0575	0.0285, 0.0641
largest diff. peak and hole /e Å^{-3}	3.595, -3.387	2.126, -2.660

[a] $R_1 = \Sigma||F_o| - |F_c||/\Sigma|F_o|$, $wR_2 = [\Sigma w(F_o^2 - F_c^2)^2 / \Sigma w(F_o^2)^2]^{1/2}$

Table 2.12 Atomic Coordinates and Isotropic Displacement Parameters (U_{eq} / 10^{-3} Å^2) for $Hf_{13.0}Ni_{40.8}Ga_{30.9}$

atom	Wyckoff	*x*	*y*	*z*	U_{eq}[a]	site occ.
Hf(1)	*2e*	0	0	0.2964(2)	17(1)	
Hf(2)	*6l*	0.2426(1)	0.4852(1)	0	7(1)	
Hf(3)	*6m*	0.1488(1)	0.5744(1)	0.5	8(1)	
Hf(4)	*12n*	0.2722(1)	0	0.2930(1)	7(1)	
Ga(1)	*2d*	0.3333	0.6667	0.5	9(1)	
Ga(2)	*6i*	0.5	0	0.2598(2)	8(1)	
Ga(3)	*6j*	0.3871(1)	0	0	13(1)	
Ga(4)	*6j*	0.1641(2)	0	0	29(1)	0.0948(8)
Ga(5)	*6k*	0.1426(1)	0	0.5	8(1)	
Ga(6)	*12o*	0.6070(1)	0.2140(1)	0.1830(1)	9(1)	
Ga(7)	*12o*	0.1781(1)	0.3562(1)	0.2387(1)	7(1)	
Ga(8)	*12q*	0.1279(1)	0.4088(1)	0.5	6(1)	
Ni(1)	*2c*	0.3333	0.6667	0	11(1)	
Ni(2)	*6k*	0.4189(1)	0	0.5	7(1)	
Ni(3)	*6l*	0.5453(1)	0.0906(1)	0	11(1)	
Ni(4)	*6m*	0.1385(1)	0.2770(1)	0.5	6(1)	
Ni(5)	*12o*	0.2609(1)	0.5218(1)	0.3444(2)	8(1)	
Ni(6)	*12o*	0.0908(1)	0.1815(1)	0.2372(2)	10(1)	
Ni(7)	*12p*	0.0879(1)	0.3232(1)	0	16(1)	
Ni(8)	*24r*	0.1046(1)	0.4476(1)	0.2256(1)	9(1)	
Ni(9)	*1a*	0	0	0	10[b]	0.129(15)
Ni(10)	*2e*	0	0	0.0870(10)	10[b]	0.118(9)
Ni(11)	*6j*	0	0.0642(9)	0	43(5)	0.174(8)

[a] U_{eq} is defined as one third of the trace of the orthogonalized U_{ij} tensor.

[b] The parameter was manually fixed

Table 2.13 Interatomic Distances (Å) for $Hf_{13.0}Ni_{40.8}Ga_{30.9}$

Hf(1)	-Ni(6)×6	2.8549(14)	Ga(1)	-Ni(5)×6	2.5862(13)
Hf(2)	-Ga(6)×4	2.8988(8)	Ga(2)	-Ni(2)×2	2.4554(17)
	-Ga(7)×2	2.8057(12)		-Ni(3)×2	2.5606(17)
	-Ni(1)	2.8125(7)		-Ni(8)×4	2.4922(10)
	-Ni(5)×2	2.8950(14)	Ga(3)	-Ni(3)×2	2.4599(18)
	-Ni(7)×2	2.8359(16)		-Ni(7)×2	2.363(2)
	-Ni(8)×4	2.8897(10)		-Ni(8)×4	2.4705(10)
Hf(3)	-Ga(1)	2.8599(7)	Ga(4)	-Ni(6)×4	2.4598(13)
	-Ga(6)×2	2.8023(12)		-Ni(7)×2	2.470(3)
	-Ga(8)×2	2.7953(11)	Ga(5)	-Ni(4)×2	2.4431(17)
	-Ni(2)×2	2.7249(11)		-Ni(6)×4	2.5856(13)
	-Ni(5)×4	2.9061(8)	Ga(6)	-Ni(1)	2.3860(11)
Hf(4)	-Ga(5)	2.8797(13)		-Ni(3)	2.4360(19)
	-Ga(7)×2	2.7971(6)		-Ni(5)×2	2.4659(13)
	-Ga(8)×2	2.9205(10)		-Ni(8)×2	2.5510(12)
	-Ni(4)×2	2.9745(5)	Ga(7)	-Ni(4)	2.4785(14)
	-Ni(6)×2	2.8490(9)		-Ni(5)	2.7104(17)
	-Ni(7)×2	2.7758(9)		-Ni(6)	2.7063(17)
	-Ni(8)×4	2.7916(11)		-Ni(7)×2	2.4234(13)
				-Ni(8)×2	2.5646(11)
Ni(3)	-Ni(8)×4	2.6476(10)	Ga(8)	-Ni(2)	2.3834(15)
Ni(4)	-Ni(6)×2	2.6238(17)		-Ni(4)	2.4587(18)
Ni(5)	-Ni(5)	2.566(3)		-Ni(5)×2	2.5663(15)
	-Ni(8)×2	2.6143(12)		-Ni(8)×2	2.4631(11)
Ni(6)	-Ni(6)×2	2.8129(14)			
Ni(7)	-Ni(7)×2	2.638(3)	Ga(5)	-Ga(5)×2	2.5509(16)
		2.724(3)	Ga(7)	-Ga(8)×2	2.6795(12)
			Ga(8)	-Ga(8)	2.739(2)

Table 2.14 Atomic Coordinates and Isotropic Displacement Parameters (U_{eq} / 10^{-3} Å^2) for $Zr_{13.0}Ni_{40.6}Ga_{31.0}$

atom	Wyckoff	*x*	*y*	*z*	U_{eq}[a]	site occ.
Zr(1)	*2e*	0	0	0.2923(4)	24(1)	
Zr(2)	*6l*	0.2427(1)	0.4854(1)	0	7(1)	
Zr(3)	*6m*	0.1487(1)	0.5743(1)	0.5	8(1)	
Zr(4)	*12n*	0.2720(1)	0	0.7077(1)	8(1)	
Ga(1)	*2d*	0.3333	0.6667	0.5	9(1)	
Ga(2)	*6i*	0.5	0	0.2593(2)	9(1)	
Ga(3)	*6j*	0.3871(1)	0	0	11(1)	
Ga(4)	*6j*	0.1641(1)	0	0	28(1)	
Ga(5)	*6k*	0.1425(1)	0	0.5	9(1)	
Ga(6)	*12o*	0.6071(1)	0.2143(1)	0.1836(1)	10(1)	
Ga(7)	*12o*	0.1782(1)	0.3565(1)	0.2393(1)	7(1)	
Ga(8)	*12q*	0.1279(1)	0.4086(1)	0.5	7(1)	
Ni(1)	*2c*	0.3333	0.6667	0	10(1)	
Ni(2)	*6k*	0.4185(1)	0	0.5	8(1)	
Ni(3)	*6l*	0.5455(1)	0.0909(1)	0	11(1)	
Ni(4)	*6m*	0.1383(1)	0.2766(1)	0.5	7(1)	
Ni(5)	*12o*	0.2607(1)	0.5214(1)	0.3451(2)	9(1)	
Ni(6)	*12o*	0.0906(1)	0.1812(1)	0.2378(2)	12(1)	
Ni(7)	*12p*	0.0882(1)	0.3234(1)	0	16(1)	
Ni(8)	*24r*	0.1048(1)	0.4481(1)	0.2257(1)	9(1)	
Ni(9)	*1a*	0	0	0.0770(20)	10[b]	0.120(6)
Ni(10)	*2e*	0	0	0.4140(10)	10[b]	0.074(6)
Ni(11)	*6j*	0.0353(4)	0.0707(9)	0	68(5)	0.178(6)

Table 2.15 Interatomic distances (Å) for $Zr_{13.0}Ni_{40.6}Ga_{31.0}$

Zr(1)	-Ni(6)×6	2.8546(14)	Ga(1)	-Ni(5)×6	2.5985(12)
Zr(2)	-Ga(6)×4	2.9105(10)	Ga(2)	-Ni(2)×2	2.4719(14)
	-Ga(7)×2	2.8180(13)		-Ni(3)×2	2.5702(15)
	-Ni(1)	2.8206(12)		-Ni(8)×4	2.4989(9)
	-Ni(5)×2	2.9102(13)	Ga(3)	-Ni(3)×2	2.4735(16)
	-Ni(7)×2	2.8447(17)		-Ni(7)×2	2.3729(18)
	-Ni(8)×4	2.9009(9)		-Ni(8)×4	2.4835(9)
Zr(3)	-Ga(1)	2.8730(12)	Ga(4)	-Ni(6)×4	2.4730(11)
	-Ga(6)×2	2.8104(11)		-Ni(7)×2	2.482(2)
	-Ga(8)×2	2.8113(10)	Ga(5)	-Ni(4)×2	2.4465(15)
	-Ni(2)×2	2.7369(13)		-Ni(6)×4	2.5903(11)
	-Ni(5)×4	2.9177(10)	Ga(6)	-Ni(1)	2.3957(10)
Zr(4)	-Ga(5)	2.8921(14)		-Ni(3)	2.4476(17)
	-Ga(7)×2	2.8085(6)		-Ni(5)×2	2.4776(11)
	-Ga(8)×2	2.8106(11)		-Ni(8)×2	2.5564(11)
	-Ni(4)×2	2.9877(7)	Ga(7)	-Ni(4)	2.4907(12)
	-Ni(6)×2	2.8574(10)		-Ni(5)	2.7111(15)
	-Ni(7)×2	2.7842(11)		-Ni(6)	2.7267(16)
	-Ni(8)×4	2.8106(11)		-Ni(7)×2	2.4347(11)
				-Ni(8)×2	2.5758(10)
Ni(3)	-Ni(8)×4	2.6542(9)	Ga(8)	-Ni(2)	2.3926(13)
Ni(4)	-Ni(6)×2	2.6284(15)		-Ni(4)	2.4691(16)
Ni(5)	-Ni(5)	2.564(2)		-Ni(5)×2	2.5711(13)
	-Ni(8)×2	2.6208(11)		-Ni(8)×2	2.4755(10)
Ni(6)	-Ni(6)×2	2.8188(13)			
Ni(7)	-Ni(7)×2	2.744(2)	Ga(5)	-Ga(5)×2	2.5596(14)
		2.640(2)	Ga(7)	-Ga(8)×2	2.6819(10)
			Ga(8)	-Ga(8)	2.7433(19)

2.4 Measurements of physical properties

Electrical conductivity was measured using a standard four-probe method under vacuum (ca. 1.33 Pa) in the temperature range 30–700 K. Each sample was prepared by compressing the ground powder into a $1 \times 1 \times 5$ mm^3 bar and then annealing it at 1073 K for five days to minimize the effect of grain boundaries in the crystalline powder. The electrical contacts comprised four Cu wires attached to the bulk with silver glue. Samples were placed under vacuum at a temperature near 295 K for at least 1 h to allow the silver glue to dry completely, thereby improving the contact performance.

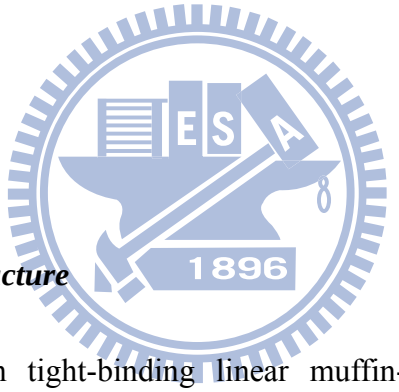

2.5 Calculations of electronic structure

Band structure calculations with tight-binding linear muffin-tin orbitals (LMTO) using the atomic-sphere approximation (ASA) were undertaken to assess the electronic structures [31, 141-144]. Density functional theory was employed with the local density approximation (LDA) for the exchange correlation energy. The electronic structures were analyzed by extracting information from the band structure, densities of states (DOS), and crystal orbital hamiltonian population (COHP) [145].

#

2.5.1.1 Laves phase

Three model structures were proposed with experimentally revealed compositions: $HfAl_{1.5}Cu_{0.5}$ of type $MgCu_2$; $HfAl_{1.25}Cu_{0.75}$ of type $MgNi_2$; and HfAlCu of type $MgZn_2$. The symmetries of the structural models were all reduced to *P*1 and the sites were assigned to match the stoichiometric formulae to simulate the mixed Al/Cu site occupancies. The orbitals used for calculation included Al 3s, 3p, and 3d, Cu 4s, 4p, and 3d, and Hf 6s, 6p, and 5d; Hf 4f orbitals were treated as core orbitals. Integration in reciprocal space was performed with an improved tetrahedral method using 220 *k* points for the $MgCu_2$ type and 210 *k* points for the $MgZn_2$ and $MgNi_2$ types in the irreducible part of Brillouin zone.

2.5.1.2 $Sc_{11}Ir_4$ phase

The orbitals used in the calculation included Al 3s, 3p and 3d, Cu 4s, 4p and 3d, and Hf 6s, 6p and 5d; Hf 4f orbitals were treated as core orbitals. Integration in the reciprocal space was performed with an improved tetrahedron method using 144 *k* points in the irreducible part of the Brillouin zone.

2.5.2 Hf–Al–Sb system

The orbitals used in the calculation included 3s, 3p and 3d of Al; 5s, 5p and 4d of Sb; and 6s, 6p and 5d of Hf with 4f treated as core orbitals. Integration in reciprocal space was performed with an

improved tetrahedron method using 176 *k*-points in the irreducible part of the Brillouin zone for model of Mn_5Si_3 type and 189 *k*-points for W_5Si_3 type.

2.5.3 Hf–Ni–Ga system

The orbitals used in the calculations included 4s, 4p, and 3d of Ga; 4s, 4p, and 3d of Ni; and 6s, 6p, and 5d of Hf with 4f treated as core orbitals. Integration in reciprocal space was performed with an improved tetrahedron method using 144 *k* points in the irreducible part of the Brillouin zone.

#

Chapter 3

Structural Variations in the Ternary System $HfAl_{2-x}Cu_x$ (x = 0.2–1.0)

Results and Discussion

3.1 Synthesis

We found Laves compounds in a series of reaction $HfAl_{2-x}Cu_x$, where x ranged from 0 to 2 in steps of 0.1. Based on the PXRD patterns, several phases were obtained through the concentration line and listed in Table 3.1. At values of x of 0 and 0.3, the patterns exhibited single-phase $MgZn_2$ (Fig. 3.1a) and $MgCu_2$ (Fig. 3.1c) structure types, respectively; consistent with the literature reports for the compounds $HfAl_2$ [77] and $HfAl_{1.65}Cu_{0.35}$ [78]. In addition, two distinct phase width regions, within the ranges $0.2 \leq x \leq 0.5$ and $0.7 < x < 0.9$, were recognized as $MgCu_2$ and $MgNi_2$ structure types, respectively. When x was larger than or equal to 1, however, the powder pattern exhibited a mixture of products (Fig. 3.1f), and we identified only two phases with $MgZn_2$ and $Sc_{11}Ir_9$ [90] structure types. The hypothetical binary Laves phase $HfCu_2$ was not obtained from reaction with a value of x of 2; instead, Hf_3Cu_8 [146] and unknown phases were formed.

#

Table 3.1 Phases observed from powder XRD patterns with starting reaction $HfAl_xCu_{2-x}$

x =	0	0.1	0.2	0.3	0.4	0.5	0.6
$MgZn_2$ phase	+	+					
$MgCu_2$ phase		+	+	+	+	+	+
$MgNi_2$ phase							+
other phases		+					
Hf_3Cu_8							

	0.7	0.8	0.9	1.0	1.1> x >1.9	2.0
$MgZn_2$ phase				+	+[b]	
$MgCu_2$ phase						
$MgNi_2$ phase	+	+	+			
other phases				+[a]	+	
Hf_3Cu_8						+

[a.] difficult to define because of overlapped peaks of mixtures

[b.] pattern of $MgZn_2$ phase disappeared as x > 1.1

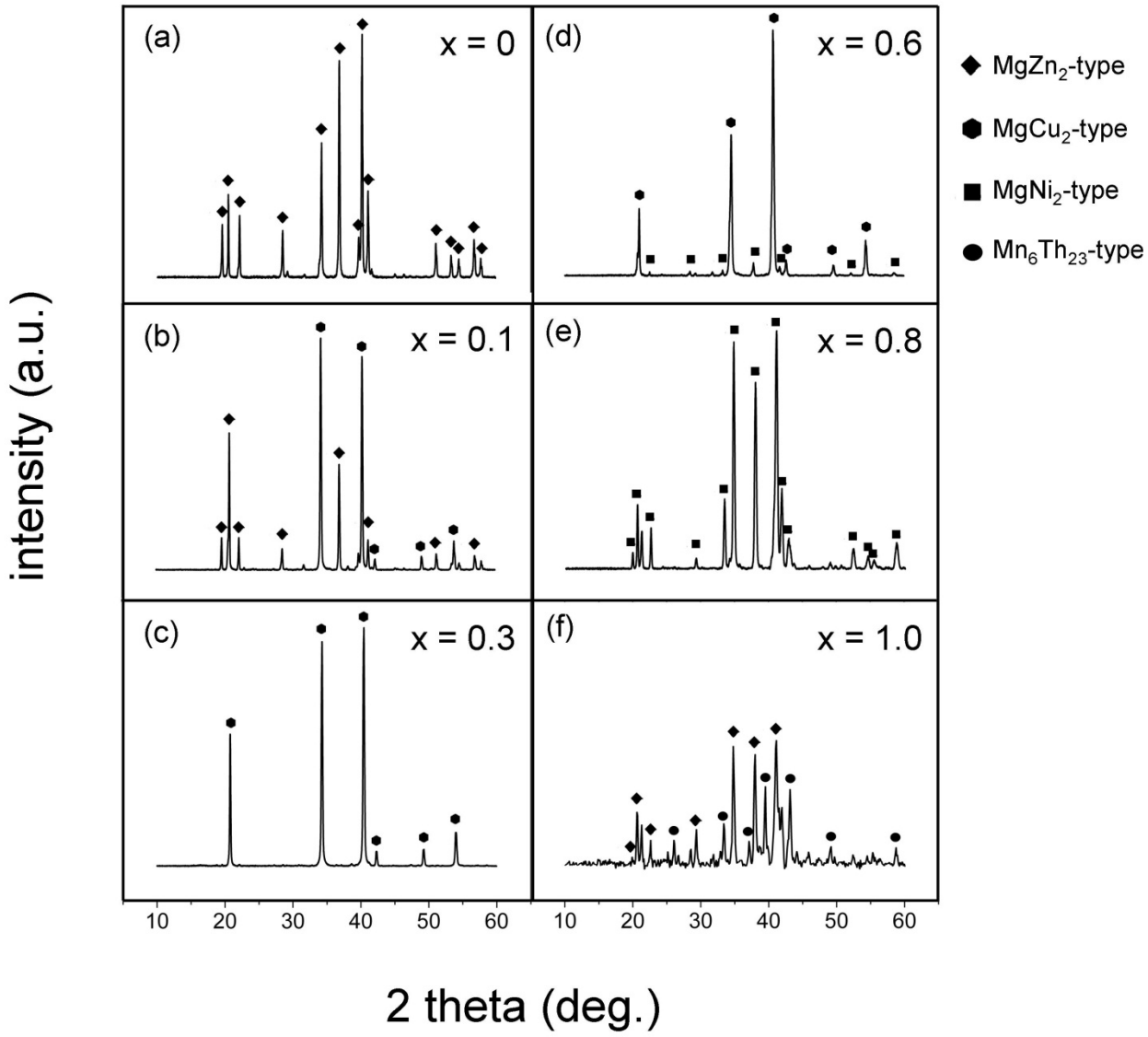

Fig. 3.1 Experimental X-ray powder patterns for $HfAl_{2-x}Cu_x$, with x = (a)0, (b)0.1, (c)0.3, (d)0.6, (e)0.8, and (f)1.0.

Judging from PXRD measurements, the Laves structures appeared in the sequence of types $MgZn_2$ → $MgCu_2$ → $MgNi_2$ → $MgZn_2$ within the range $0 \leq x \leq 1$ for the compositions $HfAl_{2-x}Cu_x$. For the pattern of the sample formed at a value of x of 0.1, however, peaks appeared that were not

#

those of Laves phases and no crystal of $MgNi_2$-type was found (Fig. 3.1b). In contrast, the pattern for the sample formed at a value of x of 0.6 exhibited two phases ($MgCu_2$ and $MgNi_2$ structure types), suggesting a successive structural transformation (Fig. 3.1d). Based on the structural relationships, $MgNi_2$-type phase was supposed to occur through the boundaries between the $MgZn_2$- and $MgCu_2$-type phases, as had been observed in many Laves systems. Therefore, our remaining discussion of the variation in the Laves phase structures of the $HfAl_{2-x}Cu_x$ systems focuses on the compositions $0.2 \leq x \leq 1$ and the sequence of types $MgCu_2$ → $MgNi_2$ → $MgZn_2$. The structural variation was accompanied by a decrease in the number of valence electrons as Cu atoms gradually replaced Al atoms. Such behavior is similar to that of the $CaAl_{2-x}Li_x$ system [74], in that aluminum atoms were replaced by lithium atoms and the phase varied in the sequence $MgCu_2$ → $MgNi_2$ → $MgZn_2$ from the electron-rich side to the electron-poor side.

3.2 Crystal structure

We obtained crystals from three of the nominal $HfAl_{2-x}Cu_x$ products—those with values of x of 0.5, 0.9, and 1.0; their refined compositions, $HfAl_{1.51}Cu_{0.49}$, $HfAl_{1.12}Cu_{0.88}$, and $HfAl_{0.96}Cu_{1.04}$, respectively, were very close to the stoichiometric ratios. Table 2.1 provides detailed information regarding these crystals; Table 2.2 lists the atomic coordinates and isotropic thermal parameters of the three phases. Table 2.3 presents selected interatomic distances. Fig. 3.2 displays the Laves structures in our systems in forms of constructive slabs, where red and blue spheres represent Hf

and Al/Cu atoms, respectively. Slabs A and B possess inverse configurations (Fig. 3.2a), dimensioned by blue spheres with red spheres located at (3/8, 3/8, ±3/8) of the unit, with part of a Kagomé net in the form of a triangular plane parallel to the plane *ab*; slab C can be regarded as a combination of the former two slabs. The $MgZn_2$, $MgNi_2$ and $MgCu_2$ structure types were formed by the stacking of these slabs in the sequences A-B, A-C-A-B, and A-C-B, respectively, with further shifted parts of the blue spheres to form vertex-sharing tetrahedra with a Kagomé net within the slabs (Fig. 3.2b).

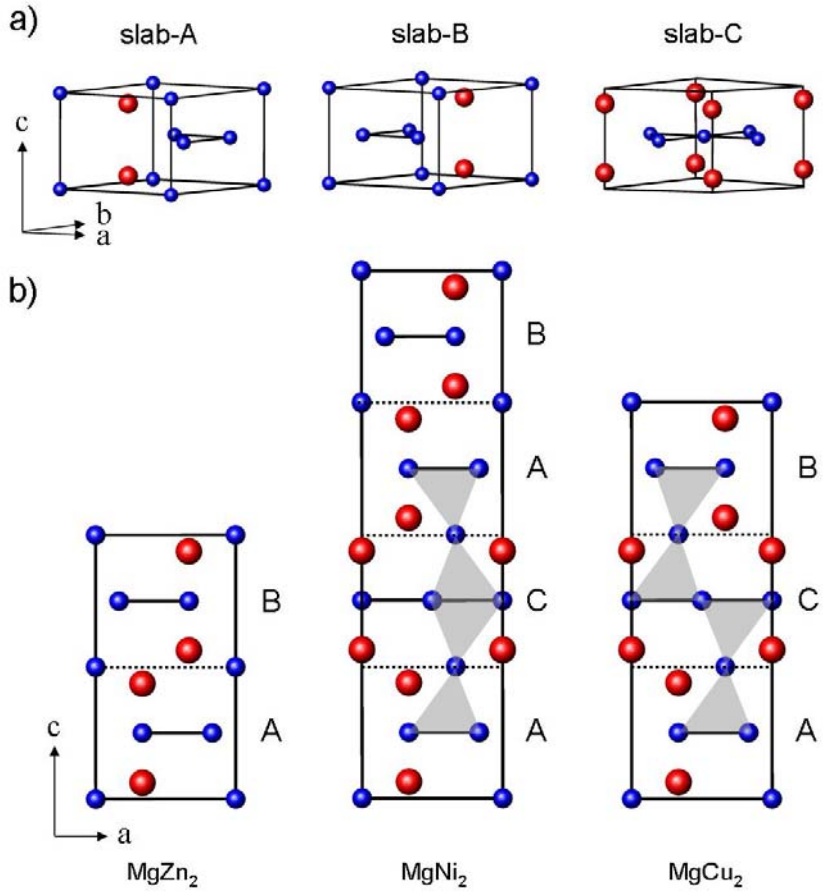

Fig. 3.2 (a) Constructive units of Laves structures. (b) Stacking structures of the $MgZn_2$, $MgNi_2$, and $MgCu_2$ types in projections along the crystallographic b-axis [010].

#

$HfAl_{1.51}Cu_{0.49}$ crystallized in cubic structure of space group $Fd\bar{3}m$ with constant M-M bond length of 2.60 Å. Comparing to $HfAl_{1.65}Cu_{0.35}$, the bond lengths were nearly identical in spite of difference in metallic radii (r_{Al} = 1.25 Å; r_{Cu} = 1.18 Å) [147]. Nevertheless, the size effect still observed in varying bonds of $MgNi_2$ and $MgZn_2$ structure comprised by more Cu atoms. $HfAl_{1.12}Cu_{0.88}$ and $HfAl_{0.96}Cu_{1.04}$ crystallized in hexagonal $MgNi_2$ and $MgZn_2$ structural types (space group $P6_3/mmc$), respectively. The Kagomé net exhibited flexibility in the $HfAl_{1.12}Cu_{0.88}$ structure with the $MgNi_2$ form and $HfAl_{0.96}Cu_{1.04}$ with $MgZn_2$ form (Fig. 3.3). In $HfAl_{1.12}Cu_{0.88}$, two types of Kagomé nets were constructed by M2(6*h*) and M3(6*g*) sites: the M2-based net exhibited considerably larger (2.65 Å) and shorter (2.51 Å) bond distances, whereas the M3-based net contained identical M-M bond lengths (2.58 Å). The distortion was also observed in the $HfAl_{0.96}Cu_{1.04}$ structure, which featured distances of 2.64 Å and 2.52 Å between adjacent M atoms. According to the site occupancy in Table 2.2, the Cu atoms preferred to reside in positions of the Kagomé net, indicating that the heteroatomic interactions had a greater correlation with the variation of bond length; this preference is consistent with the trend revealed in the simulated models (see below).

#

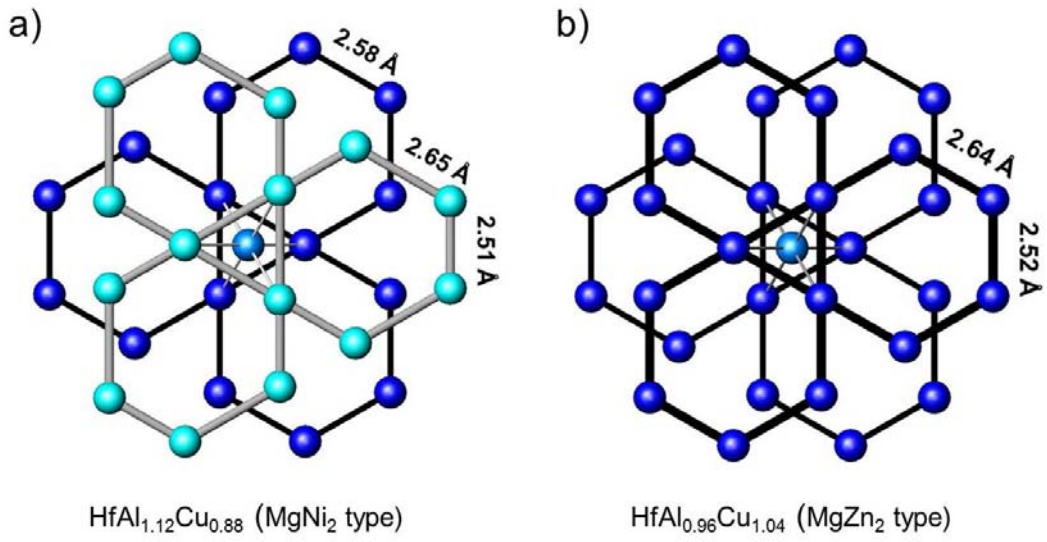

Fig. 3.3 Distorted Kagomé nets of the (a) $HfAl_{1.12}Cu_{0.88}$ and (b) $HfAl_{0.96}Cu_{1.04}$ systems. The M(1), M(2), and M(3) atoms of $HfAl_{1.12}Cu_{0.88}$ are presented as cyan, light-blue, and blue spheres, respectively. Cyan and Blue spheres denote M(1) and M(2) atoms in $HfAl_{1.51}Cu_{0.49}$, respectively. The Hf atoms have been removed for clarity.

Fig. 3.4 displays the refined lattice parameters and cell volumes of the $HfAl_{2-x}Cu_x$ species within the homogeneity ranges (x = 0.2–0.5 and 0.7–0.9), determined using the CELREF program[148]. To better compare the variation between phases, the lattice parameters of $MgCu_2$-type samples refined with $Fd\bar{3}m$ symmetry were previously converted to hexagonal form, i.e. $a_h = \sqrt{2}\, a_c$, and $c_h = \sqrt{3}\, c_c$; then, the length of the c-axis of each sample was divided by number of layers comprising the structure [$h = 1/2c_{(MgZn2)} = 1/3c_{h(MgCu2)} = 1/4c_{(MgNi2)}$]. According to the refined powder XRD results and crystal data, increased Cu contents correlates satisfactorily with the contractions of the volume and the lattice parameters, owing to the difference in metallic radii. The

variation of the *a*- and *c*-axes is specified by the *h*/*a* ratio—0.816 for $MgCu_2$ phases, 0.812 for $MgNi_2$ phases and 0.807 for $MgZn_2$ phase (values obtained from crystal data) — which are indicative of obvious structural transformation.

.

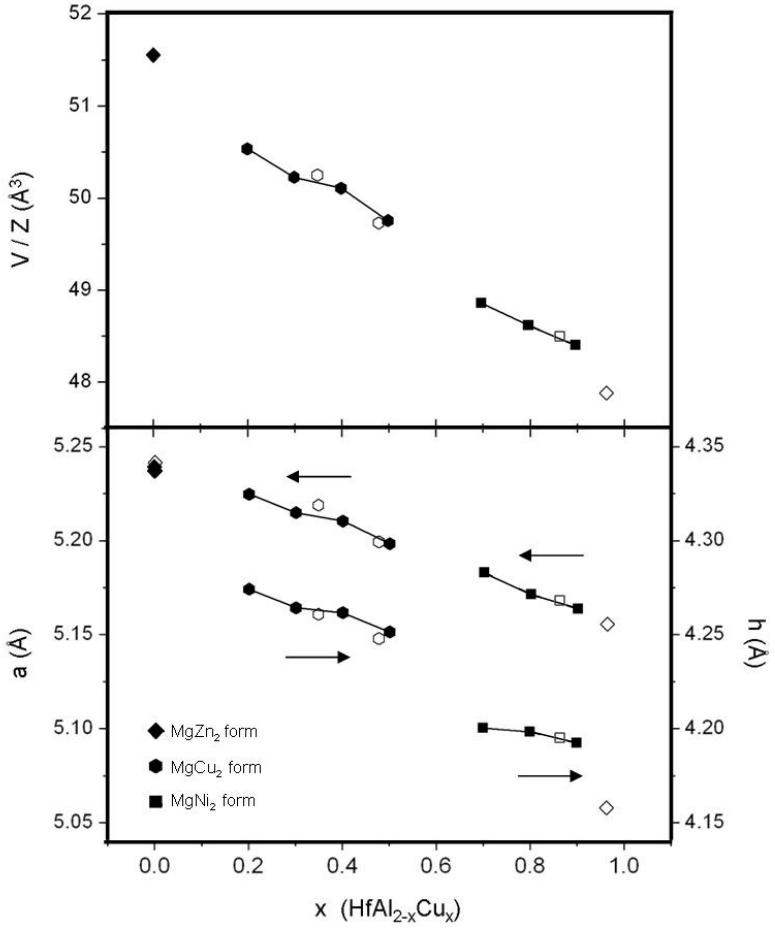

Fig. 3.4 Refined volumes and cell parameters $HfAl_{2-x}Cu_x$ within the homogeneity ranges (x = 0.2–0.5 and 0.7–0.9), and for a value of x of 0 for comparison. Crystal data for values of x of 0, 0.35, 0.49, 0.88, and 1.04 are plotted as open symbols. $h = 1/2c_{(MgZn2)} = 1/3c_{h(MgCu2)} = 1/4c_{(MgNi2)}$.

#

3.3 Physical properties

Fig. 3.5 presents the resistances of the $HfAl_{2-x}Cu_x$ systems (x = 0.5, 0.7, 0.9). The resistivities at 300 K were 4.35, 5.85 and 6.50 mΩ·cm, respectively, and they decreased slowly upon decreasing the temperature, consistent with the properties of a conducting metal. These resistivities are much higher than that of a typical conductor, most likely because of the effect of grain boundaries.

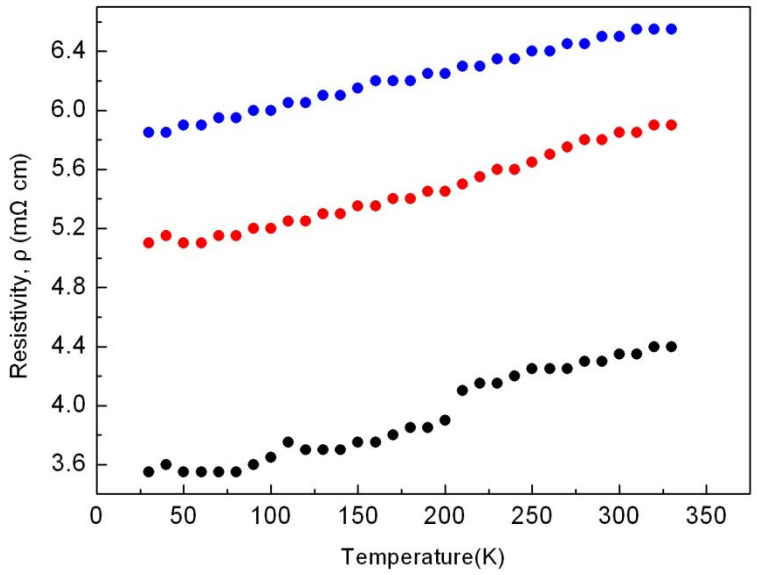

Fig. 3.5 Temperature dependence of the resistances of $HfAl_{2-x}Cu_x$ species (x = 0.5, 0.7 and 0.9), which are presented as black, red and blue dots, respectively.

3.4 Calculations of electronic structure

Our structural analyses indicated that Cu and Al atoms were mixed-occupied at the same metal sites. To simulate the observed compositions, we constructed models for all of the structures with the

#

space group *P*1. For the structural models $HfAl_{1.5}Cu_{0.5}$ (type $MgCu_2$), $HfAl_{1.25}Cu_{0.75}$ (type $MgNi_2$), and HfAlCu (type $MgZn_2$), the atomic sites for the Al and Cu atoms were split to 16, 16 and 8 positions, respectively, establishing 14, 127 and 18 possible atomic arrangements of Al and Cu atoms, respectively. We employed these models in calculations using the LMTO method. The model with the lowest total energy was assigned as the optimal distribution of Al and Cu atoms for these structures [30]. The correlation between the total energy and the coloring scheme is listed in Table 2.2. For models with lower total energies, the Cu atoms tended to organize in chains or alternately bonded with Al atoms; in contrast, for models with higher total energies, the Cu atoms grouped into tetrahedral or poly-cluster forms (Fig. 3.6). The arrangement of Cu and Al atoms was related to the number of bonding interactions. Table 2.2 revealed that the model with the lowest total energy in each phase contained the largest number of Al–Cu bonds. This result is similar to that from a study of $EuAg_xAl_{11-x}$ system [149], with nearly identical intrinsic characteristics for the Al–Cu and Al–Ag bonds; this system was also more stable when the heteroatomic contact increased. The lower-energy models mostly featured Cu atoms located in positions of the Kagomé net, correlating with the increased Cu occupancy in these positions revealed in the three observed crystals. Furthermore, the compositions of Cu atoms and Al atoms, according to the crystal refinements, were statistically close inside the Kagomé net for the $MgNi_2$-type and $MgZn_2$-type compounds, suggesting these atoms may be alternately connected as the optimum coloring arrangement.

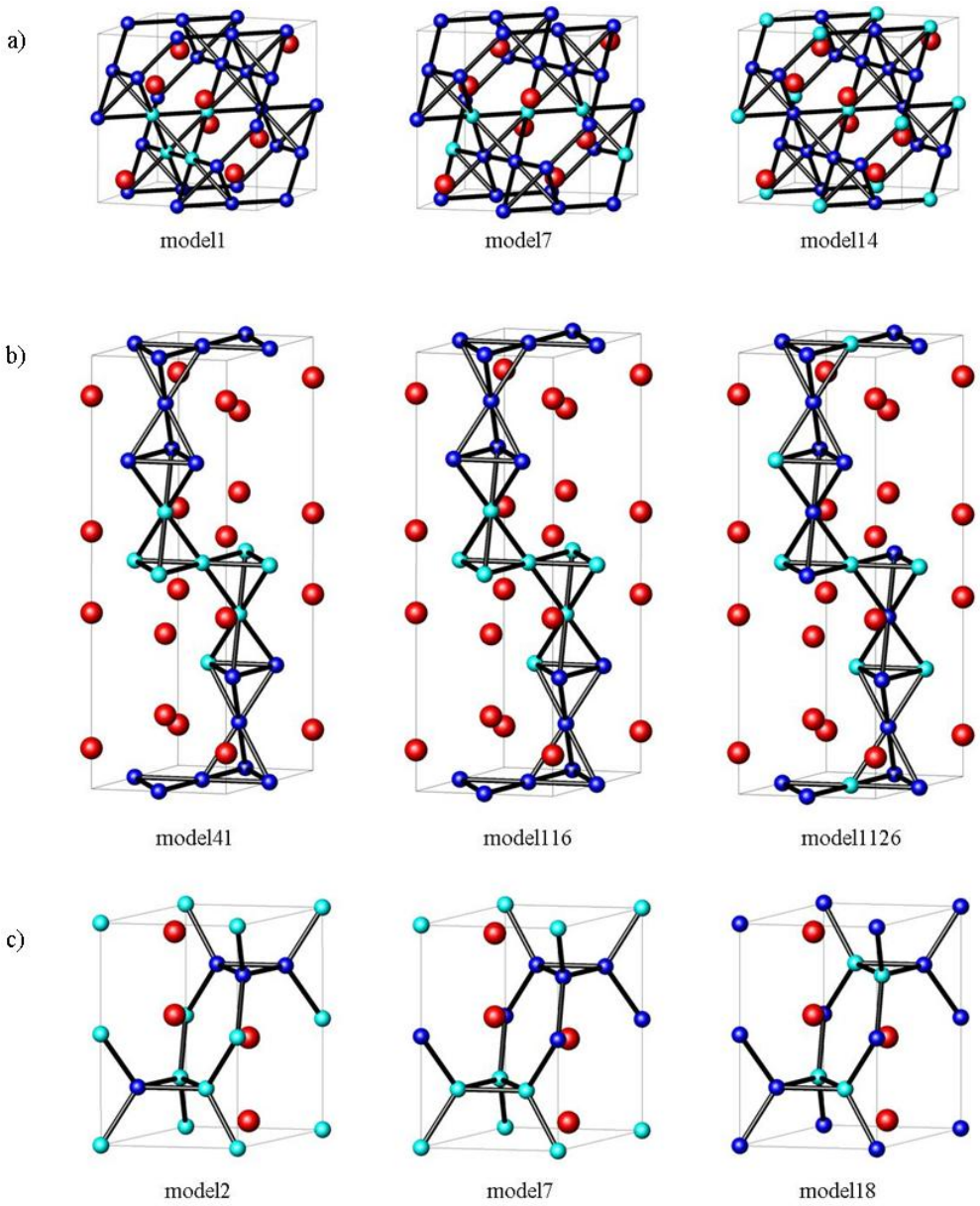

Fig. 3.6 Arrangements of Cu and Al atoms with space group P1 in various coloring models. (a) $HfAl_{1.5}Cu_{0.5}$, $MgCu_2$-phase. (b) $HfAl_{1.25}Cu_{0.75}$, $MgNi_2$-phase. (c) HfAlCu, $MgZn_2$-phase. Red spheres denote Hf atoms, blue spheres denote Al atoms and cyan spheres denote Cu atoms.

#

Table 3.2 Differences of Total Energy and Number of Metal Bonds with various Coloring Models

composition	structural type	model	dE_{tot} /eV	Cu–Cu	Al–Al	Al–Cu
$HfAl_{1.5}Cu_{0.5}$	$MgCu_2$	1	0.012	6	32	10
		7	0.006	4	24	20
		14	0	0	24	24
$HfAl_{1.25}Cu_{0.75}$	$MgNi_2$	41	0.014	14	24	10
		116	0.0049	6	20	22
		126	0	4	16	28
HfAlCu	$MgZn_2$	7	0.009	9	9	6
		2	0.0026	6	6	12
		18	0	4	4	16

Fig. 3.7 displays the DOS and COHP plots obtained from models of $HfAl_{1.5}Cu_{0.5}$, $HfAl_{1.25}Cu_{0.75}$ and HfAlCu with the lowest total energy. The calculated band structures suggested metallic properties for these compounds. The contributions of electronic states just below and above the Fermi level (EF) arose mainly from the 4d orbitals of the Hf atoms, with small contributions from that of Al 3s/3p and Cu 4s/3d orbitals. The large states in Fig. 3.7a, between -4 to -3 eV, were dominated by the 3d orbitals of Cu atoms. Upon increasing the composition of Cu atoms, the Cu d states were much broader and contributed to greater extents at energies of approximately –2 eV (Fig. 3.7 b, c), owing to increased Al–Cu interatomic interactions. The COHP curves reveal that, in the models of $MgCu_2$ and $MgNi_2$ types, the Al–Al, Al–Cu and Cu–Cu states were relatively weak and the Hf–Al and Hf–Cu states were essentially nonbonding within the region between the pseudogap and the Fermi level, consistent with the experimentally observed phase width. Each calculation in the models of $MgNi_2$ and $MgZn_2$ types revealed the –ICOHP value of Al–Cu bond (1.06 on average)

was much greater than that of Cu–Cu bond (0.71 on average). The strong heteroatomic interaction is supposed to drive the Cu atoms to form Al–Cu bonds in the coloring models, and thus stabilized the system by maximizing numbers of Al–Cu contacts. In other words, once the number of Cu atom is greater than Al atom, the weaker Cu–Cu bond become the majority inside the structure, and the phase stability decrease relatively, which was in accordance with the experimental result of reaction $HfAl_{2-x}Cu_x$ while x was larger than one.

#

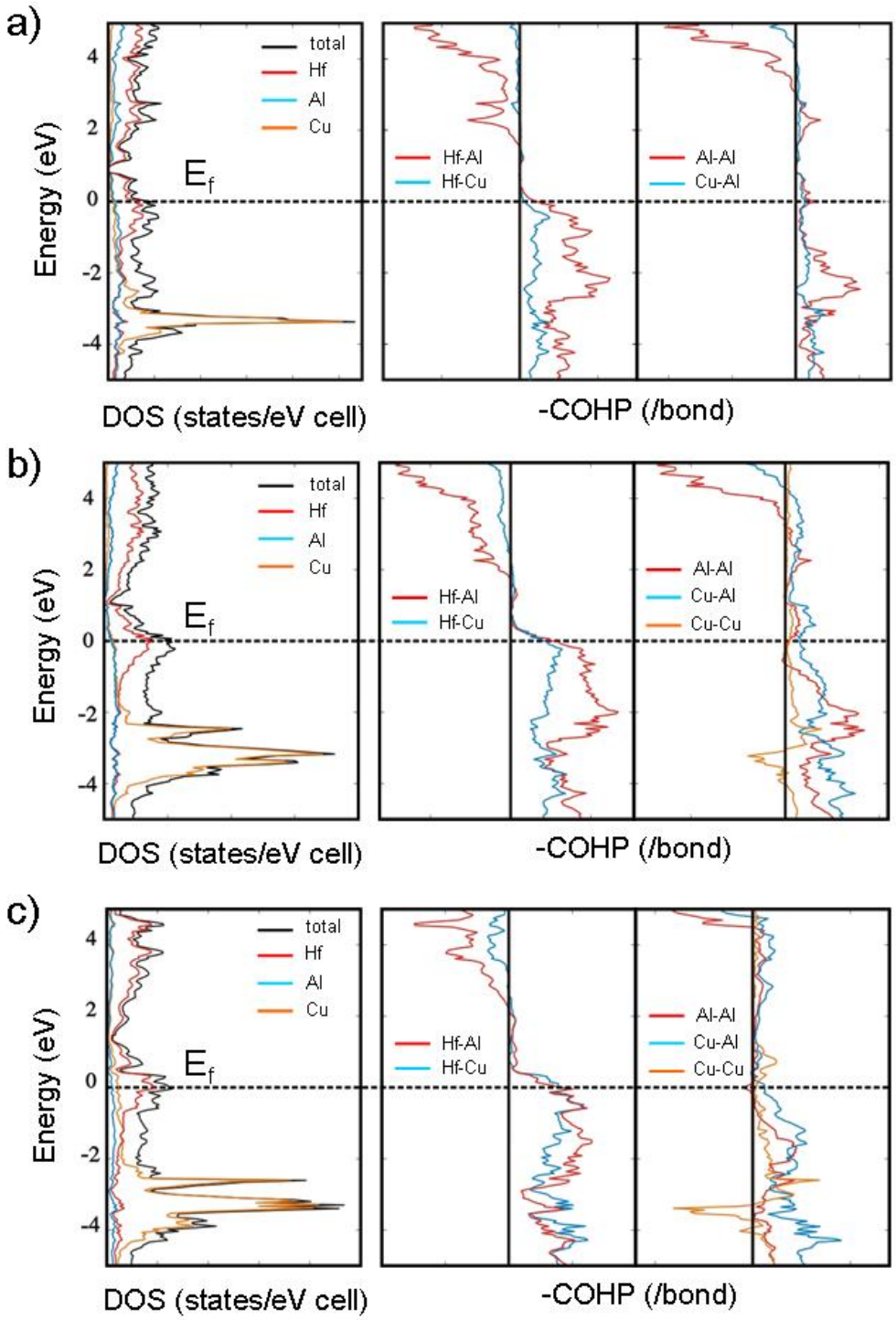

Fig. 3.7 Calculated DOS and COHP curves for (a) $MgCu_2$–type $HfAl_{1.5}Cu_{0.5}$, (b) $MgNi_2$–type $HfAl_{1.25}Cu_{0.75}$, and (c) $MgZn_2$–type HfAlCu models.

#

Chapter 4

Synthesis, Structure and Bonding of New Ternary Aluminide $Hf_6Cu_{16}Al_{7.58}$

Results and Discussion

4.1 Synthesis

According to the PXRD pattern, the title compound was discovered in work on the Laves phase, and recognized as structural type Th_6Mn_{23} [84] . Similar patterns appeared in samples from an arc-melting reaction that yielded $HfCu_{4-x}Al_x$ with x = 0.5 – 1.5, but the product contained numerous phases, making difficulty in selecting single crystals. The pure phase was then obtained from a reaction $HfCu_3Al$, which was performed within an environment of an alumina crucible (Fig. 4.1). Structural analysis of a single crystal revealed a compound isostructural with the $Sc_{11}Ir_4$ type with refined composition $Hf_6Cu_{16}Al_{7.58}$. We attempted to replicate the compound with an arc-melting reaction in a stoichiometric ratio, but $HfCu_2Al$ [150] occurred as byproduct with minor phase of structure type $MgZn_2$ [94] . It is attributed to the closely related structures and compositions between $Hf_6Cu_{16}Al_{7.58}$ and $HfCu_2Al$ as described below.

#

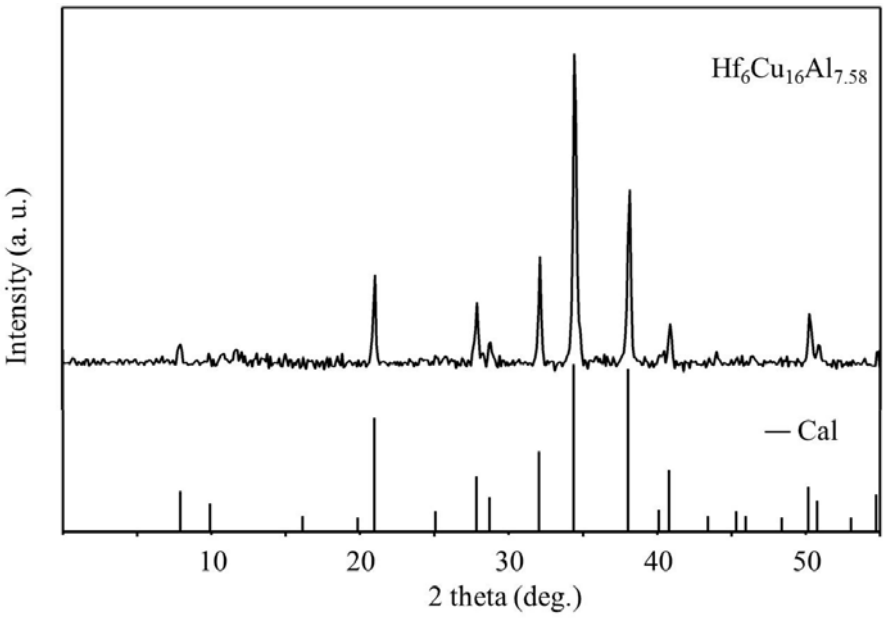

Fig. 4.1 Calculated and experimental X-ray powder patterns for $Hf_6Cu_{16}Al_{7.58}$.

4.2 Crystal Structure

$Hf_6Cu_{16}Al_{7.58}$ crystallized in cubic structure of space group $Fm\bar{3}m$ that structurally resembles compound $HfCu_2Al$. Figure 4.2 displays the structure of $HfCu_2Al$ and one eighth of the unit cell of $Hf_6Cu_{16}Al_{7.58}$. In $HfCu_2Al$, Hf and Al atoms are arranged as NaCl structure with encapsulated Cu atoms in eight tetrahedral sites, generating a composition $Hf_4Cu_8Al_4$ in a unit cell. For $Hf_6Cu_{16}Al_{7.58}$, Al atoms retained the same cubic positions, whereas Hf atoms and Cu atoms shifted from the octahedral sites and tetrahedral sites, respectively; the central Hf atom was excluded, yielding composition $Hf_3Cu_8Al_4$ for structure type $Sc_{11}Ir_9$.

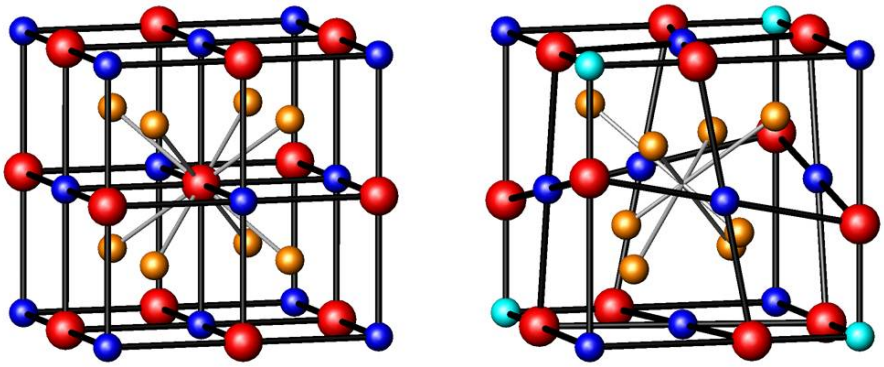

$HfCu_2Al$ $(1/8)\ Hf_6Cu_{16}Al_{7.58}$

Fig. 4.2 Structures of $HfCu_2Al$ and one eighth of $Hf_6Cu_{16}Al_{7.58}$. The red, yellow, and blue spheres represent Hf, Cu and Al atoms, respectively. The cyan sphere is the partial occupied Al2 atom.

Fig. 4.3a displays the structure of $Hf_6Cu_{16}Al_{7.58}$ in shells of polyhedral; its structure is regarded as a condensation of polyhedra in four successive shells: the first shell is an octahedron of six Hf atoms centered at atom Al2 in site 4b; the second is a cube composed of eight Cu2 atoms; the third is a cuboctahedron of twelve Al3 atoms, and the fourth shell contains 24 Cu1 atoms forming a rhombicuboctahedron. These polyhedral shells stack in cubic close packing, which formed cubic vacancies for Al1 atoms, as shown in Fig 4.3b.

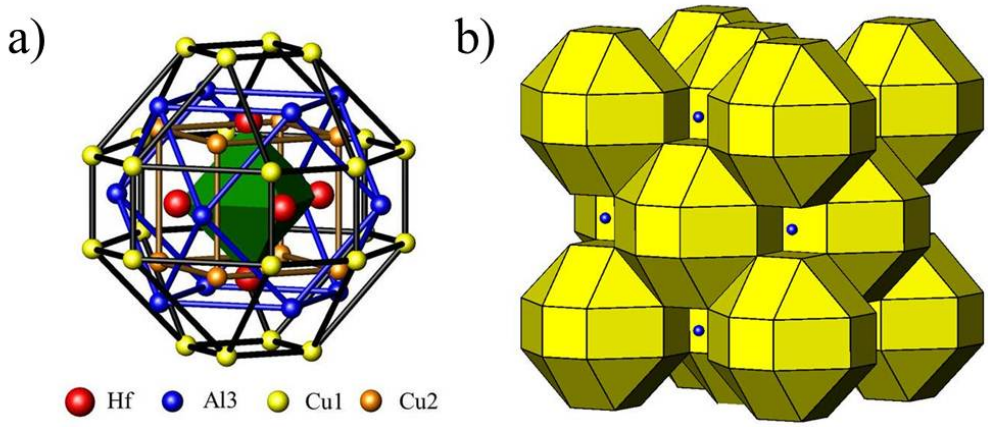

Fig. 4.3 (a) Structure of $Hf_6Cu_{16}Al_{7.58}$ in form of polyhedral shells. (b) Building units of polyhedral shells condenses in cubic closed packing.

Fig. 4.4 displays the local environment of each crystallographic site, which are classified as a capped trapezoid prism (Hf1, CN9), icosahedron (Cu2, CN12) and one with an additional vertex (Cu1, CN13), cube (Al1, CN8), octahedral (Al2, CN6), and bi-capped trigonal antiprism (Al3, CN8). To present reasonable bonds, the distances from the central atom are truncated at 3 Å according to the metallic radii (r_{Hf} = 1.44 Å; r_{Cu} = 1.18 Å; r_{Al} = 1.25 Å) [147] . The Hf atom to the adjacent Cu atoms are within 2.88 - 2.94 Å. These connections are longer than the sum of the corresponding metallic radii and that observed in $HfCu_2Al$ (2.67 Å), and are considered as weak binding. Both Cu1 and Cu2 atoms are located in high coordination environments in the structure. The Cu–(Cu, Al) bond lengths are in a reasonable range 2.43 - 2.83 Å, near those found in CuAl ($d_{Cu–Cu}$ = 2.65 Å) [151], and Cu_2Al_3 ($d_{Cu–Cu}$ = 2.82 Å, $d_{Cu–Al}$ = 2.49–2.59 Å) [152]. The Al2 atom partially occupied the regular octahedron with a small bond distance (2.37 Å) to the vertices; its

displacement parameter was larger than other positions, which might reflect a spatial consideration. Calculations of electronic structure revealed a strong interaction in Hf-Al bonding (see below) that stabilized atomic connections of this type.

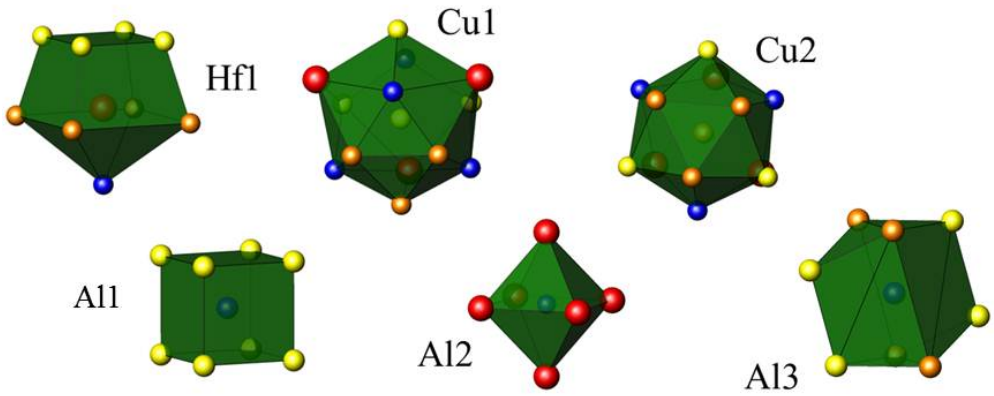

Fig. 4.4 Local environments of Hf, Cu and Al atoms with truncation distances of 3 Å.

Measurements of resistivity of $Hf_6Cu_{16}Al_{7.58}$ are plotted as a function of temperature in Fig. 4.5. At 323 K the resistivity is 0.18 mΩ cm; this value increases with increasing temperature, indicative of a metallic property. The resistivity does not exhibit a linear dependence with temperature; a minor mixture of the $HfCu_2Al$ phase and a small effect of grain boundaries might cause this effect.

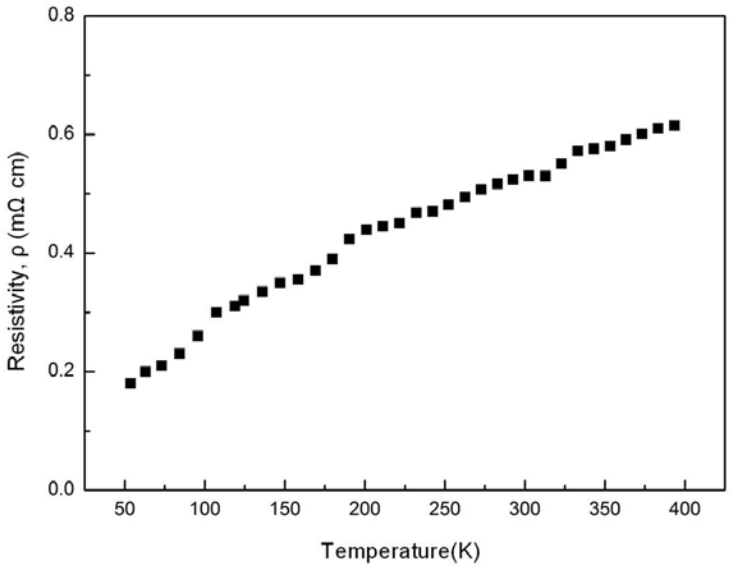

Fig. 4.5 Temperature dependence of the resistances of $Hf_6Cu_{16}Al_{7.58}$ species.

4.3 Calculations of Electronic Structure

Fig. 4.6 presents calculated plots of the densities of states (DOS) and crystal-orbital Hamilton population (COHP) for a detailed investigation of the electronic structure and bonding properties. Calculated model '$Hf_6Cu_{16}Al_8$' was established using crystal data of $Hf_6Cu_{16}Al_{7.58}$ with the Al2 position designed to be fully occupied. There is no observable band gap about the Fermi level, indicating the compound to be metallic. A maximum occurs between ca. -4 and -2 eV, which pertains mainly to 3d orbitals of copper. The contributions of electronic states about the Fermi level were mainly from 4d orbitals of Hf atoms, 3p orbitals of Al atoms and 4s orbitals of Cu atom, indicating regular interactions between these atoms. Individual and total –ICOHP values for

bonding interactions are listed in Table 4. Consistent with the result of the bond distance, the calculation reveals a weak interaction in the Hf–Cu bond with –ICOHP = 0.43, smaller than that for a homoatomic Cu–Cu bond, 0.61. The Cu–Al interaction was strong (0.99) with a large bonding contribution per cell, marking the dominance of the Cu–Al bond in the contribution to structural bonding (53.40 %). The COHP curves reveal a strong Hf–Al interaction (–ICOHP value: 1.21) with a sharp maximum near the Fermi level. The corresponding electronic structure of hypothetical model '$Hf_6Cu_{16}Al_7$' (with an empty 4b site) is marked with a dot line in the figure, indicating that the strength of the Hf–Al bond was determined by the composition of the Al atom in the 4*b* site. As a result, the partial occupancy of Al2 atom is not only attributed to an unfavorable coordination environment, but also in seeking an optimal bonding strength of the Hf–Al interaction.

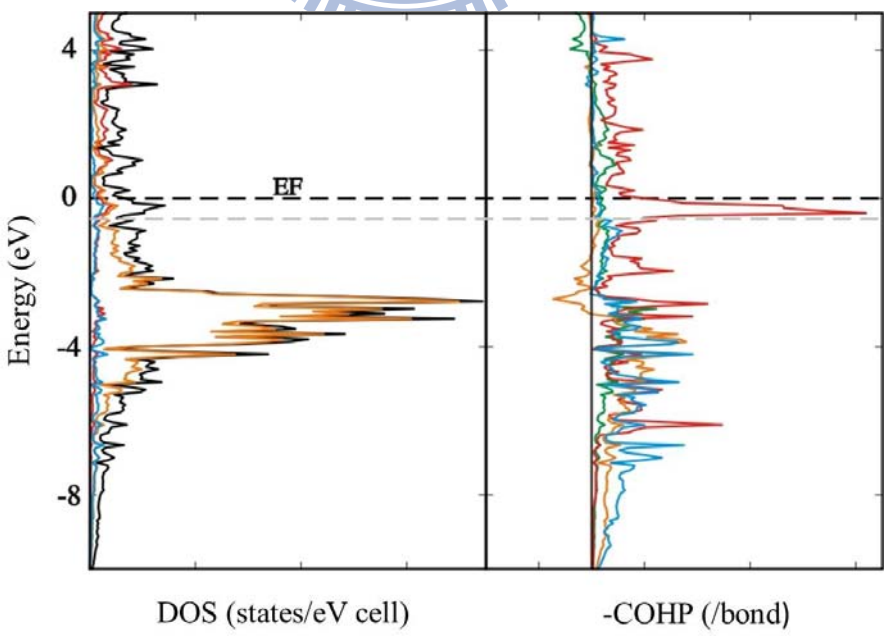

Fig. 4.6 Calculated densities of states (DOS) and crystal-orbital Hamiltonian-population (COHP) curves for theoretical model $Hf_6Cu_{16}Al_8$.

Table 4.1 Individual and total -ICOHP values for bonding interactions for $Hf_6Cu_{16}Al_{7.58}$

bond	Hf-Cu	Hf-Al	Cu-Cu	Cu-Al
number of bonds/cell	64	48	48	128
-ICOHP/bond (avg.)	0.43	1.12	0.61	0.99
-COHP/cell	27.52	53.76	29.28	126.72
contribution /%	11.60	22.66	12.34	53.40

Chapter 5

Synthesis and Characterization of $Hf_5Al_{3-x}Sb_x$ (x = 0.70, 1.44, 2.14)

Results and Discussion

5.1 Synthesis

The title compounds were obtained from reactions with general formula "$Hf_5Al_{3-x}Sb_x$", in which x was varied from 0 to 3 in step 0.5. It performed a survey of ternary phase through the concentration line between two binary compounds Hf_5Al_3 [153] and Hf_5Sb_3 [154] . To the best of our knowledge, these new compounds were the first examples of ternary phase in the Hf-Al-Sb system. In attempts to find new ternary phases, similar trials, such as reactions $HfAl_{1-x}Sb_x$ and $HfAl_{2-x}Sb_x$, were not successful. According to the powder XRD measurements (Fig. 5.1), the product of $Hf_5Al_{3-x}Sb_x$ remained within the Mn_5Si_3 type in the range $0 < x < 1.0$. The signals shifted to smaller 2 theta angle, indicating an extension of the cell volume, as Sb atoms gradually replaced Al atoms. The pattern exhibited a two-phase feature (Mn_5Si_3 and W_5Si_3 structural types) when $x = 1.5$, and showed single-phase product of W_5Si_3 type within the range $2 < x < 2.5$. Finally, the pattern for Hf_5Sb_3 ($x = 3$) revealed air-sensitive product of Y_5Bi_3 structural type.

#

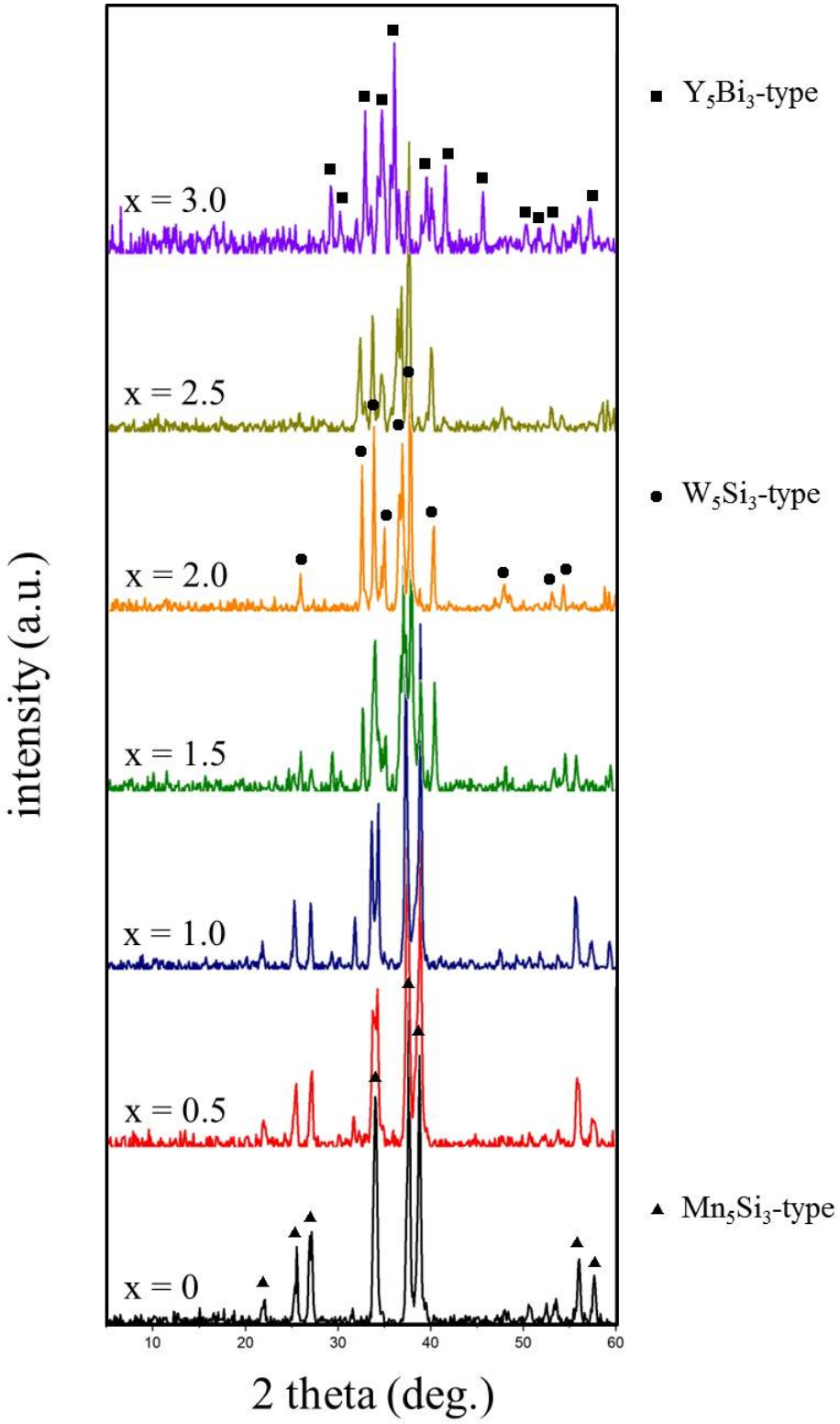

Fig. 5.1 Experimental X-ray powder patterns for $Hf_5Al_{3-x}Sb_x$.

5.2 Crystal structure

$Hf_5Al_{2.30}Sb_{0.70}$ crystallized in hexagonal space group *P6₃/mcm* with structure of Mn_5Si_3-type as shown in Fig. 5.2. It implied a condensation of two distinct octahedra which condensed by sharing basal faces along the [001] direction. One of octahedral was centered by Hf1 atom, which was surrounded by six M(Al/Sb) atoms with a distorted form (Fig. 5.2b) on the threefold axes; the other was established by six Hf2 atoms with regular coordination around the origin of unit cell (Fig. 5.2c). Relative to the isostructural compound Hf_5Al_3, Sb substitution caused an increase of the unit cell volume of the ternaries. The *a* axis of $HfAl_{2.30}Sb_{0.70}$ increased from 8.07 Å to 8.14 Å for Sb substitution ~23 %; the M-M distances expanded from 3.19 Å to 3.32 Å. The Hf1-M bonds were consistent at distance 2.88 Å, and those for Hf2-M varied from 2.89 Å to 3.09 Å. The Hf1 atoms were separated vertically with distance 2.83 Å, indicative of Hf-Hf interaction for it was significantly smaller than that in structure of Hf metal (3.13 Å).

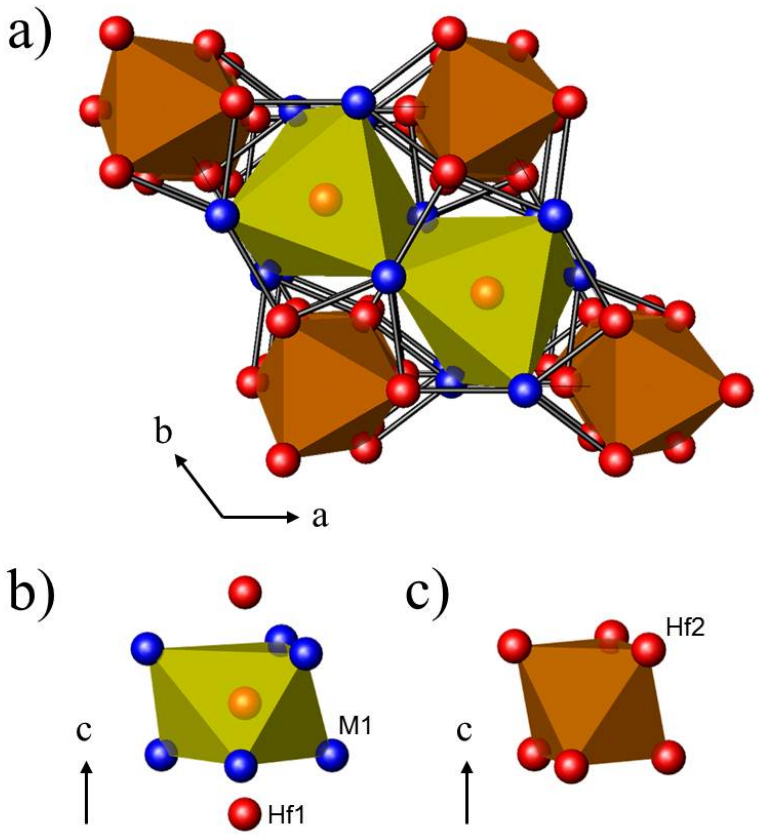

Fig. 5.2 (a) Structure of $HfAl_{2.30}Sb_{0.70}$ in a projection along the c-axis. (b) Hf1-centered trigonal antiprism composed by mixtures of metals (Al/Sb) with vertical Hf-Hf bond. (c) Trigonal antiprism composed by Hf2 atoms.

Fig. 5.3 displayed W_5Si_3 structure adopted by $Hf_5Al_{1.56}Sb_{1.44}$ and $Hf_5Al_{0.86}Sb_{2.14}$, which contains four crystallographically unique positions for two Hf atoms (4*b* and 16*k*) and two mixtures of Al and Sb atoms (4*a* and 8*h*). It consisted of polyhedra of two types, which were a M2-based tetrahedron and a Hf2-based square antiprism, stacking along the *c* direction through edge-sharing and face-sharing, respectively. The Hf1 atom was distant from the M2 sites by 2.88 Å in $Hf_5Al_{1.56}Sb_{1.44}$, which was near that of 2.89 Å in $Hf_5Al_{0.86}Sb_{2.14}$. The Hf2-M bonds were nearly

identical in these two compounds within the range 2.87 – 2.92 Å. Similar to the $Hf_5Al_{2.30}Sb_{0.70}$ (Mn_5Si_3 structure type), the Hf1 atoms and M1(Al/Sb) atoms were adjacent to themselves vertically with half-length 2.76 Å of the *c*-axis. This distance was smaller than the bond length within the elements aluminium (2.86 Å), antimony (2.90 Å) and hafnium (3.13 Å).

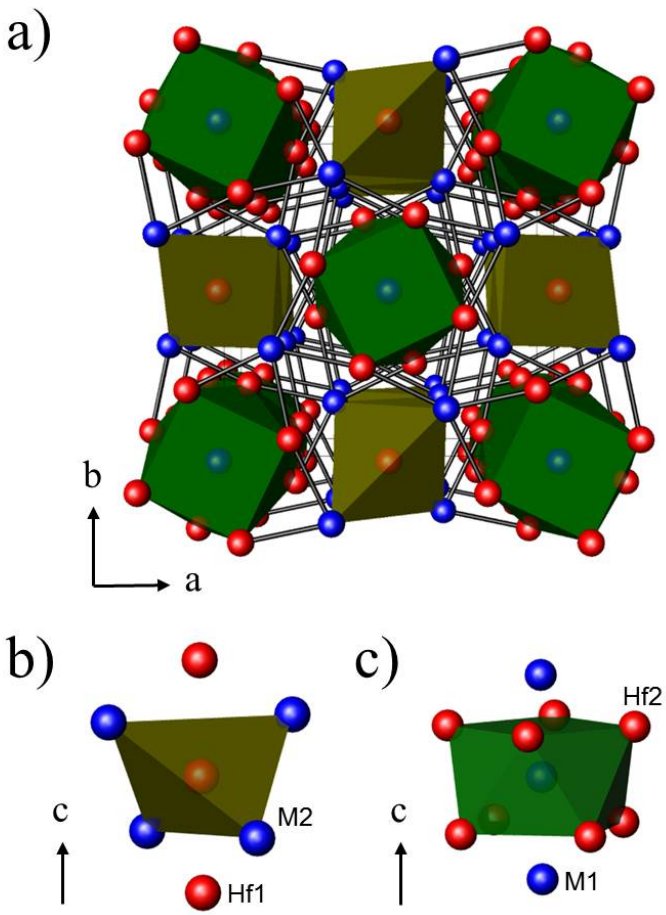

Fig. 5.3 (a) Structure of $HfAl_{1.56}Sb_{1.44}$ and $HfAl_{0.86}Sb_{2.14}$ in a projection along the c-axis. (b) Tetrahedron composed by mixtures of metals (Al/Sb) with vertical Hf-Hf bond. (c) Square antiprism composed by Hf2 atoms with vertical M-M bond.

#

Based on the crystallographic data, the smaller Al atoms preferred to locate in the 4*a* site with coordinated environment CN:10, whereas the larger Sb atoms mostly situated in the 8*h* site with fewer neighbor atoms, CN: 6. This behavior was also observed in many intermetallics, in which the 4*a* site was occupied by the smaller transitional-metal atoms [108, 109] . Brewer-Engel rules interpret the conflict of the size factor, such that the cohesive energy was supposed to be the result of d-electron interactions, which leads to maximal number of bonding between early and late transition-metal atoms [155] . The short bonds to adjacent atoms in the vertical direction are unfavorable for the larger atoms. We verified the result that Sb atoms were disadvantageous to place in the 4*a* site for the adverse bonding characters of a Sb-Sb interaction, relative to Al-Al and Al-Sb interactions, considering the phase-width behavior as specified in the theoretical calculation below.

Fig. 5.4 presented the resistivities of the pure samples of reaction $Hf_5Al_{3-x}Sb_x$, in which x = 0.5, 1.0 and 2.0. The resistivities 0.63, 0.78 and 0.90 mΩ·cm, respectively, at 323 K, gradually increased with temperature, indicating metallic properties as revealed in the calculations of electronic structure.

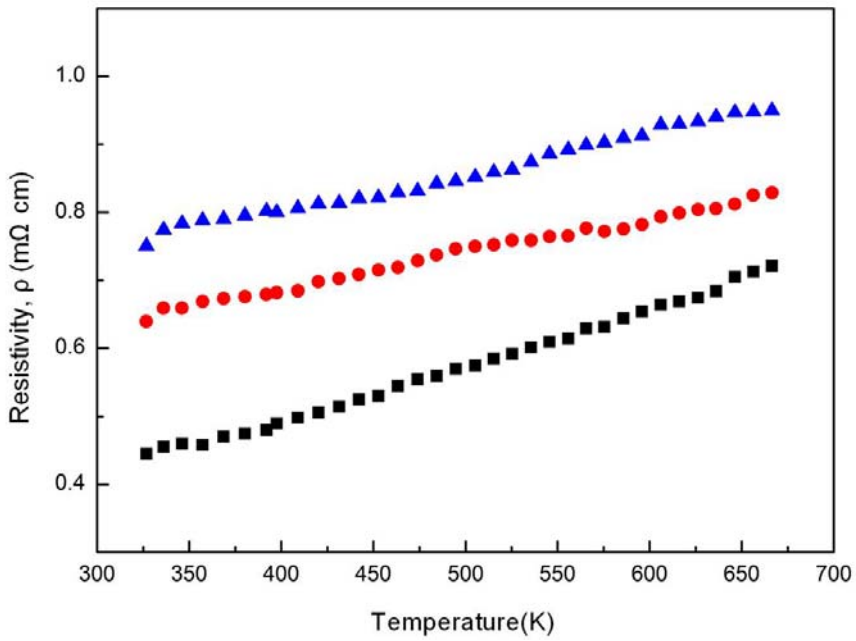

Fig. 5.4 Temperature dependence of the resistivities of $Hf_5Al_{3-x}Sb_x$ species (x = 0.5, 1.0 and 2.0), which are presented as blue (triangle), red (circle) and black (square) dots, respectively.

5.3 Calculations of electronic structure

To understand the electronic structure and bonding properties, we undertook quantum-chemical calculations with model '$Hf_5Al_{1.5}Sb_{1.5}$' of Mn_5Si_3 and W_5Si_3 types. These models were constructed by reducing the symmetry of Mn_5Si_3 and W_5Si_3 types to *P31m* and *P4*, respectively. The resulting models contained split metal sites from 6*g* of Mn_5Si_3 type and (4*a*, 8*h*) of W_5Si_3 type, which were assigned to match the designed formula to simulate the mixed Al/Sb site occupancies. Densities of states (DOS) and crystal-orbital Hamilton populations (COHP) calculated for model $Hf_5Al_{1.5}Sb_{1.5}$ of Mn_5Si_3 type were plotted in Fig. 5.5. The Fermi energy (EF) was located in a continuous band characterizing a metal property. The local minimum of the conduction band

composed mainly of the Hf d-orbitals with small contributions from Al 3s/3p and Sb 5p orbitals. The calculated band structure was similar to that of Hf_5Al_3 (not shown) except Sb orbitals narrowly lying below –10 eV, indicating Sb 5s states to be localized and considered as core orbitals.

The integrated COHP values of Hf-Hf, Hf-Al, and Hf-Sb were listed in Table 5.1. The average –ICOHP for Hf-Hf and Hf-Sb were similar at value 1.13, which is more substantial than Hf-Al (0.84). The overall –ICOHP contributions per cell in $Hf_5Al_{1.5}Sb_{1.5}$ were 50.1 % and 37.3 % from Hf-Sb and Hf-Al bonding, respectively, but 12.6 % for Hf-Hf, which indicated the Hf-M interactions to be mainly constructing the framework of the structure; the strong Hf-Sb bonding indicated that Sb replacements from Hf_5Al_3 would be stable within structure of Mn_5Si_3 type. Further substitutions of Al atoms from $Hf_5Al_{1.5}Sb_{1.5}$ were unfavorable for the bond strength of Hf-Sb contacts decreased as strongly affected by the anti-bonding.

Table 5.1 Individual and total -ICOHP values for bonding interactions for $Hf_5Al_{1.5}Sb_{1.5}$ model of Mn_5Si_3 type

bond	Hf-Hf	Hf-Al	Hf-Sb
number of bonds/cell	2	8	8
-ICOHP/bond (avg.)	1.14	0.84	1.13
-COHP/cell	2.28	6.72	9.04
contribution /%	12.6	37.3	50.1

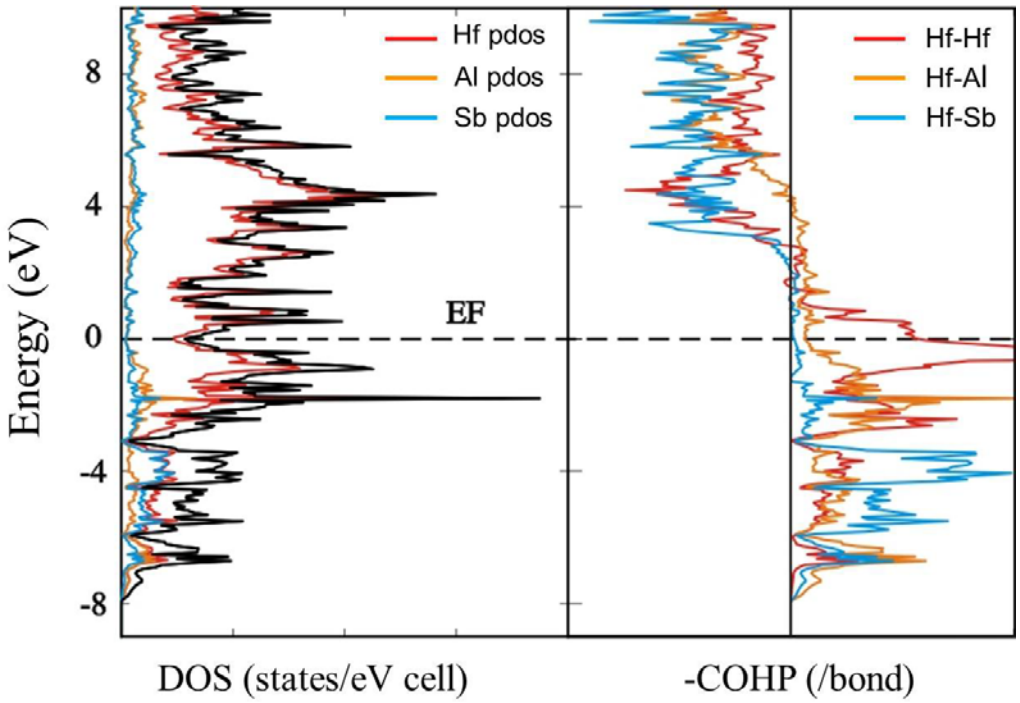

Fig. 5.5 Calculated densities of states (DOS) and crystal-orbital Hamiltonian-population (COHP) curves for theoretical model Hf5$Al_{1.5}Sb_{1.5}$ of Mn_5Si_3 type.

Fig. 5.6a displayed a DOS plot calculated for model $Hf_5Al_{1.5}Sb_{1.5}$ of W_5Si_3 type. The curves were expected to show a metallic property for the Fermi level located near the local energy minimum. The most prominent features in the DOS were the broad Hf 5*d* bands distributed above ~ –7.5 eV and the split Sb 5*s* bands from ~ –9 eV to ~ –12 eV. The partial DOS revealed that the Sb 5*s* states at the M2 site concentrated as core orbitals, whereas those at M1 site contributed to the Sb-Sb bond located at lower energy. To better compare the site preference in the square antiprism environment, Al and Sb atoms were assigned in two *P*4 symmetry models to establish Al-Al, Sb-Sb (model1) and Al-Sb bonds (model2). Individual and total –ICOHP values for bonding interactions

were listed in Table 5.2. In both models, the average –ICOHP for Hf-Hf (0.88) was smaller than that in the Mn_5Si_3-type model (1.14), likely because of the bond length decreased from 2.83 Å to 2.76 Å, and the Hf-Sb bonding was still substantial and contributed the greatest bond populations relative to other metal interactions. The Hf–Al and Hf-Sb bonds were essentially optimized at the Fermi level with largest –ICOHP values 0.98 and 1.27 eV/bond, which showed strong bonding interactions. Fig. 5.6c displayed bonding characteristics of Al-Al, Sb-Sb and Al-Sb bonds, which revealed essentially nonbonding near the Fermi level, indicating a result of the phase width as observed in experiments. Despite the COHP calculations indicating strong Sb-Sb interactions (–ICOHP values: Sb-Sb, 1.15; Al-Al, 1.00; Al-Sb, 1.07), the feature of Sb-Sb anti-bonding was more evident beyond the Fermi level compared to Al-Al and Al-Sb interactions, i.e. the Sb-Sb bond was unfavorable as the Sb composition increased or decreased in the corresponding phase. Considering the experimental observation to phase width, the W_5Si_3-type structure hence preferred Al atoms to occupy the 4*a* site to prevent the formation of linear Sb-Sb bonds, consistent with previous discussions about the preference of a smaller occupied atom [108, 109].

Table 5.2 Individual and total -ICOHP values for bonding interactions for $Hf_5Al_{1.5}Sb_{1.5}$ model of W_5Si_3 type

	model1					model2
bond	Hf-Hf	Hf-Al	Hf-Sb	Al-Al	Sb-Sb	Al-Sb
number of bonds/cell	2	10	10	2	2	4
-ICOHP/bond (avg.)	0.88	0.98	1.27	1.00	1.15	1.07
-COHP/cell	1.76	9.80	12.70	2	2.30	4.28

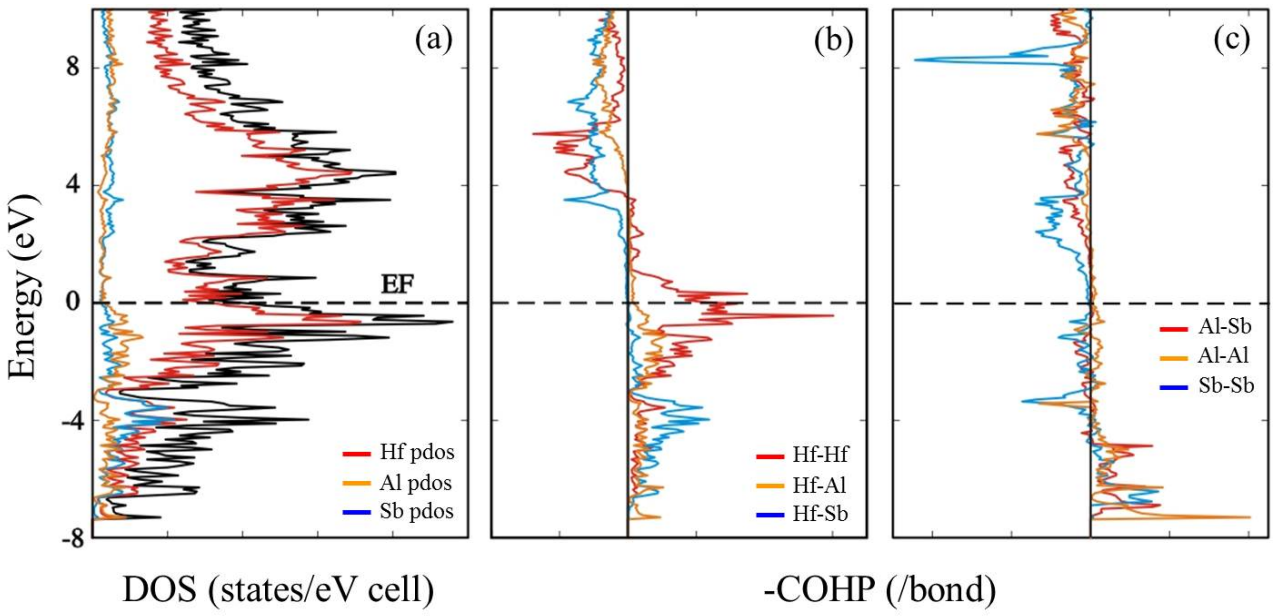

Fig. 5.6 Calculated densities of states (DOS) and crystal-orbital Hamiltonian-population (COHP) curves for theoretical model $Hf_5Al_{1.5}Sb_{1.5}$ of W_5Si_3 type.

#

Chapter 6

Ternary Intermetallics of $Hf_{13.0}Ni_{40.8}Ga_{30.9}$ and $Zr_{13.0}Ni_{40.6}Ga_{31.0}$

Results and Discussion

6.1 Synthesis

The Hf-Ni-Ga title compound was first found in a series of reactions $HfNi_{2.15+x}Ga_{3.85-x}$ (x = 0 to 2) in a trial seeking phase-width to the analogue of $YbCd_6$ [137]. Based on the powder XRD patterns, a new phase occurred when x was greater than 0.8. Further crystal analysis revealed that the new compound was isostructural to $Y_{13}Pd_{40}Sn_{31}$ [138] with the refined composition $Hf_{13.0}Ni_{40.8}Ga_{30.9}$. We performed phase-width experiments with reactions $Hf_{13}Ni_{30+x}Ga_{40-x}$, where x ranged from 0 to 20 in steps of 2. The targeted phase appeared, however, only within the range $8 < x < 12$; and the pure phase observed only when x was equal to 10. Refinements performed using the CELREF program [148] revealed that the lattice parameters of these samples were nearly identical, indicating the limited phase width of this structure. This result is consistent with the refinement of single crystals, which revealed that most sites were fully occupied by metals (see below).

According to the refined composition, we made attempts to substitute Hf atoms with elements of the same group, but only the Zr-analogue was replicated. This result can be rationalized by

considering the similar metallic radii of Hf and Zr atoms (r_{Hf} = 1.50 Å; r_{Zr} = 1.48 Å), and the relatively small Ti atom (r_{Ti} = 1.36 Å) [147]. Further replacement reactions, using Co, Cu, Al, In, or Ge atoms as substitutes for the Ni and Ga atoms, were unsuccessful. Similar phenomena have been reported for the compounds $Y_{13}Pd_{40}Sn_{31}$ [138], $Li_{13}Ni_{40}Si_{31}$, $Sc_{12.7}Ni_{40.7}Ge_{31}$ [156], $Nb(Ta)Co_4Si_3$ [157] and $Na_{26}Cd_{144}$ [158]; that is, the phases with this unique structure are composed only by specific elements of different groups.

6.2 Structural Refinement

We selected irregularly shaped single crystals of $Hf_{13.0}Ni_{40.8}Ga_{30.9}$ and $Zr_{13.0}Ni_{40.6}Ga_{31.0}$ from their annealed samples to collect crystal X-ray diffraction data for further structural refinement. For each crystals, the analysis revealed a hexagonal unit cell and the Laue group 6/mmm with a primitive lattice. Systematic absences favored a centrosymmetric structure, yielding possible space groups $P\bar{3}$, $P\bar{3}m1$, and *P6/mmm*. We chose the space group *P6/mmm* to be consistent with the one adopted by known compounds. Using direct methods, we built a structural model with 20 crystallographic sites. We assigned four positions to Hf atoms because of their large electron densities; we assigned the other positions to Ga or Ni atoms and distinguished them with the aid of site occupancy. Most sites exhibited full occupancy, but the Ga4 site only revealed an occupancy of 0.948(8). We suspect that the deficiency in electron density was influenced by nearby residuals around position (0, 0, 0), rather than by a mixed occupancy of Ga and Ni atoms. It was supported by the elongated

displacement parameters of the Ga4 site paralleling direction to residuals. Subsequent refinements reveled three residual maxima with small inter-site distances and unreasonable thermal parameters. For improved analysis, these electron densities were refined as Ni9, Ni10 with fixed U_{eq} (0.01 $Å^2$), and Ni11 with anisotropic thermal displacement. The residuals decreased significantly from 14.17 to 3.56 e/$Å^3$ with the disordered model and yielded partial occupancies for the Ni9, Ni10 and Ni11 atoms of 0.12(1), 0.116(9), and 0.180(8), respectively. Although small electron densities remained near Ni11, further refinements with the remaining residuals were unstable and failed. All metal positions, except Ni9 and Ni10, were eventually refined anisotropically. The final *R* factors *R1*, *wR2*, and *GOF* were 0.0299, 0.0598, and 1.138, respectively, with the formula $Hf_{13.0}Ni_{40.8}Ga_{30.9}$. The Zr analogue was processed in a similar manner to generate the formula $Zr_{13.0}Ni_{40.6}Ga_{31.0}$ with parameters *R1*, *wR2*, and *GOF* of 0.0348, 0.0686, and 1.088, respectively.

6.3 Crystal Structure

The structures of $Hf_{13.0}Ni_{40.8}Ga_{30.9}$ and $Zr_{13.0}Ni_{40.6}Ga_{31.0}$ can be understood as comprising three fragments—$CaCu_5$ type [159], $MnCu_2Al$ type [160] and Fe_2P type [161]—viewed along the *c* direction. The $CaCu_5$ fragments (Fig. 6.1) are located at the corners of the unit cell and form a tunnel-like structure with a six-fold rotation axis. The $MnCu_2Al$ fragments, which possess an inversion center, sit at the centers of the edges and the cell. The Fe_2P fragments with a six-fold inversion axis are surrounded by the former two fragments, placed in the positions where *x* and *y*

are equal to ±1/4.

Fig. 6.2 and 6.3 present the detailed coordinate environments of each atomic site. The distances from the central atom are truncated at 3 Å to present reasonable bonds based on the metallic radii (r_{Hf} = 1.50 Å; r_{Ga} = 1.26 Å; r_{Ni} = 1.21 Å) [147]. The interatomic distances around Hf range from 2.72 Å to 2.97 Å (Table 2.12). Despite some Hf–(Ni, Ga) contacts being longer than the sum of their corresponding metallic radii, these distances are comparable with those found in Hf_2Ga_3 ($d_{Hf–Ga}$ = 2.96 Å) [162], Hf_5Ga_3 ($d_{Hf–Ga}$ = 2.84 Å) [163] and $HfNi_2$ ($d_{Hf–Ni}$ = 2.86 Å) [164]. The Ga–Ga, Ni–Ni and Ni–Ga distances are truncated at a range from 2.36 Å to 2.81 Å, considered effective distances for bonding interactions. Such bond lengths are found in $HfGa_3$ ($d_{Ga–Ga}$ = 2.74 Å) [165], Hf_2Ni_7 ($d_{Ni–Ni}$ = 2.50–2.80 Å) [166] and $Ni_{13}Ga_9$ ($d_{Ni–Ga}$ = 2.35–2.67 Å) [167]. The Ni–Ga bonds were significantly shorter than the Ga–Ga and Ni–Ni contacts and were more abundant in the structure.

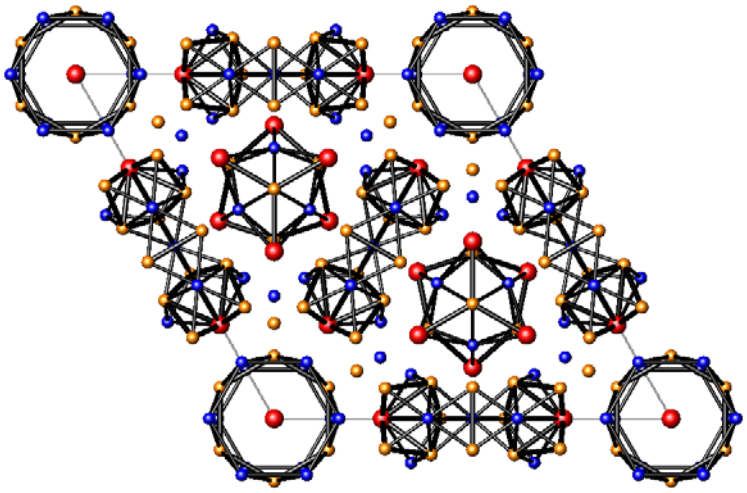

Fig. 6.1 Structure of $Hf_{13.0}Ni_{40.8}Ga_{30.9}$ in a projection along the *c*-axis, demonstrating the forms of the $CaCu_5$, $MnCu_2Al$, and Fe_2P phases. The red, yellow, and blue spheres represent Hf, Ni and Ga atoms, respectively.

Fig. 6.2a displays Hf-based polyhedra with a pentacapped pentagonal prism (Hf2, CN15), a pentacapped trigonal prism (Hf3, CN11) and a tricapped pentagonal prism (Hf4, CN13). The coordination environment of the atom Hf1 is a hexagonal antiprism with a shifted center distorting the Hf–Ni (2.85 Å) and Hf–Ga (3.05 Å) bond distances. Fig. 6.2b presents the stacking hexagons constructed by the Ni and Ga atoms with disordered sites randomly distributed within the framework around position (0, 0, 0). Because of the short distance of 2.44 Å in the vertical direction between the neighboring Hf atoms and the origin, these electron residuals were not assigned to a Hf atom but rather a Ni atom, considering where they reside in the same plane with the Ga hexagon. The distance of 2.94 Å from the center hexagon to the Ga atom is significantly longer than the average Ni–Ga bond (2.47 Å), suggesting that the disordered model can be attributed to spatial considerations.

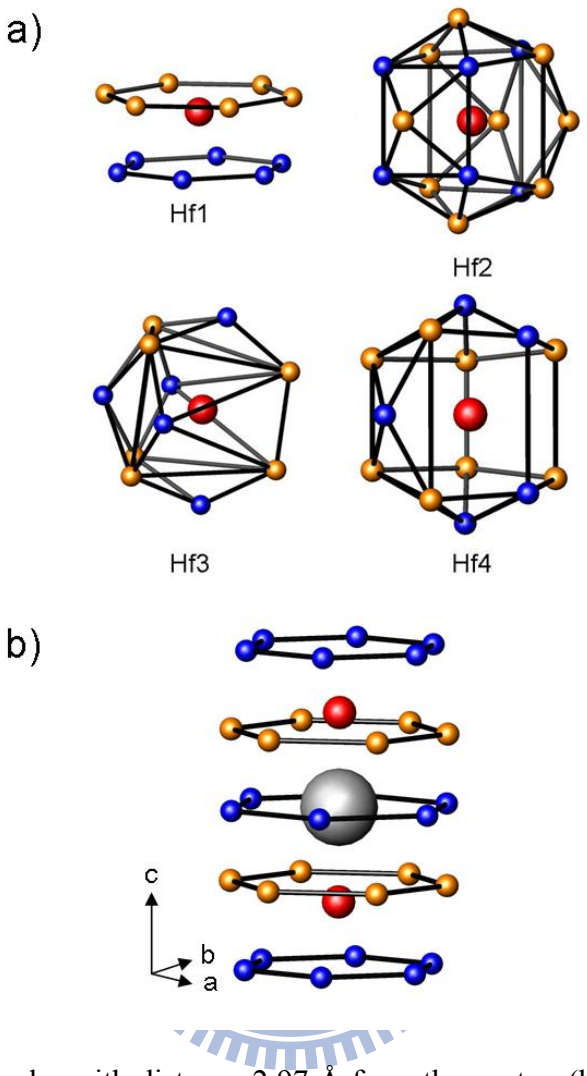

Fig. 6.2 (a) Hf-based polyhedra with distance 2.97 Å from the center. (b) Environment of disorder located around position (0, 0, 0). The colors of the spheres conform to those in Fig. 6.1.

Fig. 6.3 displays the coordination environments of Ni and Ga atoms containing 6–12 neighbors. Some of the polyhedra adopt a trigonal prism as the main framework (Ga4 and Ni2), further capped with three atoms (Ga1, Ga6, and Ni1) or a pair of atoms (Ga2). Other notable structural units include distorted icosahedra (Ga7, Ga8, Ni4, and Ni5), cuboids (Ga3) and a pentagon capped with two pairs of atoms (Ni7). The coordination environments for the Ga5, Ni3, Ni6, and Ni8 sites are randomly constructed with neighboring atoms; they are difficult to classify.

#

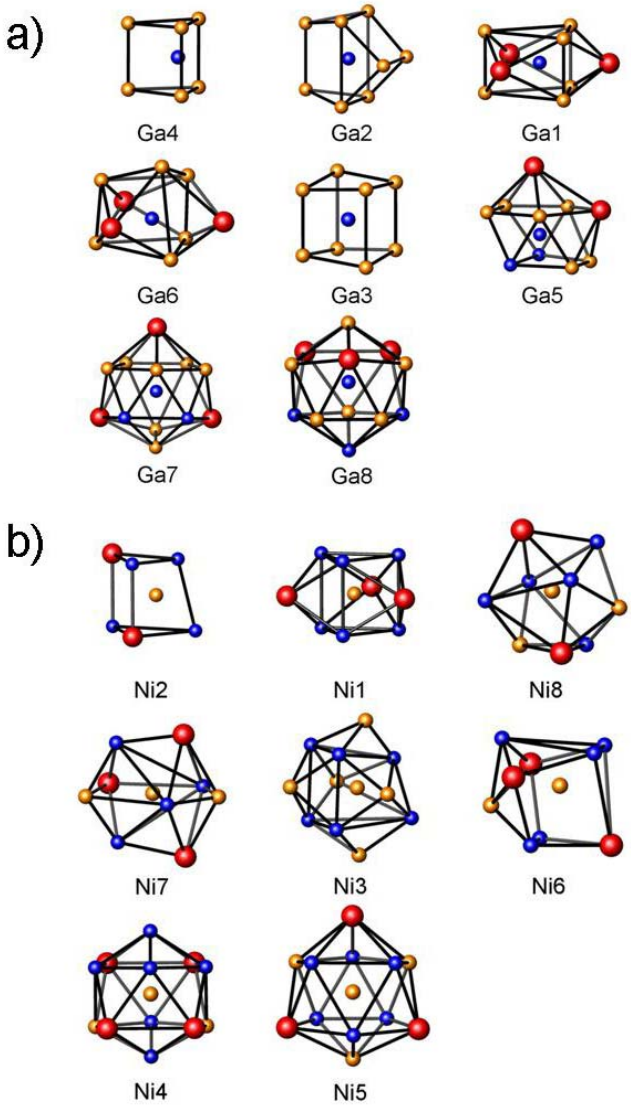

Fig. 6.3 (a) Ga- and (b) Ni-based polyhedra with truncation distances of 2.81 and 2.73 Å, respectively. The colors of the spheres conform to those in Fig. 6.1.

The structure of $Hf_{13.0}Ni_{40.8}Ga_{30.9}$ features three different layers along the *c* direction [158]; the arrangement of atoms on each layer is extended as a result of a $CaCu_5$ structure and correlates with those of similar compounds (Fig. 6.4), namely $HoNi_{3.4}Ga_{1.6}$ and $HoNi_{2.6}Ga_{2.4}$ [168]. The structure of $HoNi_{3.4}Ga_{1.6}$ features two layers: layer 1 (L1) contains one Ho atom (Wyckoff site 1*a*) with two Ni and Ga mixed positions evenly separated along the diagonal (site 2*c*); layer 2 (L2) has Ni and Ga

#

mixed sites (site 3g) that form infinite triangular nets. For $HoNi_{2.6}Ga_{2.4}$, the atomic sites on layers L1 and L2 correspond to a two-fold scale of the $CaCu_5$ structure with two sites removed from the diagonal of L1 and six sites on L2 replaced with two large atoms.

$Hf_{13.0}Ni_{40.8}Ga_{30.9}$ is a four-fold $CaCu_5$-related compound with a third extra layer 3 (L3). In L1, only two gallium atoms are expelled from the lattice, resulting in a puckered sheet because of the compactness of the positions within a confined cell. The substitutions on L2 occur on positions around the three-fold axis, generating open sites that allow Ga atoms to reside within. In addition, L3 is formed by rotating 180° on the blue triangular fragments of L2. As a result, both L2 and L3 are sandwiched by layer L1, forming a 3-D structure with an L1-L2-L1-L3-L1 stacking sequence. Although we sought to discover compounds corresponding to a three-fold scale of $CaCu_5$ composed of Ni and Ga, our many trials provided no specific results. Nevertheless, two reported compounds—$LaGaBi_2$ [169] and $La_{13}Ga_8Sb_{21}$ [170]—account for the three- and four-fold $CaCu_5$ -related samples, for which more eliminations and substitutions are performed in both L1 and L2.

Whereas the atomic size is a very significant factor affecting the structure of intermetallic compounds, the series of isostructural phases comprising elements of different groups indicate that the valence electron concentration (*vec*) is another effective factor. The number of electrons per atom of $Hf_{13.0}Ni_{40.8}Ga_{30.9}$ is 6.53 (552.7/84.7); this value is within the range 6.62–6.31 obtained from the known compounds–$Y_{13}Pd_{40}Sn_{31}$ [138], $Li_{13}Ni_{40}Si_{31}$, $Sc_{12.7}Ni_{40.7}Ge_{31}$ [156], $Nb(Ta)Co_4Si_3$ [157] and $Na_{26}Cd_{144}$ [158]. The relationship between the number of valence electrons and the

#

structure has been investigated in $RE_{2-x}Fe_4Si_{14-y}$ species and related intermetallic systems [171], where the framework and sequence of stacking layers differ as *vec* varies.

#

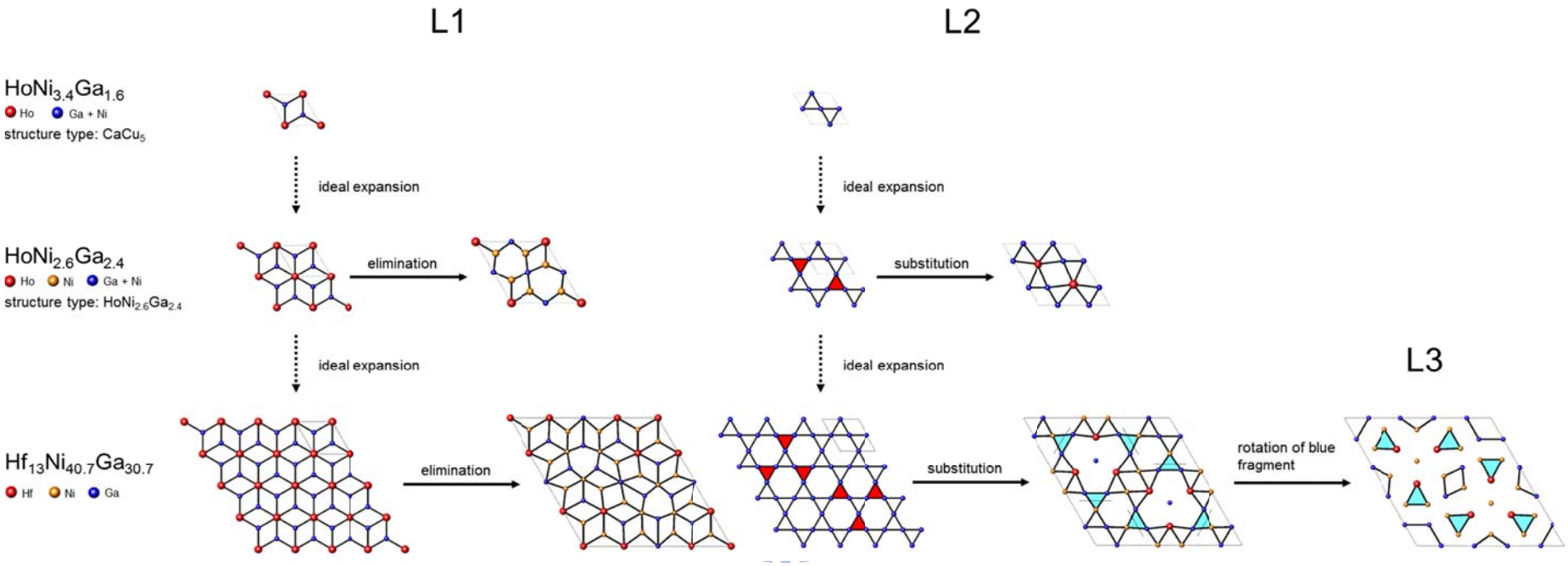

Fig. 6.4 Layers of $HoNi_{3.4}Ga_{1.6}$, $HoNi_{2.6}Ga_{2.4}$, and $Hf_{13.0}Ni_{40.8}Ga_{30.9}$, regarded as varied scales of the $CaCu_5$ structure, and the elimination and substitution of atoms performed on them. L3, a derivative layer of L2, was found only in compound $Hf_{13.0}Ni_{40.8}Ga_{30.9}$.

#

6.4 Calculations of electronic structure

Because the observed crystal structure is complicated, we used theoretical calculations to determine the electronic structure and bonding properties. Fig. 6.5 presents the calculated plots of the densities of states (DOS) and crystal-orbital Hamilton population (COHP). We performed these calculations using "$Hf_{13}Ni_{40.5}Ga_{31}$" as a theoretical model, with Ni(10) and Ni(11) sites were removed and all positions designed to be fully occupied. The DOS curve does not features a gap near the Fermi level (E_f), indicative of a metallic properties. The pronounced Ni 3d orbitals are occupied from –4 eV to the Fermi level, and are mixed with contributions from Hf and Ga atoms between –4 and –2 eV. A local minimum state appeared approximately 3 eV above the Fermi level in the plot of the DOS, indicated a characteristic feature of a polar intermetallic phase, as seen in a partial DOS (Fig. 6.6) that electron transfer is revealed in the occupied Ni 4s and 3p orbitals. Nevertheless, a large part of the Hf 4d orbitals lies below the Fermi level, indicating that the Hf atom is partial cationic and intimately involved in chemical bonding.

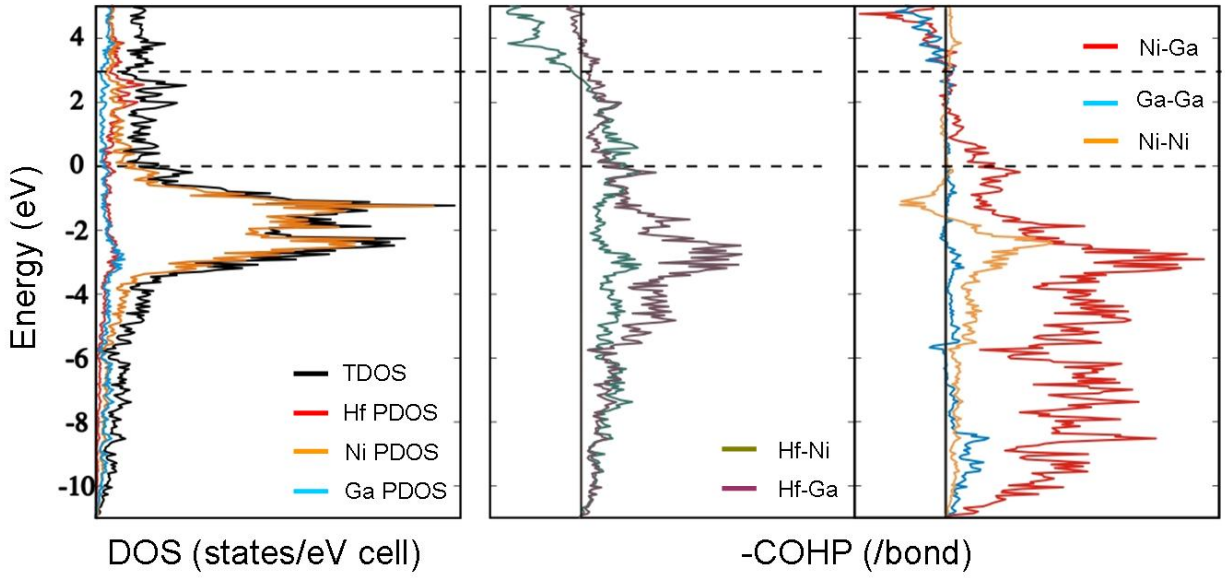

Fig. 6.5 Calculated densities of states (DOS) and crystal-orbital Hamiltonian-population (COHP) curves for the model compound $Hf_{13}Ni_{40.5}Ga_{31}$. The lower horizontal line denotes the Fermi energy; the upper line denotes the optimal level.

The COHP curves and bonding contributions from the Hf–Ni, Hf–Ga, Ni–Ga, and Ga–Ga pairs. The integrated COHP value reveals the strong interaction of the Ni–Ga bond (1.36), more than 25% greater than those of the Hf–Ni (1.03), Hf–Ga (1.09), and Ga–Ga (1.00) bonds. The Ni–Ni contact is relatively weak because of the anti-bonding contribution near the Fermi level. We suggest that these bonds are optimized at 3 eV above the Fermi level, revealing the local minimum state in the DOS curve. In the region between the Fermi level and the pseudogap, the interactions of the Ni–Ni, Ga–Ga, and Ni–Ga contacts appear to be non-bonding, whereas the Hf–Ni and Hf–Ga interactions are relatively weak. This observation suggests a potential phase width, through substitution of Ga by Ni, from $Hf_{13}Ni_{40.5}Ga_{31}$ to $Hf_{13}Ni_{50.5}Ga_{16}$, which derives from the corresponding electrons of a pseudogap. The homogenous range is, however, experimentally unattainable in the series of reactions $Hf_{13}Ni_{30+x}Ga_{40-x}$, because the major phase turned to $HfNi_2Ga$ when x was greater than 12.

#

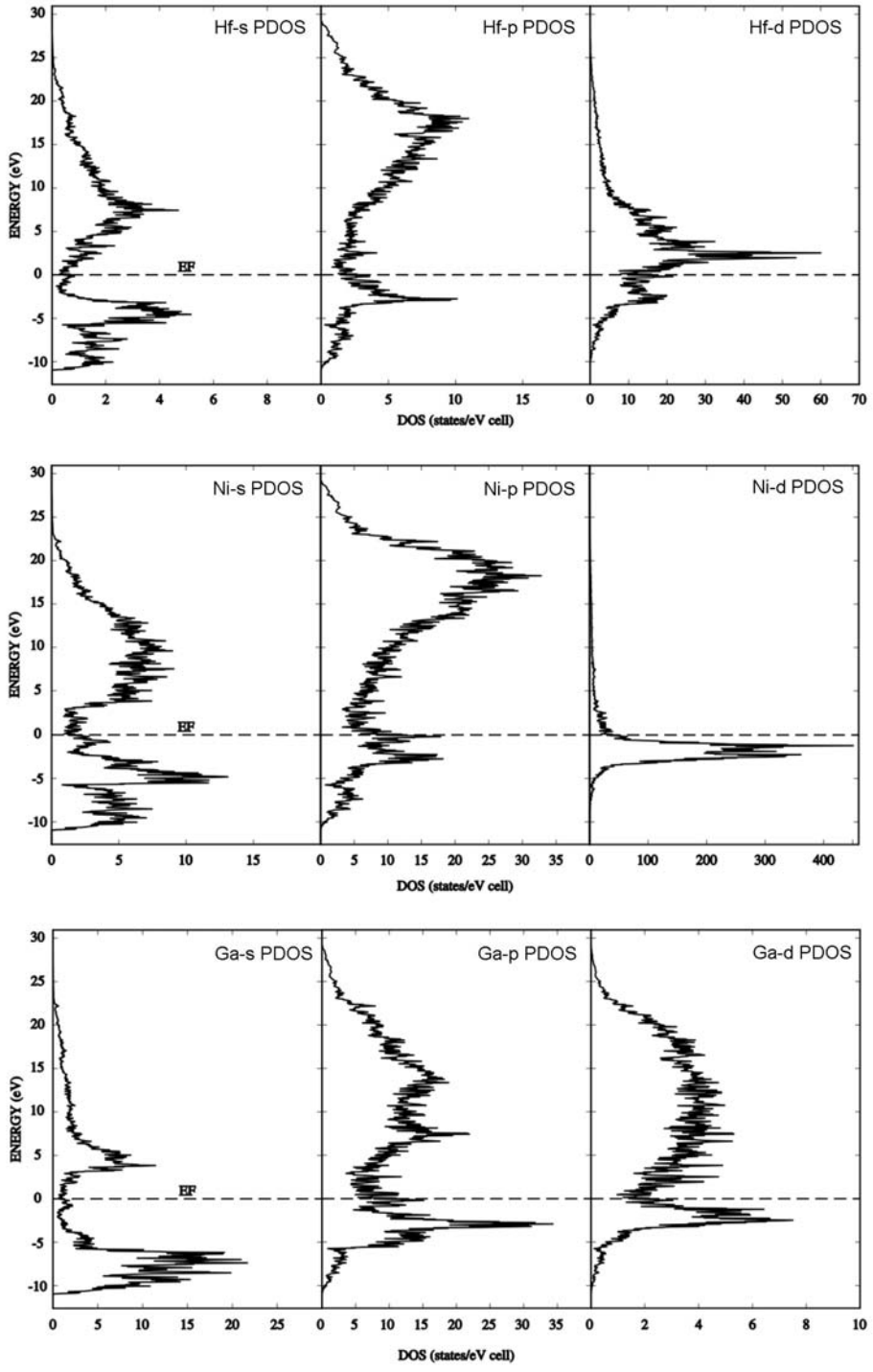

Fig. 6.6 Calculated partial densities of states (PDOS) for individual orbitals of Hf, Ni and Ga.

#

Chapter 7

Conclusion

In Hf–Cu–Al system, we have synthesized and characterized ternary Laves phases $HfAl_xCu_{2-x}$ (x = 0.2–1.0). Analysis of three crystals—$HfAl_{1.51}Cu_{0.49}$, $HfAl_{1.12}Cu_{0.88}$, and $HfAl_{0.96}Cu_{1.04}$—confirmed that the variation of the three Laves phases occurred in sequence $MgCu_2$ → $MgNi_2$ → $MgZn_2$. As smaller Cu atoms gradually replaced the Al atoms, the size reduction was observed in refined volumes and cell parameters. Theoretical calculations with the coloring models suggest that the model with high number of Al–Cu contacts is more stable due to strong bonding interaction compared to Al-Al and Cu–Cu contacts.

Furthermore, We have synthesized and characterized a ternary compound $Hf_6Cu_{16}Al_{7.58}$, which is isostructural with $Sc_{11}Ir_4$ and comprises polyhedra with coordination numbers 8–13 for Hf, Cu and Al atoms. Calculations of the electronic structure reveal a strong Cu–Al interaction that provides the greatest contribution to the structural bonding. The Al2-based octahedron exhibits a short bond from the central Al atom to the vertex Hf atom; bonding analysis indicates strong interatomic interactions from Hf–Al contacts.

In Hf–Al–Sb system, We have successfully obtained three new ternary hafnium aluminium antimonides $Hf_5Al_{3-x}Sb_x$ (x = 0.70, 1.44, 2.14). The structure of $HfAl_{2.30}Sb_{0.70}$ was isostructural with

binary compound Hf_5Al_3 of Mn_5Si_3 type, which was composed of trigonal antiprism of two types stacking along the *c* axis, whereas $HfAl_{1.56}Sb_{1.44}$ and $HfAl_{0.86}Sb_{2.14}$ adopted W_5Si_3 structure with condensations of tetrahedra and square antiprisms. Resistivity measurements revealed effective electrical conductivity. A bonding analysis revealed strong Hf-Sb interactions in models of both Mn_5Si_3 and W_5Si_3 types. The large proportion of Sb also favored anti-bonding characters (Hf-Sb for the Mn_5Si_3 type and Sb-Sb for the W_5Si_3 type), which rationalizes the variation of structure and the site preference of metal atoms.

Lastly, in Hf–Ni–Ga system, the structure of two compounds $Hf_{13.0}Ni_{40.8}Ga_{30.9}$ and $Zr_{13.0}Ni_{40.6}Ga_{31.0}$ are characterized, which comprise polyhedra with 12–15 connected neighbors for Hf and Zr atoms and 6–12 coordination numbers for Ni and Ga atoms; these structures can be regarded as extended forms of the $CaCu_5$ structure with reduction in numbers of atoms and valence electron concentration. According to calculations of the band structure, these phases are metallic and partially polar, with electron transfer revealed in the Ni 4s and 3p orbitals, and strengthened by the strong contributions of Ni–Ga bonds. In addition, the title structures has been synthesized with elements ranging from groups 1 to 5 (i.e., Li, Na, Y, Sc, Zr, Hf, Nb, Ta), but no isostructural compounds comprising elements from group 2. Accordingly, the possible permutations of Mg and Ca elements, via the information of valence electron concentration, are predicted; the corresponding experiments are in progress.

#

Reference

[1] W.E. Wallace, Annu. Rev. Phys. Chem., 15 (1964) 109-130.
[2] G. Sauthoff, Z. Metallkd., 81 (1989) 855-861.
[3] C.E. Gellert, Comm. Acad. Petropol., 13 (1751) 382-399.
[4] G. Sauthoff, Intermetallics, VCH, Weinheim, New York, Basel, Cambridge, Tokyo, 1995.
[5] G. Tammann, Z. Anorg. Chem., 45 (1905) 24.
[6] M. Laue, W. Friedrich, P. Knipping, Univ. Munich Sitzber. K. Akad. Wiss. Munchen, (1912) 303.
[7] M.R. Andrews, Phys. Rev., 10 (1921) 245.
[8] P. Debye, P. Scherrer, Phys. Z., 18 (1917) 291.
[9] G.E.R. Schulze, Metallphysik., Akademie-Verlag, Berlin, 1967.
[10] L. Pauling, J. Am. Chem. Soc., 45 (1923) 2777.
[11] C.G. Shull, S. Siegel, Phys. Rev., 75 (1949) 1008.
[12] V.M. Goldschmidt, Z. Phys. Chem., 133 (1928) 397.
[13] H. Okamoto, L.E. Tanner, Phase diagrams of binary beryllium alloys, ASM International, Metals Park, Ohio, 1987.
[14] P. Villars, L.D. Calvert, Pearson's handbook of crystallographic data for intermetallic phases, ASM International, Materials Park, OH USA, 1991.
[15] K. Wade, Adv. Inorg. Chem. Radiochem., 18 (1976) 1.
[16] E. Mooser, W.B. Pearson, Phys. Rev., 101 (1956) 1608.
[17] U. Müller, Inorganic structural chemistry, John Wiley & Sons, Ltd, Philipps-Universität Marburg, Germany, 1992.
[18] W. Hume-Rothery, G.V. Raynor, The Structure of Metals and Alloys, Institute of Metals, London, 1962.
[19] A.-K. Larsson, J. Alloys Compd., 221 (1995) 136.
[20] U. Häussermann, S.I. Simak, I.A. Abrikosov, B. Johansson, S. Lidin, J. Am. Chem. Soc., 120 (1998) 10136.
[21] C.S. Lee, G.J. Miller, J. Am. Chem. Soc., 122 (2000) 4937-4947.
[22] E. Zintl, H. Kaiser, Z. Anorg. Allg. Chem., 221 (1933) 113.
[23] J.D. Corbett, Angew. Chem. Int. Ed., 39 (2000) 670-690.
[24] T.S. You, S. Lidin, O. Gourdon, Y. W, G.J. Miller, Inorg. Chem., 48 (2009).
[25] T.S. You, G.J. Miller, Inorg. Chem., 48 (2009) 6391-6401.
[26] F. Laves, Naturwissen schaften, 27 (1939) 65.
[27] G. Leitner, G. Schulze, Krist. Tech., 6 (1971) 449.
[28] F. Stein, M. Palm, G. Sauthoff, Intermetallics, 12 (2004) 713-720.
[29] H.F. Franzen, M. Köckerling, Prog. Solid State Chem., 23 (1995) 265-289.
[30] G.J. Miller, Eur. J. Inorg. Chem., 5 (1998) 523.

#

[31] H.L. Skriver, The LMTO Method, Springer, Berlin, 1984.
[32] A.V. Tkachuk, D.G. Piercey, A. Mar, Inorg. Chem., 46 (2007) 2887.
[33] S. Ponou, N. Müller, T.F. Fässler, U. Häussermann, Inorg. Chem., 44 (2005) 7423-7430.
[34] V. Svitlyk, B.J. Campbell, Y. Mozharivskyj, Inorg. Chem., 48 (2009) 10364-10370.
[35] J.D. Corbett, Inorg. Chem., 39 (2000) 5178-5191.
[36] J.D. Corbett, Inorg. Chem., 49 (2010) 13-28.
[37] D.K. Seo, J.D. Corbett, J. Am. Chem. Soc., 122 (2000) 9621-9627.
[38] J.C. Dai, S. Gupta, O. Gourdon, H.J. Kim, J.D. Corbett, J. Am. Chem. Soc., 131 (2009) 8677-8682.
[39] S. Liu, J.D. Corbett, Inorg. Chem., 43 (2004) 2471.
[40] Q. Lin, J.D. Corbett, Inorg. Chem., 43 (2004) 1912-1919.
[41] Q. Lin, J.D. Corbett, Inorg. Chem., 47 (2008) 3462-3464.
[42] Q. Lin, J.D. Corbett, Inorg. Chem., 42 (2003) 8762-8767.
[43] Q. Lin, J.D. Corbett, J. Am. Chem. Soc., 127 (2005) 12786-12787.
[44] U. Zachwieja, J. Alloys Comp., 235 (1996) 7.
[45] Q. Lin, J.D. Corbett, J. Am. Chem. Soc., 128 (2006) 13268-13273.
[46] Q. Lin, J.D. Corbett, J. Am. Chem. Soc., 129 (2007) 6789-6797.
[47] J.C. Dai, J.D. Corbett, Inorg. Chem., 46 (2007) 4592-4598.
[48] M.G. Kanatzidis, Chem. Mater., 22 (2010) 648-659.
[49] M.C. Francisco, C.D. Malliakas, P.M.B. Piccoli, M.J. Gutmann, A.J. Schultz, M.G. Kanatzidis, J. Am. Chem. Soc., 132 (2010) 8998-9006.
[50] I. Todorov, D.Y. Chung, H. Claus, C.D. Malliakas, A.P. Douvalis, T. Bakas, J. He, V.P. Dravid, M.G. Kanatzidis, Chem. Mater., 22 (2010) 3916-3925.
[51] O. Gourdon, D. Gout, D.J. Williams, T. Proffen, S. Hobbs, G.J. Miller, Inorg. Chem., 46 (2007) 251-260.
[52] O. Gourdon, Z. Izaola, L. Elcoro, V. Petricek, G.J. Miller, Inorg. Chem., 48 (2009) 9715-9722.
[53] S. Gupta, E.A. León-Escamilla, F. Wang, G.J. Miller, J.D. Corbett, Inorg. Chem., 48 (2009) 4362-4371.
[54] T. Björling, D. Noreus, U. Häussermann, J. Am. Chem. Soc., 128 (2006) 817-824.
[55] S.Q. Xia, S. Bobev, J. Am. Chem. Soc., 129 (2007) 4049.
[56] S.Q. Xia, S. Bobev, Inorg. Chem., 47 (2008) 1919.
[57] B. Saparov, S. Bobev, Inorg. Chem., 49 (2010) 5173-5179.
[58] A.M. Mills, A. Mar, J. Am. Chem. Soc., 123 (2001) 1151-1158.
[59] H. Bie, A. Mar, J. Solid State Chem., 2009 (2009) 3131-3137.
[60] S.S. Stoyko, E.R. Blanchard, A. Mar, Inorg. Chem., 49 (2010) 2325-2333.
[61] B. Li, J.D. Corbett, Inorg. Chem., 46 (2007) 8812-8818.
[62] R. Lam, R. McDonald, A. Mar, Inorg. Chem., 40 (2001) 952-959.
[63] M.H. Ge, J.D. Corbett, Inorg. Chem., 46 (2007) 4138-4144.

#

[64] S. Derakhshan, A. Assoud, K.M. Kleinke, H. Klenike, Inorg. Chem., 46 (2007) 1459-1463.
[65] B. Li, S.J. Kim, G.J. Miller, J.D. Corbett, Inorg. Chem., 48 (2009) 6573-6583.
[66] D. Gout, T.J. Barker, O. Gourdon, G.J. Miller, Chem. Mater., 17 (2005) 3661-3667.
[67] S.Q. Xia, S. Bobev, Chem. Mater., 22 (2010) 840-850.
[68] J.D. Livingston, Phys. Status Solidi A, 131 (1992) 415-423.
[69] A.D. Huxley, C. Paulsen, O. Laborde, J.L. Tholence, D. Sanchez, A. Junod, R. Calemczuk, J. Phys.: Condens. Matter, 5 (1993) 7709-7718.
[70] S.R. Ovshinsky, M.A. Fetcenko, J. Ross, Science, 260 (1993) 176-181.
[71] F. Laves, H. Witte, Metallwirtschaft, 14 (1935) 645.
[72] F. Laves, H. Witte, Metallwirtschaft, 15 (1936) 840.
[73] F. Laves, H. Witte, Metallwirtschaft, 15 (1936) 15.
[74] R. Nesper, G.J. Miller, J. Alloys Comp., 197 (1993) 109-121.
[75] H. Klee, H.Z. Witte, Phys. Chem., 202 (1953/54) 352.
[76] S. Amerioun, S.I. Simak, U. Haussermann, Inorg. Chem., 42 (2003) 1467-1474.
[77] A.E. Dwight, T. Am. Soc. Metal, 53 (1961) 479.
[78] V.Y. Markiv, P.I. Kripyakevich, Kristallografiya, 11 (1966) 859.
[79] Y. Verbovytsky, K. Latka, J. Alloys Comp., 438 (2007) L7-L11.
[80] V.V. Burnashova, V.Y. Markiv, G.B. Stroganov, Dopov. Akad. Nauk., 1971 (1971) 1122.
[81] B.Y. Kotur, Y.V. Verbovytsky, Prace Naukowe - Wyzsza Szkola Pedagogiczna Czestochowa, Chemia i Ochrona Srodowiska, 8 (2004) 7.
[82] A. Drasner, Z. Blazina, Z. Naturforsch., B: Anorg. Chem. Org. Chem., 36 (1981) 1547.
[83] V.Y. Markiv, V.V. Burnashova, Izv. Akad. Nauk SSSR, Metally, 1969 (1969) 113.
[84] J.V. Florio, R.E. Rundle, A.I. Snow, Acta Crystallogr., 5 (1952) 449-457.
[85] G. Rixecker, R. Haberkorn, J. Alloys Compd., 316 (2001) 203-208.
[86] X. Yan, A. Grytsiv, P. Rogl, V. Pomjakushin, X. Xue, J. Alloys Compd., 469 (2009) 152-155.
[87] D. Berthebaud, O. Tougait, M. Potel, E.B. Lopes, A.P. Gonçalves, H. Noël, J. Solid State Chem., 180 (2007).
[88] Q.A. Zhang, Y.J. Liu, T.Z. Si, J. Alloys Compd., 417 (2006) 100-103.
[89] W. He, X. Wang, J. He, J. Wen, M. Yu, L. Zeng, J. Alloys Compd., 502 (2010) 87-91.
[90] B. Chabot, K. Cenzual, E. Parthe, Acta Crystallogr. B, 36 (1980) 7-11.
[91] M. Zelinska, S. Oryshchyn, O. Zhak, J.Y. Pivan, M. Potel, O. Tougait, H. Noël, D. Kaczorowski, J. Solid State Chem., 183 (2010) 2121-2126.
[92] V.Y. Markiv, A.I. Storozhenko, I.M. Panyuta, Dopov. Akad. Nauk Ukr. RSR, Ser. A, (1974) 463-466.
[93] B. Kotur, Y. Verbovytsky, E. Bauer, Visn. Lviv Univ. Ser. Chem., 44 (2004) 72-76.
[94] W.H. Huang, C.S. Lee, Intermetallics, 19 (2011) 1849-1856.
[95] R. Meyer zu Reckendorf, P.C. Schmidt, A. Weiss, Z. Phys. Chem., 163 (1989) 103-108.
[96] A.V. Grytsiv, P. Rogl, V. Pomjakushin, Intermetallics, 14 (2006) 784-791.

[97] A.V. Grytsiv, P. Rogl, G. Giester, V. Pomjakushin, Intermetallics, 13 (2005) 497-509.
[98] A.V. Grytsiv, P. Rogl, H. Schmidt, G. Giester, P. Hundegger, G. Wiesinger, V. Pomjakushin, Intermetallics, 12 (2004) 563-577.
[99] K.S. Kumar, C.T. Liu, Jom-J Min Met Mat S, 45 (1993) 28-34.
[100] T.B. Massalski, J.L. Murray, L.H. Bennett, H. Baker, Binary Alloy Phase Diagrams, ASM, Materials Park, OH, 1990.
[101] I.J. McColm, J.M. Ward, J. Alloys Comp., 178 (1992) 91-100.
[102] E. Garcia, J.D. Corbett, Inorg. Chem., 27 (1988) 2353-2359.
[103] W. Xiangzhong, L. Hongrui, H. Wei, Z.L. Min, Mater. Lett., 62 (2008) 615-618.
[104] N. Melnychenko, L. Romaka, Y. Stadnyk, D. Fruchart, O. Bodak, J. Alloys Compd., 352 (2003) 89-91.
[105] K. Young-Uk, S.C. Sevov, J.D. Corbett, Chem. Mater., 2 (1990) 550-556.
[106] J.W. Kaiser, W. Jeitschko, Z Anorg Allg Chem, 628 (2002) 337-343.
[107] H. Kleinke, C. Ruckert, C. Felser, Eur. J. Inorg. Chem., 2000 (2000) 315-322.
[108] G. Melnyk, W. Tremel, J. Alloys Compd., 349 (2003) 164-171.
[109] A.V. Tkachuk, A. Mar, J. Solid State Chem., 177 (2004) 4136-4141.
[110] J. Ye, H. Horiuchi, T. Shishido, K. Ukei, T. Fukuda, Acta Crystallogr. C, 46 (1990) 1193-1195.
[111] K. Ukei, T. Shishido, T. Fukuda, Acta Crystallogr. C, 45 (1989) 349-350.
[112] A.Y. Kozlov, V.V. Pavlyuk, Intermetallics, 11 (2003) 237-239.
[113] H. Kleinke, Can. J. Chem., 79 (2001) 1338-1343.
[114] Y.P. Yarmolyuk, Y. Grin, E.I. Gladyshevskii, Dopov. Akad. Nauk A, 40 (1978) 759-763.
[115] Y.N. Hrin, Dopov. Akad. Nauk A, 44 (1982) 80-84.
[116] Y. Grin, Y.P. Yarmolyuk, O.A. Usov, A.M. Kuz'min, V.A. Bruskov, Kristallografiya, 28 (1983) 1207-1209.
[117] A.E. Dwight, Mater. Res. Bull., 22 (1987) 305-308.
[118] L.O. Wasylechko, O.M. Sichevich, Y. Grin, J. Alloys Compd., 185 (1992) 19-24.
[119] L. Vasylechko, W. Schnelle, U. Burkhardt, R. Ramlau, R. Niewa, H. Borrmann, K. Hiebl, Z. Hu, Y. Grin, J. Alloys Compd., 350 (2003) 9-16.
[120] B. Chevalier, J.L. Bobet, E. Gaudin, M. Pasturel, J. Etourneau, J. Solid State Chem., 168 (2002) 28-33.
[121] L. Vasylechko, W. Schnelle, M. Schmidt, U. Burkhardt, H. Borrmann, U. Schwarz, Y. Grin, J. Alloys Compd., 416 (2006) 35-42.
[122] X.Z. Chen, P. Small, S. Sportouch, M. Zhuravleva, P. Brazis, C.R. Kannewurf, M.G. Kanatzidis, Chem. Mater., 12 (2000) 2520-2522.
[123] Y.J. Cho, J.N. Millican, C. Capan, D.A. Sokolov, M. Moldovan, A.B. Karki, D.P. Young, M.C. Aronson, J.Y. Chan, Chem. Mater., 20 (2008) 6116-6123.
[124] H. Flandorfer, P. Rogl, K. Hiebl, E. Bauer, A. Lindbaum, E. Gratz, C. Godart, D. Gignoux, D.

Schmitt, Phys. Rev. B: Condens. Matter, 50 (1994) 15527-15541.
[125] R.J. Cava, A.P. Ramirez, H. Takagi, J.J. Krajewski, W.F. Peck, Jr., J. Magn. Magn. Mater., 128 (1993) 124-128.
[126] S.-G. Kim, Y. Grin, E.I. Gladyshevskii, E.I. Hladyshevskii, Dopov. Akad. Nauk B, 1983 (1983) 13-15.
[127] R.W. Henning, J.D. Corbett, Inorg. Chem., 38 (1999) 3883-3888.
[128] V.Y. Markiv, N.N. Belyavina, Dopov. Akad. Nauk A, 51 (1989) 75-78.
[129] L.O. Vasilechko, Y. Grin, A.A. Fedorchuk, Neorg. Mater., 30 (1994) 1409-1411.
[130] P.I. Kripyakevich, V.Y. Markiv, Y. Melnyk, Dopov. Akad. Nauk A, 1967 (1967) 750-753.
[131] V.Y. Markiv, E.I. Gladyshevskii, Y.B. Kuz'ma, Dopov. Akad. Nauk, 1962 (1962) 1329-1331.
[132] V.Y. Markiv, Y.V. Voroshilov, P.I. Kripyakevich, E.E. Cherkashin, Sov. Phys. Crystallogr., 9 (1964) 619-620.
[133] V.Y. Markiv, N.N. Belyavina, A.A. L'Isenko, A.A. Babenko, Dopov. Akad. Nauk B, 1983 (1983) 35-37.
[134] V.Y. Markiv, N.N. Belyavina, V.E. Zavodnik, Dopov. Akad. Nauk B, 1988 (1988) 51-53.
[135] M. Schlueter, B. Heying, R. Poettgen, Z. Naturforsch. B: Anorg. Chem. Org. Chem., 58 (2003) 16-21.
[136] V.Y. Markiv, V.V. Burnasheva, Dopov. Akad. Nauk A, 1969 (1969) 463-464.
[137] V.Y. Markiv, N.N. Belyavina, A.A. Babenko, Dopov. Akad. Nauk B, 1983 (1983) 43-46.
[138] K. Cenzual, E. Parthe, Acta Crystallogr. C, 40 (1984) 1127-1131.
[139] SAINT Version 6.22., Version 4 ed., Siemens Analytical X-ray Instruments Inc., Madison, WI., 2001.
[140] SADABS, Bruker/Siemens area detector absorption and other corrections, V2.03, Bruker Analytical X-ray Systems, Inc., Madison, WI., 2001.
[141] O.K. Andersen, Phys. Rev. B: Condens. Matter, 12 (1975) 3060.
[142] O.K. Andersen, O. Jepsen, V.N. Antonov, B.Y. Yavorsky, A.Y. Perlov, A.P. Shpak, Physica B 204 (1995) 65.
[143] P.E. Blöhl, O. Jepsen, O.K. Andersen, Phys. Rev. B: Condens. Matter, 49 (1994) 16223.
[144] L. Hedin, B.I. Lundqvist, J. Phys. C: Solid State Phys, 4 (1971) 2064.
[145] R. Dronskowski, P.E. Blöhl, J. Phys. Chem., (1993) 8617.
[146] L. Bsenko, Acta Crystallogr. B, 32 (1976) 2220.
[147] L. Pauling, The Nature of the Chemical Bond, Cornell University Press, Ithaca, NY, 1960.
[148] J. Laugier, B. Bochu, Celref, in, pp. http://www.inpg.fr/LMGP; Laboratoire des Materiaux et du Génie Physique de l'Ecole Supérieure de Physique de Grenoble.
[149] F. Wang, K.N. Person, G.J. Miller, Chem. Mater., 21 (2009) 230.
[150] V.Y. Markiv, Y.V. Voroshilov, P.I. Kripyakevich, E.E. Cherkashin, Kristallografiya, 9 (1964) 737-738.
[151] M. El Boragy, R. Szepan, K. Schubert, J. Less-Common Met., 29 (1972) 133-140.

[152] P. Ramachandrarao, M. Laridjani, J. Mater. Sci., 9 (1974) 434-437.
[153] H. Boller, H. Novotny, A. Wittmann, Monatsh. Chem., 91 (1960) 1174-1184.
[154] H. Kleinke, C. Felser, J. Alloys Compd., 291 (1999) 73-79.
[155] H. Wang, E.A. Carter, J. Am. Chem. Soc., 115 (2003) 2357-2362.
[156] O.I. Bodak, V.V. Pavlyuk, R.I. Andrusyak, B.Y. Kotur, V.K. Pecharskii, V.A. Bruskov, Kristallografiya, 35 (1990) 312-315.
[157] M. Vilasi, G. Venturini, J. Steinmetz, B. Malaman, J. Alloys Compd., 227 (1995) 32-36.
[158] E. Todorov, S.C. Sevov, Inorg. Chem., 37 (1998) 6341-6345.
[159] W. Haucke, Z. Anorg. Allg. Chem., 244 (1940) 17-22.
[160] O. Heusler, Ann. Phys., 19 (1934) 155-201.
[161] S.B. Hendricks, P.R. Kosting, Z. Kristallogr., 74 (1930) 511-533.
[162] M. Poetzschke, K. Schubert, Z. Metallkd., 53 (1962) 474-488.
[163] H. Boller, E. Parthe, Monatsh. Chem., 94 (1963) 225-226.
[164] V.V. Pet'kov, V.Y. Markiv, V.V. Gorskii, Izv. A. N. SSSR, Met., 1972 (1972) 188-192.
[165] M. Poetzschke, K. Schubert, Zum Aufbau einiger T(4)-B(3) homologer und quasihomologer Systeme. I. Die Systeme Ti-Ga, Zr-Ga und Hf-Ga, Z. Metallkd., 53 (1962) 474-488.
[166] J.K. Dattagupta, K. Schubert, Z. Metallkd., 64 (1973) 789-792.
[167] M. Ellner, S. Bhan, K. Schubert, J. Less-Common Met., 19 (1969) 245-252.
[168] Y. Grin, Y.P. Yarmolyuk, V.K. Pecharskii, Izv. A. N. SSSR, Met., 1983 (1983) 213-218.
[169] M.G. Morgan, M. Wang, W. Chan, A. Mar, Inorg. Chem., 42 (2003) 1548-1555.
[170] A.M. Mills, A. Mar, Inorg. Chem., 39 (2000) 4599-4607.
[171] M. Han, Y. Wu, M. Kramer, B. Vatovez, F. Grandjean, G.J. Long, G.J. Miller, Inorg. Chem., 45 (2006) 10503-10519.

Appendix

In our study, ternary crystallization diagram is utilized as a tool to organizes and illustrates stoichiometric ratios for all exploratory synthesis. Each vertex of diagram indicates a full component element (A, B or C). The line between two vertexes is concentration line of one binary system (A_mB_n); similarly, the lines inside diagram between two points on edges is concentration line of one ternary system [$A_m(B_{1-\delta}C_\delta)_n$, or $(A_{1-\delta}C_\delta)_mC_n$]. Blue dots on the ternary phases diagrams indicate the ratios of elements used for exploratory synthesis of new intermetallic compound. Red dots indicate known binary or ternary compounds.

(a) **Hf–Al–Ge system**

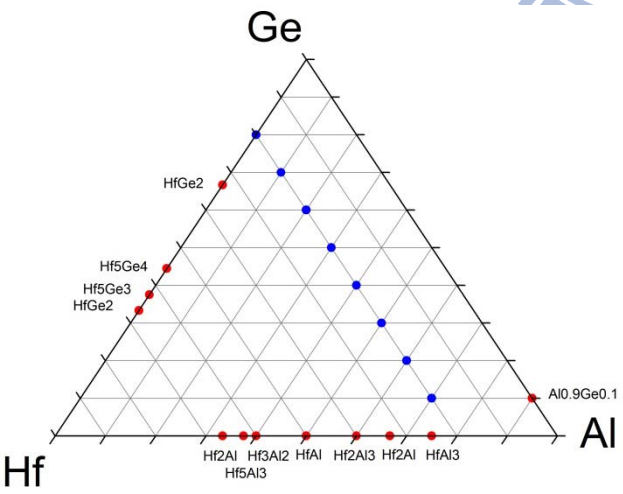

(b) **Hf–Al–Sb system**

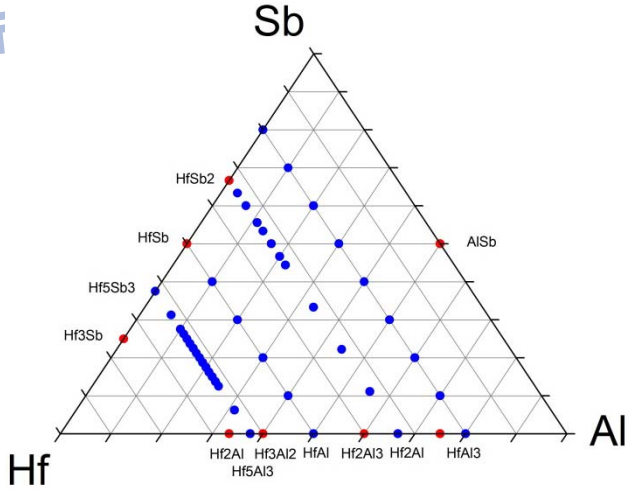

(c) **Hf–Cu–Al system**

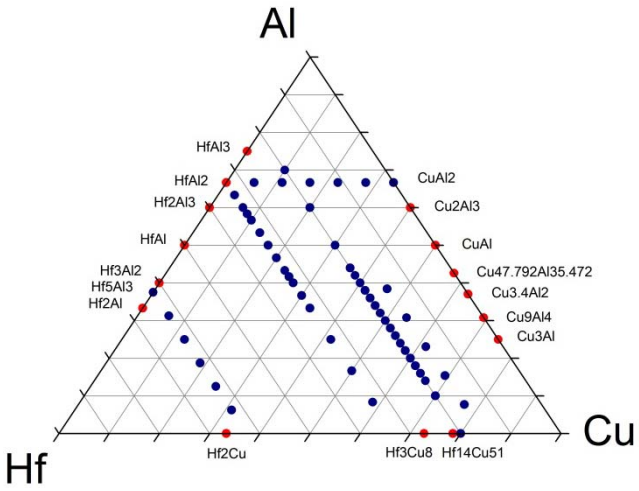

(d) **Hf–Cu–Ga system**

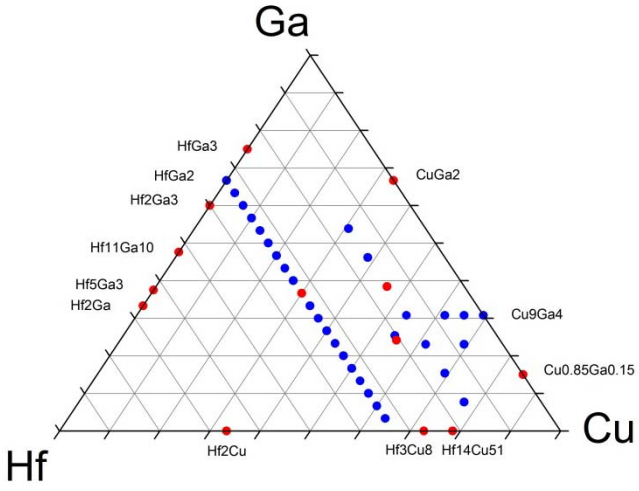

(e) **Hf–Cu–In system**

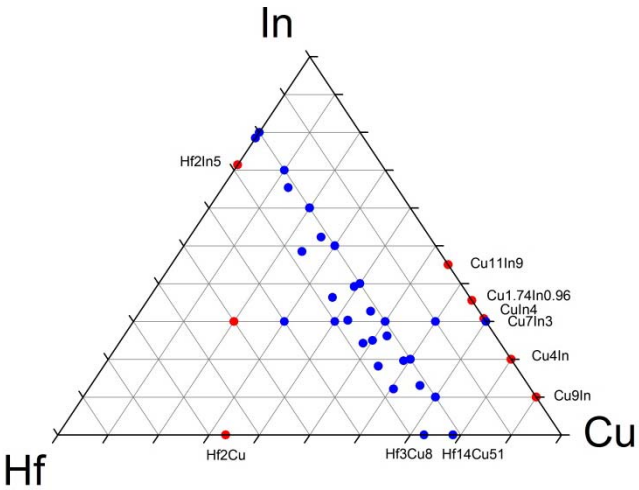

(f) **Hf–Cu–Sb system**

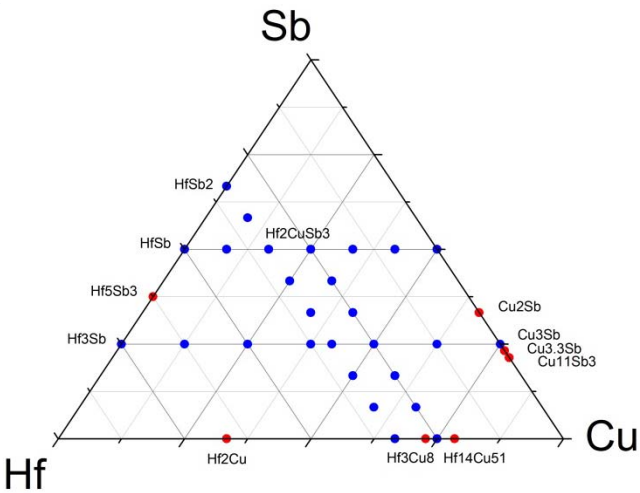

(g) **Hf–Cu–Si system**

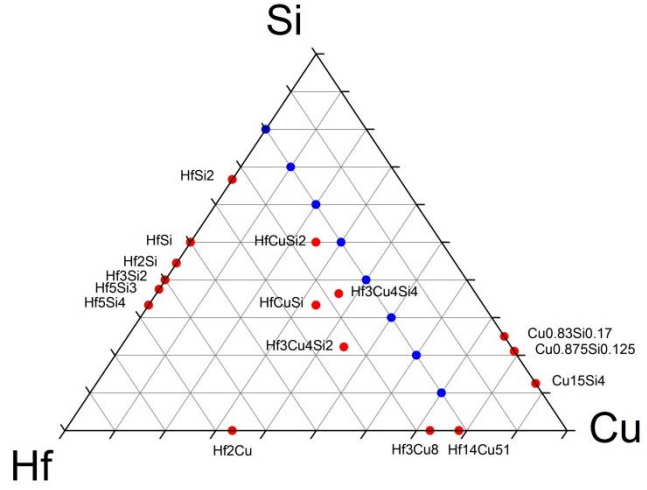

(h) **Hf–Cu–Sn system**

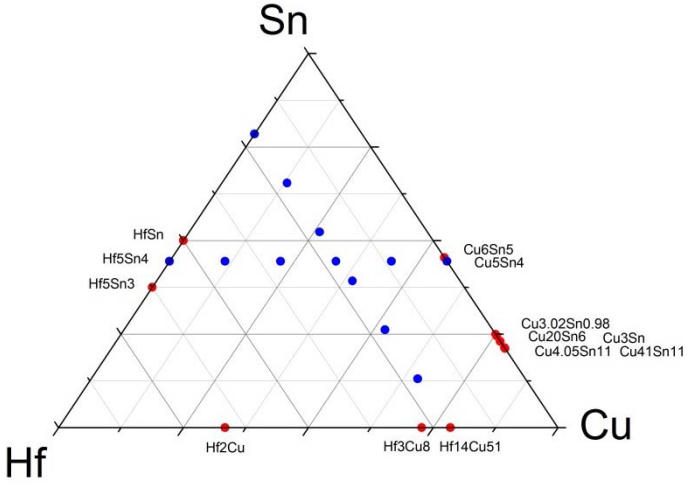

#

(i) **Hf–Ni–Ga system**

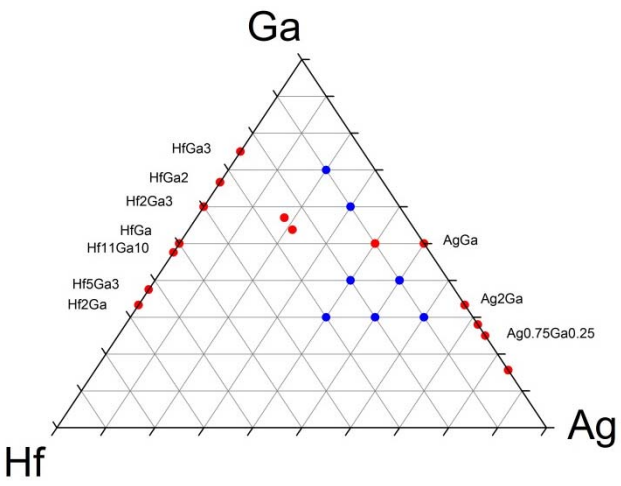

(j) **Hf–Ag–Al system**

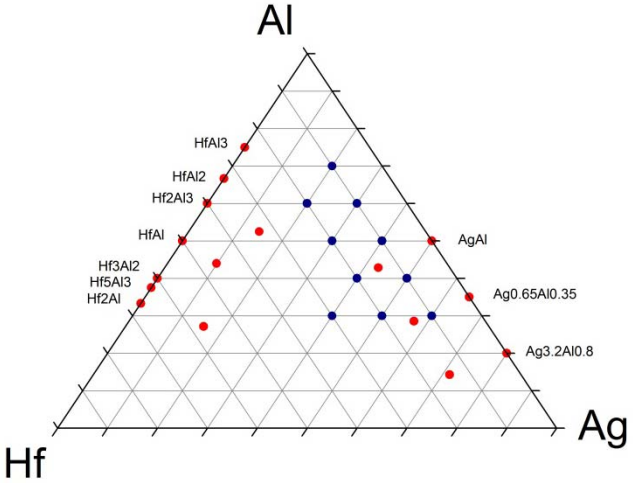

(k) **Hf–Ag–Ga system**

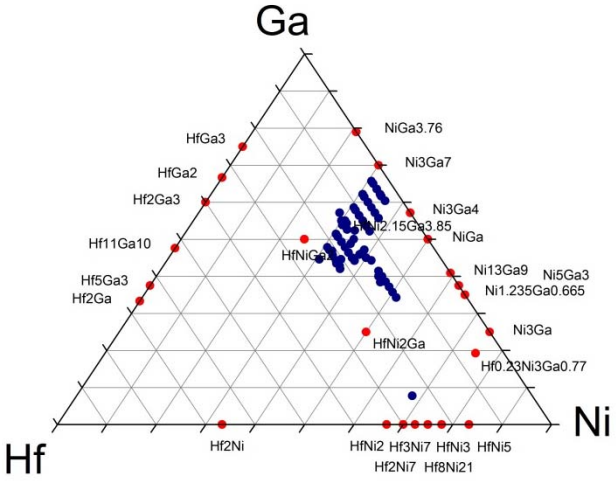

(l) **Hf–Ni–Al system**

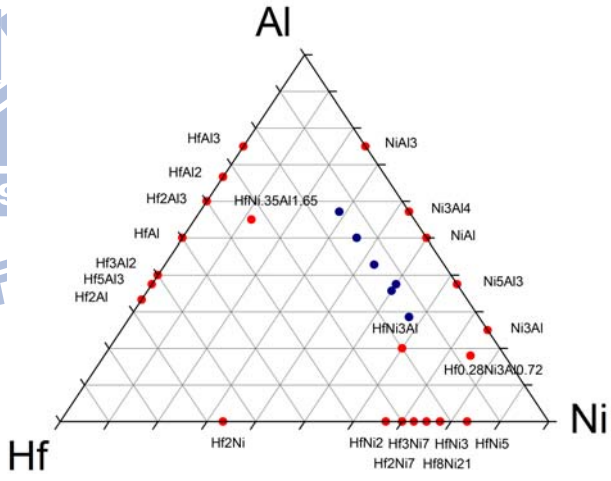

#